Stony Brook University

The Involvement of Metal Ions in Copper-Zinc Superoxide Dismutase Related Amyotrophic Lateral Sclerosis

by

Megan Whitney Bourassa

to

The Graduate School

in Partial Fulfillment of the

Requirements

for the Degree of

Doctor of Philosophy

in

Chemistry

Stony Brook University

August 2012

Stony Brook University

The Graduate School

Megan Whitney Bourassa

We, the dissertation committee for the above candidate for the

Doctor of Philosophy degree, hereby recommend

acceptance of this dissertation.

Lisa M. Miller, Ph.D – Dissertation Advisor

Biophysicist, National Synchrotron Light Source, Brookhaven National Laboratory

Benjamin Hsiao, Ph.D - Chairperson of Defense

Chair, Department of Chemistry

Nicole Sampson, Ph.D

Professor, Department of Chemistry

Martina Ralle, Ph.D

Research Assistant Professor, Department of Biochemistry and Molecular Biology, Oregon Health and Sciences University

This dissertation is accepted by the Graduate School

Charles Taber

Interim Dean of the Graduate School

Abstract of the Dissertation

The Involvement of Metal Ions in Copper-Zinc Superoxide Dismutase Related Amyotrophic Lateral Sclerosis

by

Megan Whitney Bourassa

Doctor of Philosophy

in

Chemistry

Stony Brook University

2012

Amyotrophic lateral sclerosis (ALS) is a neurodegenerative disease affecting the motor neurons of the spinal cord. While most ALS cases are sporadic with no known cause, some are linked to mutations in the antioxidant protein copper-zinc superoxide dismutase (SOD1), which is associated with the formation of small SOD1 aggregates in motor neurons. While the aggregation of SOD1 has been studied extensively *in vitro*, much less is known about aggregate-formation and its effects on metal homeostasis and neurodegeneration in intact cells and tissues. Therefore, the goal of this thesis was to understand how SOD1 aggregation plays a role in metal homeostasis and oxidative damage in SOD1-ALS by combining high-resolution X-ray and infrared imaging methodologies with both mouse and cell culture models of the disease. Results showed that the SOD1 aggregates were unmetallated within the cells, suggesting that aggregate formation occurs with the nascent protein and prior to delivery of copper and zinc to the enzyme's active site. It has been suggested that aggregation protects the cells by preventing

cytotoxic reactions arising from improperly bound metal in soluble SOD1 mutants. Cells containing SOD1 aggregates also showed a reduced intracellular copper concentration, which is consistent with the inability of the misfolded protein to be metallated by copper chaperone proteins. In contrast, the copper content in the spinal cords of a SOD1-ALS mouse model was dependent upon the ability of the SOD1 mutant to bind metal, i.e. only mutations that permitted copper-binding showed elevated copper in the spinal cord. This suggests that there could be more soluble metallated SOD1 in the tissues than in the cells, which quickly form dense unmetallated aggregates, and would account for the difference between the two models. Interestingly, the copper levels in the spinal cord tissue were not correlated with increased oxidative stress, as most spinal cords showed evidence of oxidative damage. One exception was G37R, which is a mutation with a protected copper active site and increased aggregation propensity, both of which reduce aberrant forms of SOD1 that can contribute to oxidative damage. Thus, this research identifies complex relationships in the disease pathology, where soluble forms of mutant SOD1 can lead to damaging redox reactions due to improper copper binding whereas SOD1 aggregation prevents the binding of copper, essentially neutralizing the redox toxicity of the mutant SOD1. In both cells and tissues, SOD1-ALS is associated with altered copper homeostasis, which can affect other antioxidant mechanisms beyond SOD1. This new understanding of aggregate formation, metal homeostasis, and oxidative damage in ALS could lead to improved treatment options and ultimately a cure.

TABLE OF CONTENTS

LIST OF FIGURES

LIST OF TABLES

LIST OF ABBREVIATIONS

5xFAD	Alzherimer's disease mouse model
A4V	Alanine 4 Valine
AD	Alzheimer's disease
ALS	Amyotrophic lateral sclerosis
AMPA	α-amino-3-hydroxy-5-methylisoxazole-4-propionic acid
APPVn/NOS2	Alzheimer's disease mouse model
APS	Advanced Photon Source
ATR	Attenuated total reflectance
BNL	Brookhaven National Laboratory
CaF_2	Calcium fluoride
CCS	Copper chaperone for SOD1
CHO-K1	Chinese hamster ovary cells
CNS	Central nervous system
CSF	Cerebrospinal fluid
D125H	Aspartic acid 125 Histidine
EDTA	Ethylenediaminetetraacetic acid
ER	Endoplasmic reticulum
EXAFS	Extended X-ray absorption fine structure
FBS	Fetal bovine serum
FALS	Familial amyotrophic lateral sclerosis
FTIR	Fourier transform infrared
FTIRI	Fourier transform infrared imaging

FTIRM	Fourier transform infrared microscopy
FPA	Focal plane array
FUS	Fused-in-sarcoma
G37R	Glycine 37 Arginine
G93A	Glycine 93 Alanine
H_2O_2	Hydrogen peroxide
HEPES	4-(2-hydroxyethyl)-1-piperazineethanesulfonic acid
H46R/ H48Q	Histidine 46 Arginine and Histidine 48 Glutamine
H80R	Histidine 80 Arginine
IR	Infrared
KB	Kirkpatrick-Baez
KO	Knock-out
L126Z	Leucine 126 deletion
MBR	Metal binding region
MCT	Mercury cadmium telluride
NIST	National Institute of Standards and Technology
NMDA	N-methyl-D-aspartate
NO	Nitric oxide
NSLS	National Synchrotron Light Source
NTG	Non-transgenic
O_2^-	Superoxide
$ONOO^-$	Peroxynitrite
OCT	Optimal cutting temperature (embedding compound)

PSAPP	B6C3-Tg(APP_{swe},PSEN1dE9) 85Dbo/J (mouse model)
PBS	Phosphate buffered saline
PCA	Principle component analysis
PS	Polystyrene
RNS	Reactive nitrogen species
ROI	Region of interest
ROS	Reactive oxygen species
RPM	Revolutions per minute
SALS	Sporadic amyotrophic lateral sclerosis
SD	Standard deviation
Si_3N_4	Silicon nitride
SOD1	Copper-zinc superoxide dismutase
SOD1-ALS	Copper-zinc superoxide dismutase related amyotrophic lateral sclerosis
TDP-43	Transactivating response element DNA binding protein
UV	Ultraviolet
WT	Wild type
WTL	Wild type like
XAS	X-ray absorption spectroscopy
XANES	X-ray absorption near edge spectroscopy
XFM	X-ray fluorescence microscopy
YFP	Yellow fluorescent protein
ZnSe	Zinc Selenide

ACKNOWLEDGMENTS

I would like to express my deepest gratitude to my advisor Dr. Lisa Miller, who has provided excellent guidance and support. Her expertise and suggestions have significantly improved the quality of everything I have done and written. She has patiently taught me to how to do research and to remember the 'big picture.'

I also wish to thank my fellow group members, Alvin Acerbo, Dr. Imke Bodendiek, Dr. Meghan Faillace, Sarah Heins, Dr. Andreana Leskovjan, Daphne Meza, Dr. Ruth Pietri, Randy Smith, Dr. Eli Stavitski, and Dr. Ryan Tappero. They have spent countless hours teaching me to operate beamlines, grow cells, section tissues, analyze data, accompanied me on numerous beamtime trips to APS, and provided endless support.

My experiments were made possible by my collaborators who provided samples, data and a vast knowledge of ALS. I am indebted to Dr. Dave Borchelt, Hilda Brown, and Susan Fromholt for their help with mouse and cell culture experiments. Also, to Dr. Joan Valentine and especially Dr. Herman Lelie, who has performed several complementary experiments that have helped me interpret my data.

I am grateful for the help I received both at the NSLS from Dr. Tony Lanzirotti and Dr. Erik Farquhar; and at the APS from Dr. Stefan Vogt, Dr. Sophie Charlotte Gleber, Dr. Raul Barrea, and Dr. Naresh Kujala. Without their help, I would still be trying to collect and analyze data.

I am also extremely thankful to those who helped me edit the numerous versions of my dissertation, including Judy Bourassa, Dr. Sanjaya Senanayake, and Dr. Andreana Leskovjan.

Most importantly, I wish to thank my family and friends, who have encouraged and supported me throughout my education. They have kept me happy with food, drinks, and love.

PUBLICATIONS

1. **Bourassa, M.W.**, Miller, L.M. (2012). Metal Imaging in Neurodegenerative Diseases. *Metallomics.* (Accepted - In Press).

2. Lelie, H.L., Liba, A., **Bourassa, M.W.**, Chan, P.K., Gralla, E.B., Miller, L.M., Borchelt, D.R., Valentine, J.S., Whitelegge, J.P. (2011). Copper and Zinc Metallation Status of Copper-Zinc Superoxide Dismutase from Amyotrophic Lateral Sclerosis Transgenic Mice. *Journal of Biological Chemistry.* 286: 4, 2795-2806.

CHAPTER 1

INTRODUCTION

1.1 AMYOTROPHIC LATERAL SCLEROSIS (ALS)

ALS is a devastating neurodegenerative disease that affects two out of every 100,000 people worldwide, making ALS the most common motor neuron disease [1]. ALS, more commonly known in the US as Lou Gehrig's disease, is characterized by the degeneration of the motor neurons located in the ventral horn of the spinal cord, ALS begins with muscle weakness and progresses to total paralysis. In general the disease is fatal within the first two to five years of the onset of symptoms. The typical age of onset is between 50 and 60 years of age [2] and is more common in men than women [3]. There is currently no cure for ALS, and the only approved treatment is a drug named riluzole, a glutamate inhibitor that increases the life expectancy by about three months.

ALS is a complex and multifactorial disease that is believed to have several etiological factors. The majority of ALS cases (90-95%) are sporadic (SALS) in nature with no known cause. However, certain environmental factors, such as exposure to heavy metals and pesticides, have been correlated to increased rates of incidence of the disease [4]. In addition, a few geographical regions have unusually high incidence of ALS, including the Kii peninsula of Japan and Guam [1]. The remaining 5-10% of cases have a genetic link, where mutations in several different genes are known to cause familial ALS (FALS). A common etiology that could link sporadic and familial ALS remains elusive [5]. However, the presence of ubiquinated protein

inclusions has recently been identified in both SALS and FALS cases. The transactivating response element DNA binding protein (TDP-43) has been found in the motor neurons of SALS patients [6, 7]. TDP-43 is thought to play a role in RNA processing; thus it is normally localized to the nucleus. Interestingly, the inclusions are exclusively located in the cytosol of SALS and some FALS patients [7]. Many FALS patients also develop protein inclusions with other misfolded or mutant proteins [8]. Specifically, patients with genetic mutations to SOD1 or fused-in-sarcoma (FUS) [9], associated with juvenile ALS [10], develop aggregates of the mutated protein in the motor neurons. While there is currently no hypothesis to explain the pathogenesis of both FALS and SALS, the ubiquinated inclusions and a disruption in RNA processing, which is influenced by TDP-43 and FUS, are possible causes [11, 12].

Regardless of the type of ALS (sporadic or familial), the motor neurons of the spinal cord are exclusively affected by the disease. The spinal cord is comprised of several regions and is divided into the gray matter and the white matter as shown in **Figure 1.1** [13]. Gray matter primarily consists of cell bodies, such as neurons and glial cells, and thus it is high in protein content. The gray matter is divided into two horns, ventral and dorsal, that create a butterfly shape within the spinal cord. The dorsal horn consists of sensory neurons that are responsible for relaying information, such as touch and vibration to the brain. The ventral horn of the gray matter contains the motor neurons affected by ALS and control movement. The white matter surrounds the gray matter butterfly and is composed of myelinated axons that are rich in lipids for signal transduction.

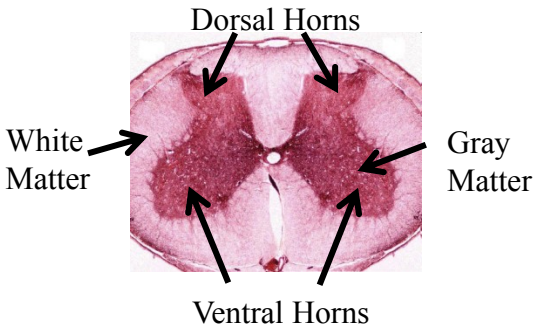

FIGURE 1.1 A histochemically stained spinal cord cross section depicting the protein-rich gray matter 'butterfly' surrounded by the lipid-rich white matter. The ventral and dorsal horns subdivide the gray matter and are the locations of the motor and sensory neurons, respectively (Adapted from [13]).

An explanation for why motor neurons are specifically targeted in ALS, while sensory neurons and the remainder of the central nervous system (CNS) are unaffected, remains unclear [1]. It has been hypothesized that the larger size of the motor neurons increases metabolic demands that force the cell to rely on a robust cytoskeleton and efficient axonal transport. These processes are also linked to the high demands on the mitochondria, which are severely affected by ALS. Increased mitochondrial stress can lead to the production of reactive oxygen species (ROS), through a leaky respiratory system, that result in oxidative stress. ROS are defined as oxygen-containing molecules that are more reactive than molecular oxygen itself [14]. The motor neurons also rely heavily on ROS and reactive nitrogen species (RNS) for axonal signaling. Thus the combination of mitochondrial stress with these signaling molecules may cause a shift in the crucial equilibrium of ROS/RNS and antioxidant mechanisms. In addition, motor neurons are highly susceptible to excitotoxicity. This is based on the high levels of active AMPA receptors that lack the GluR2 subunit, which determines calcium permeability, resulting in increased glutamate release and calcium. The relatively low levels of calcium buffering

proteins in motor neurons exacerbate this effect. These factors are thought to contribute to the high specificity to motor neurons seen in ALS.

1.2 COPPER-ZINC SUPEROXIDE DISMUTASE (SOD1)

Approximately 25% of FALS cases are caused by a mutation in the gene that codes for copper-zinc superoxide dismutase (SOD1) [15]. SOD1 is a vital antioxidant protein. Human SOD1 is a 32 kDa protein that exists as a homodimer via an intermolecular disulfide bond [16]. Each monomer consists of a beta-barrel with eight antiparallel beta strands [17] and one copper and one zinc binding site located just outside the beta barrel. Three histidine residues and one aspartic acid residue coordinate the zinc site and is responsible for the structural stability of SOD1. Copper is responsible for the catalytic activity of the protein. In the reduced state, the copper ion is coordinated with three histidine residues but in the oxidized state, it is coordinated by a fourth bridging histidine residue that is shared by the zinc ion. **Figure 1.2** depicts the secondary structure of SOD1 with a ribbon diagram and demonstrates the active site in the metal binding region. SOD1 is ubiquitously expressed in all cell types, where it catalyzes the reaction that converts superoxide to molecular oxygen (O_2) and hydrogen peroxide (H_2O_2) (Reactions 1 and 2).

$$Cu^{2+}ZnSOD + O_2^- \longrightarrow Cu^{+}ZnSOD + O_2 \quad (1)$$

$$Cu^{+}ZnSOD + O_2^- + 2H^+ \longrightarrow Cu^{2+}ZnSOD + H_2O_2 \quad (2)$$

These two reactions are incredibly efficient, occurring at nearly diffusion-limited rates (2×10^9 M^{-1} s^{-1}) for enzymatic catalysts at physiological pH [18].

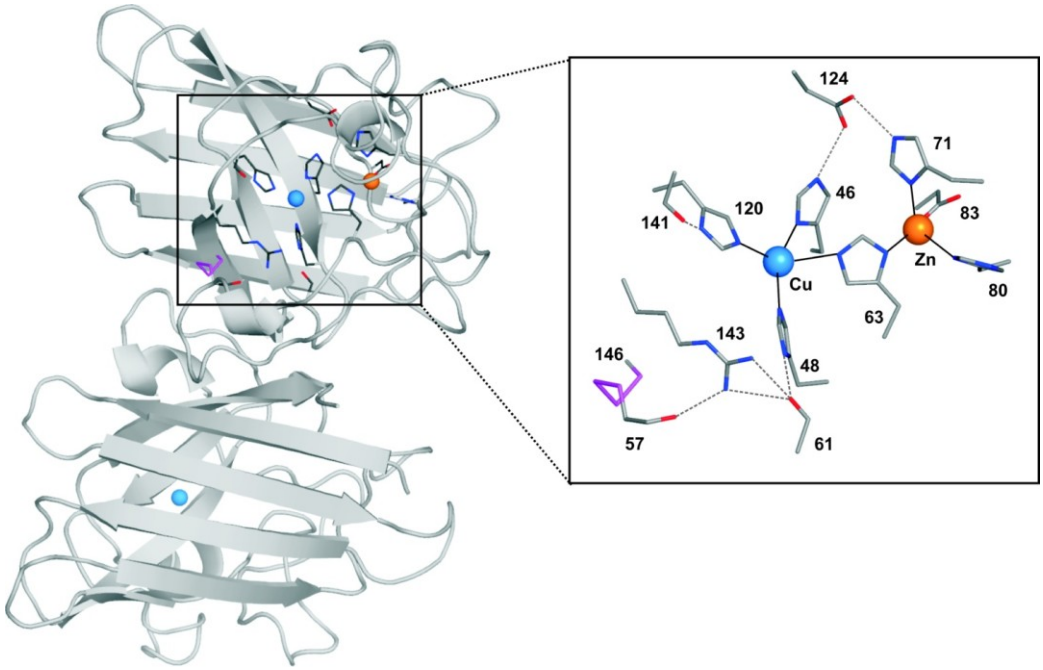

FIGURE 1.2 A ribbon diagram of an SOD1 homodimer showing the antiparallel β-sheets, and the copper (blue sphere) and zinc (orange sphere) binding sites within the protein. The metal binding region is expanded to show the histidine (His 46, His48, His 63, His 71, His80, and His 120) and aspartic acid (Asp124) residues responsible for coordinating the metal ions and the amino acids that contribute to the hydrogen bonding network of the active site. His63 is the bridging histidine that is responsible for coordinating both the zinc and copper in the reduced state of the protein [16].

Aside from its high catalytic efficiency, SOD1 is an extraordinarily stable protein, with a half-life of 100 hours when mouse SOD1 is expressed in human kidney cells [19]. A large part of the protein's stability is associated with its intramolecular disulfide bond. In the reducing environment of the cytosol, stable disulfide bonds are highly unusual. The disulfide bond is formed by the copper chaperone for SOD1 (CCS), which also delivers the copper ion to nascent SOD1. In addition, SOD1 is abundantly expressed in cells with concentrations ranging from 10 to 100 μM [2, 20]. The high activity, stability and concentration emphasize the importance of SOD1 in the cellular environment. As a result, mutations in SOD1 have a dramatic effect on cells.

Superoxide is thought to be an accidental byproduct of adding an electron to molecular oxygen during respiration. It is highly reactive with nitric oxide (NO), leading to the production of highly reactive peroxynitrite ($ONOO^-$) species [21, 22]. Iron-sulfur clusters, such as dehydratase, also risk damage by superoxide through the removal of an iron atom, rendering the enzyme inactive [23]. H_2O_2, a product of the superoxide dismutase reaction, is still a ROS; but the oxygen-oxygen bond is less reactive [24], and it is a relatively poor oxidant [25] compared to superoxide. Specifically, H_2O_2 is significantly less reactive with iron-sulfur compounds with a reaction constant of 10^2-10^3 M^{-1} s^{-1}, which is 10,000 fold less than the same reaction with superoxide [26]. H_2O_2 is also capable of reacting with cysteine and methionine residues, but with a very low reaction rate constant of 2-20 M^{-1} s^{-1} for cysteine and lower values for methionine [27]. The majority of the toxicity attributed to H_2O_2 is associated with its ability to decompose into hydroxyl radicals (·OH), a reaction that can be catalyzed by redox active metals like iron and copper through the Fenton reaction [25]. However, the reaction constants for this are relatively low and have been measured between 76 M^{-1} s^{-1} [28] and 6000 M^{-1} s^{-1} [29] with free iron and iron bound to a ligand, respectively. Some estimates have stated that this would result in the formation of approximately one hydroxyl radical per minute per cell and thus has a negligible impact on the cellular environment [24].

1.3 SOD1 MUTATIONS IN ALS

There are over 160 known individual mutations in SOD1, any one of which can cause ALS [30, 31]. These mutations occur throughout the protein chain and have been found at nearly every residue. ALS patients with SOD1 mutations develop aggregates containing the protein in their motor neurons [32].

SOD1 mutations are classified into two distinct categories, wild type like (WTL) and metal binding region (MBR) mutations [33, 34]. WTL mutations, such as A4V, G37R, G93A and L126Z, are capable of binding copper and zinc and generally maintain similar enzymatic activity to that of the WT protein. MBR mutations, such as H46R/H48Q, H80R and D125H, interfere with the protein's ability to bind copper or zinc and thus preclude enzymatic activity. MBR mutations generally occur in the histidine residues that directly coordinate the metal ions or in the electrostatic loops that surround the metal binding region. However, both WTL and MBR mutations lead to the development of ALS.

There are relatively few common properties between the different SOD1 mutations. Metal binding ability, protein stability aggregation propensity, and life expectancy of human patients are all highly variable between the different mutations [34, 35]. **Table 1.1** provides a summary of the known biophysical properties of the SOD1 mutations used in this work and demonstrates the wide variability in SOD1 mutations that cause ALS [16, 33, 35-38]. The large differences between the various mutations have made discovering the role of mutant SOD1 in ALS extremely difficult.

TABLE 1.1 List of SOD1 mutations used in this study with their respective biophysical properties.

SOD1 Mutation	Mutation Type	Location	% Activity of WT	Copper Binding Per Dimer	Zinc Binding Per Dimer	Survival Time in Humans (years)[35]	Degree of Aggregates at 24 hrs[35]	Stability[35]
WT	NA	NA	100%	88%[36]	100%[36]	NA	None	High
A4V	**WTL**	Dimer interface	~100%[16]	48%[33]	> 90%[33]	1.2 ± 0.9	High	Low
G37R	WTL	Loop	~75%[36]	85%[33]	100%[36]	18.7 ± 11.4	Moderate	High
H46R	**MBR**	Cu Binding	~1%[16]	~1%[33]	~3%[33]	17.0 ± 7.0	Moderate	High
H48Q	MBR	Cu Binding	~1%[16,33]	> 79%[33]	64%[33]	1.1	Moderate	High
H80R	**MBR**	Zn Binding	~6%[16]	~16%[16]	~35%[16]	ND	Low	ND
G93A	WTL	β-barrel	~100%[33]	77%[33]	> 90%[33]	2.4 ± 1.4	High	Low
D125H	**MBR**	Charged Loop	~26%[16] ~17%[33]	15%[33]	21%[33]	0.7	Low	Low
L126Z	WTL	Truncation	~30%[37]	Low[35]	ND	> 4[38]	Extreme	Low

1.4 Hypotheses on the Role of SOD1 in ALS

The precise role of SOD1 in ALS is currently unknown, though several hypotheses speculate on how the array of known mutations to SOD1 can have such a dramatic effect on motor neurons. Due to the decline in functional ability of many SOD1 mutations, it was originally hypothesized that SOD1-related ALS resulted from a loss of function of SOD1 [39, 40]. However, because many point mutations, such as G37R and G93A, maintain high levels of antioxidant activity [41, 42]; and the expression of WT SOD1 coexpressed with mutant SOD1 does not rescue the ALS phenotype in mice [43, 44], this original hypothesis has subsequently been revised. Based on key observations, it is now well accepted that the development of ALS is not based on a loss of function of SOD1, but rather a gain of function [41]. The gain of function hypotheses propose that SOD1 has added function(s), such as increased aggregation propensity, aberrant copper chemistry and/or the acquisition of pro-oxidant properties that contribute to ALS and the deterioration of motor neurons [45].

1.5 Oxidative Stress

Oxidative stress is a hallmark feature found in the spinal cords and cerebrospinal fluid (CSF) of sporadic and familial ALS patients [46-48]. Oxidative stress is the result of an imbalance in the production of ROS and the cell's ability to counteract ROS production with antioxidants like SOD1 [49]. Most cellular ROS arise from the mitochondrial respiratory chain. In the mitochondria electrons are 'leaked' by the incomplete reduction of molecular oxygen (O_2) producing superoxide ($O_2^{\cdot -}$) and hydrogen peroxide (H_2O_2) during oxidative phosphorylation. Both $ONOO^-$, the product of superoxide and nitric oxide, and $\cdot OH$, the dissociation of H_2O_2, are highly reactive oxidizing agents capable of damaging unsaturated fatty acids in the cell

membrane, altering DNA and RNA species and changing protein conformation [49]. It is unclear whether oxidative stress is a primary cause of ALS or a result of some other toxic event, but it is a key component in the progression of the disease.

One of the proposed gains of function for mutant SOD1 is to become a pro-oxidant rather than an anti-oxidant [50]. It is hypothesized that SOD1 can increase the number of ROS, possibly due to aberrant copper chemistry, that have damaging and toxic consequences for the living cell. For example, increased peroxidase activity has been found in mutant SOD1 in which hydrogen peroxide (H_2O_2) [51, 52], a product of superoxide disproportionation, is converted to a hydroxyl radical by Cu^+. Alternatively, SOD1 mutants can interact with new substrates such as peroxynitrite ($ONOO^-$) to increase the rate of oxidative damage [53].

Several other factors can contribute to the production of ROS that could lead to the oxidative damage seen in ALS patients. ROS can increase with age, possibly through an increasingly 'leaky' mitochondrial respiration [54]. This could be related to the onset of ALS later in life. With a compromised mutant SOD1, the increase in ROS may be too difficult to handle for other antioxidant proteins, such as SOD2 (manganese SOD) and glutathione peroxidases [49]. Additionally, the response of the endoplasmic reticulum (ER) to misfolded proteins, such as SOD1, can increase the rate of ROS production [55, 56]. The primary source of the elevated ROS and oxidative damage in ALS is unknown, though numerous factors could contribute to the increase and lead to oxidatively modified proteins, DNA and lipids.

1.6 AGGREGATION OF SOD1

Mutant SOD1 forms aggregates in the affected motor neurons of ALS patients. These aggregates are largely β-sheet in structure and similar to the protein aggregates found in other

neurodegenerative disorders, including Alzheimer's disease and Parkinson's disease. Protein aggregates can interfere with axonal transport, protein degradation, and mitochondrial function [2]. Aside from SOD1, the aggregates also contain ubiquitin and several heat-shock proteins [43, 57], indicating a failure to properly fold.

Most current aggregation hypotheses in ALS regard aggregates as cytoprotective, serving as a defense mechanism to remove the soluble and possibly more toxic form of SOD1 from the cytosol. This hypothesis is supported by the lack of correlation between aggregate formation and cell death [58, 59]. Given the of most holo-SOD1 mutations, it is also hypothesized that aggregates are formed by the unmetallated and nascent protein. Indeed, SOD1 aggregates lacked many of the post-translation modifications found in the mature protein [60]. This suggests that the aggregated SOD1 is not fully activated and thus aggregates are formed before the toxic mature mutant SOD1 has a chance to react with its environment.

1.7 The Role of Copper

Copper is an essential catalytic center for many metalloenzymes, including SOD1. Both copper overload (Wilson's disease) and copper deficiency (Menkes disease) are potentially fatal and have significant impacts on the central nervous system (CNS). As a redox-active metal, copper is tightly regulated to eliminate aberrant reactions that can result in the production of damaging reactive oxygen species (ROS). It has been hypothesized that the toxic gain of function could involve improper reactions of copper in SOD1 with its surroundings [61].

Aberrant copper hypotheses are based on evidence that the copper ion is inappropriately exposed in mutant SOD1. Specifically, the copper ion may not be properly bound to the copper site. In experiments with zinc deficient SOD1, the copper ion becomes more accessible in the

destabilized protein and is extremely toxic to cultured motor neurons [62, 63]. Some mutations, such as G85R, do not directly affect the binding of metal; but X-ray crystallography studies show they do expose the copper site more than in the WT protein [64]. In the MBR mutations copper is capable of binding to zinc site. A lab-generated "quad" mutant that removes all four copper-coordinating histidine residues showed a strong affinity for metals, including copper [63].

In addition to copper in the metal binding sites of SOD1, a noncanonical copper binding site has been found on a surface cysteine (Cys111) residue [65]. Both WTL and MBR have been shown *in vitro* to bind copper at this site [66]. This residue is highly exposed to the cytosol and could be a source of aberrant copper chemistry that could lead to the increase in ROS found in ALS.

CCS provides further evidence for the role of copper in ALS. The CCS protein has also been proposed as a source of copper for both WTL and MBR mutations, as it can form stable dimers with SOD1 mutations [45]. Also, the expression of human CCS and human G93A SOD1 in mice resulted in dramatic reduction in survival time from about 242 days to 36 days, while mice expressing human CCS and human WT SOD1 showed no change in survival time and appeared asymptomatic or normal [67].

These experiments demonstrate the importance of copper in ALS. When improperly controlled, redox-active copper can have deleterious effects on the cell and may be a source of the proposed gain of function in mutant SOD1.

1.8 The Role of Zinc

Similar to copper, zinc is also an essential element to cellular processes, and it is toxic at both high and low doses. Zinc is responsible for the stability of SOD1 and can also function in

the cell as a neurotransmitter. In contrast to copper, zinc is not redox active and is generally considered more inert, as it cannot catalyze the production of ROS. As a result, it is not always chaperoned, and free zinc can be found in the cell. Many SOD1 mutations show decreased zinc binding affinities regardless of the location of the mutation (MBR or WTL) [68]. Reduced zinc affinity could lead to an alteration in cellular zinc levels that can cause a wide range of consequences. An imbalance of zinc homeostasis is hypothesized to be a factor in oxidative stress, glutamate excitotoxicity, and protein aggregation in ALS [69].

Zinc is capable of inducing oxidative stress at high concentrations, where it can inhibit energy production in the mitochondria, leading to an accumulation of ROS [70]. In ALS SOD1 is often found in the mitochondria, and mitochondrial abnormalities are seen in patients and mice, indicating that damage is occurring within this organelle [41, 71]. Excess zinc can also promote the noninducible nitric oxide synthase that can lead to the production of NO and can in turn be converted by superoxide to $ONOO^-$, a highly reactive species [72]. While zinc is not directly capable of catalyzing ROS, it is capable of promoting oxidative stress.

Glutamate excitotoxicity is seen in ALS and is tightly coupled to zinc. Excitotoxicity occurs when glutamate induces the release of calcium through N-methyl-D-aspartate (NMDA) receptors and α-amino-3-hydroxy-5-methylisoxazole-4-propionic acid (AMPA) receptors [73]. As a result, the reduced glutamate uptake found in ALS patients encourages excitotoxicity. The increase in calcium leads to the release of zinc that further enhances the activity of AMPA receptors. Riluzole, the only approved drug for ALS, is a glutamate inhibitor; but it only increases the life expectance of ALS patients by about three months. While this is a small increase in life expectancy, it does indicate the importance of glutamate excitotoxicity in ALS.

SOD1 aggregation can also be influenced by zinc. Zinc deficient SOD1 is highly prone to aggregation [74]. It is hypothesized that the weakened zinc-binding site of mutant SOD1 can result in reduced stability and increased aggregation propensity. It has also been shown that zinc can induce the aggregation of other misfolded proteins found in Alzheimer's disease [75]. Thus, if aggregates sequester toxic soluble proteins, then this role of zinc would be considered neuroprotective.

1.9 Overview of Methods

1.9.1 Synchrotron X-ray Fluorescence Microscopy (XFM)

Synchrotron micro-XFM enables the localization and quantification of metal ions with in a specimen to better understand the role of metal ions in ALS. XFM has the advantage of being a non-destructive, non-contact method for precise, localized micro-analysis of trace elements [76]. The phenomenon begins when an X-ray photon of sufficient energy encounters an electron within the core shell and ejects an electron. An electron from an outer shell relaxes into the inner shell to fill the hole, releasing a photon of lower energy in the process. The release of the photon is the source of the X-ray fluorescence [76]. Each element has characteristic photoemission energy lines; and a full energy dispersive spectrum is acquired at each point, making it possible to quantitatively distinguish between many different elements simultaneously, as shown in **Figure 1.3**. XFM with a synchrotron source provides the high brightness needed to collect data efficiently, and the broadband white light from the synchrotron allows for a tunable energy range that allows for spectroscopic measurements.

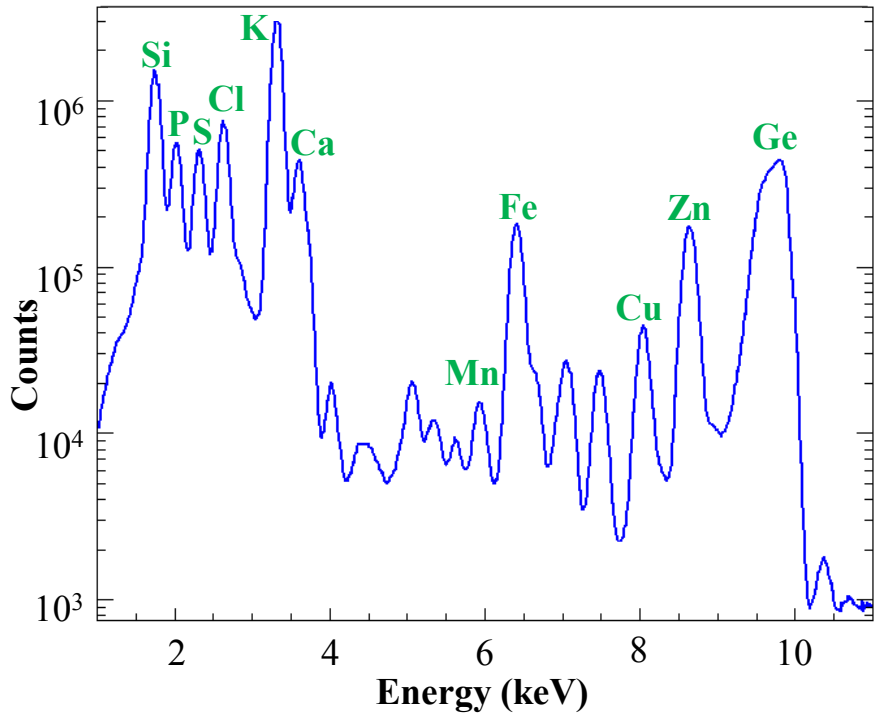

FIGURE 1.3 A typical XFM spectrum from a biological specimen at 10 keV showing silicon from the silicon nitride windows; germanium from the detector; and phosphorus, sulfur, chlorine, potassium, calcium, iron, manganese, copper, and zinc from the specimen. The unlabeled peaks are either very trace levels of other elements or the Kβ peaks (smaller contributions) of the labeled elements.

An XFM beamline is equipped with a monochromator, focusing optics, a moveable sample stage, and a detector. A schematic of a typical XFM end station is depicted in **Figure 1.4** [77]. The monochromator is used to select the energy of the incident X-ray beam and is generally made of a silicon crystal. Next, the beam is focused using either Kirkpatrick-Baez (KB) mirrors or zone plates. The energy must be greater than the excitation energy of the largest (greatest Z) element of interest. A pair of parabolic KB mirrors can be used to focus the X-ray beam in the horizontal and vertical directions, and are capable of achieving a spot size on the order of a few μm to a few hundred nm. Zone plates consist of a circular diffraction grating of increasing line density towards the center of the lens. Zone plates offer higher resolution than KB mirrors (40-

500 nm), but zone plates are less efficient (<20%) and have a short working distance (~1 cm)

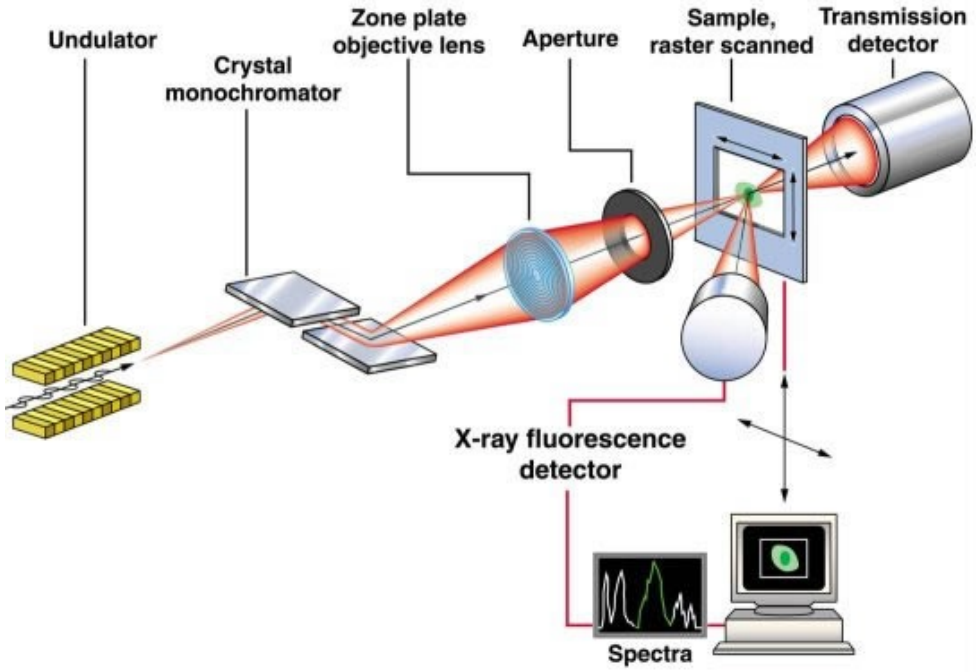

FIGURE 1.4 Schematic of an XFM end station depicting the light coming from the undulator of the synchrotron to the crystal monochromator to choose the energy of the incident beam, which is then focused using zone plates (or KB mirrors). The sample is raster scanned with respect to the beam, and the fluorescence detector is located at a 45 degree angle with respect to the sample and a 90 degree angle with respect to the incident beam. A transmission detector can also be used to acquire information such as phase contrast. The signals from the detector(s) are relayed to a computer where the data is processed and stored [77].

that is highly dependent on the energy of the incident beam. KB mirrors have higher efficiency (70-90%), much longer working distance (~10 cm), and are achromatic so the focal distance is not energy dependent. Once focused, the incident beam encounters the specimen, which is placed at a 45-degree angle with respect to the beam. The stage can move the specimen in the horizontal (x) and vertical (y) directions to raster scan the specimen, creating a map; and in the z direction, to ensure that the specimen is placed at the focal point of the X-rays where the spot size is the smallest. After the incident beam interacts with the specimen, a liquid nitrogen-cooled detector, positioned at a 90-degree angle from the incident beam, measures the fluorescent photons and

their respective energies. This geometry avoids interference with the transmitted X-rays and provides maximum detection of the of the X-ray fluorescence.

X-ray absorption spectroscopy (XAS) is a technique that can utilize the same end-station configuration as XFM, but is used to probe the oxidation state and coordination of metal ions. XAS is performed by gradually increasing the energy of an incident monochromatic X-ray beam on to a specimen. The energy is varied from below the absorption edge of an element of interest to well above the edge. Below the absorption edge there is insufficient energy to excite electrons from the element of interest so there is little absorption. Once the energy is high enough there is a sharp increase in the absorption, creating the absorption edge. This region of the spectrum is known as X-ray absorption near-edge structure (XANES) and extends from a few eV before the absorption edge to about 50 eV above. XANES can provide information about the oxidation state of the element, as the position of the absorption edge varies a few eV with change in oxidation state. After the XANES region is the extended X-ray absorption fine structure (EXAFS) region, which continues on for an additional 1000 eV after the absorption edge. EXAFS shows the interference between the emitted photoelectron and the neighboring atoms, creating a backscattering effect. The backscattering can provide structural information within approximately a 5 Å radius of the atom of interest [78]. **Figure 1.5** shows a typical XAS spectrum over the iron K-edge, indicating the XANES and EXAFS regions. Synchrotron radiation is needed for XAS for its high, uniform flux over a range of tunable energies to obtain adequate signal to noise in a relatively short amount of time. The broad range of the synchrotron light allows for a variable amount of energy to be used with a monochromator to scan over the absorption edge of an element of interest [78]. XAS has been useful in studying active sites of proteins and variations of ligand binding [76].

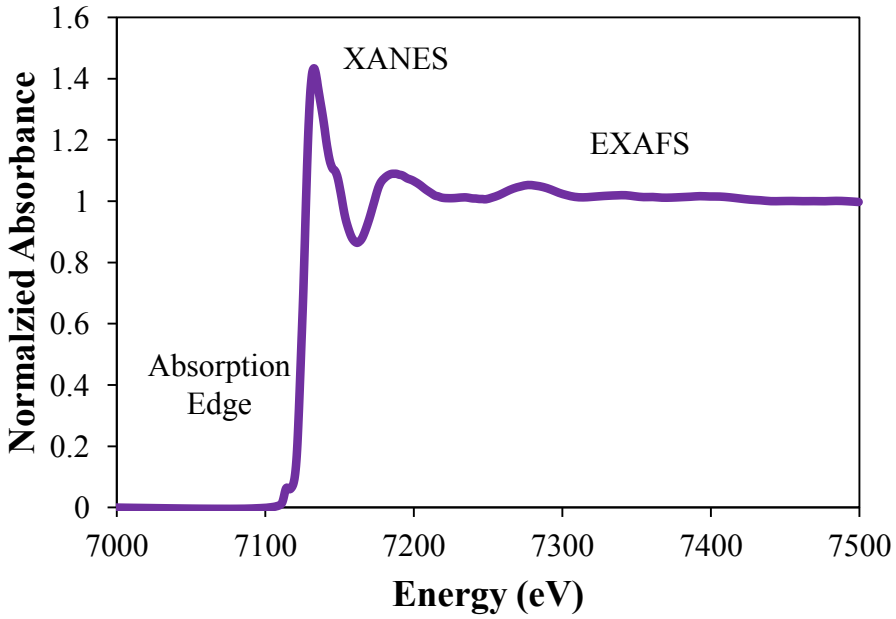

FIGURE 1.5 An iron XAS spectrum of ferritin, an iron storage protein that shows the absorption edge, XANES, and EXAFS regions. These regions provide information about the oxidation state and coordination of the iron in the specimen.

For XFM techniques, sample preparation for biological tissues generally involves thin tissue sections or cryosections. Cryosections should be as thin as possible, while still maintaining a high enough concentration of the elements of interest to be readily detectable. For example, copper is present in very low concentrations in biological materials. Thus, for these experiments spinal cord sections were cut to 20 µm, which is the minimum thickness to allow for the detection of copper. Thin sections are placed onto a thin, trace-metal free, X-ray transparent substrate, such as silicon nitride windows (Silson, UK) or Ultralene film (SPEX CertiPrep, Metuchen, NJ). The thin substrate reduces the level of scatter from the transmitted X-rays. Silicon nitride windows are 500 nm thick and 2.5 x 2.5 mm in size. They have a thicker frame that provides more structural stability and enables the substrate to be handled. The Ultralene film is 4 µm thick and is made into a ring shape using 1 mm thick Delrin (polyoxymethylene) rings that are about 1 inch (inner diameter) in diameter. To do this, Ultralene is stretched tightly and taped to a solid surface, ensuring there are no ripples or waves, and the rings are glued on to the

Ultralene with the white/gray epoxy (3M Scotch-Weld, St. Paul, MN). The epoxy is allowed to dry overnight and is then cut out of the Ultralene sheet. This produces a flat Ultralene ring that enables the substrate and specimen to be handled and mounted on a beamline stage. For cell culture experiments, cells can be grown directly on to a suitable substrate. Silicon nitride windows and Ultralene rings (including Delrin and epoxy) do not affect cell growth. A monolayer of cells is ideal to avoid analyzing multiple or a varied number of cells, and the monolayer has sufficient copper to detect in an XFM measurement. Cells are rinsed with phosphate buffered saline (PBS) and fixed rapidly by dipping in cold methanol. All biological specimens are allowed to dry and stored in a desiccator until measurements are made at the beamline to prevent the deterioration of the sample.

XFM experiments were performed at beamline X27A in the National Synchrotron Light Source (NSLS) at Brookhaven National Laboratory (BNL) (Upton, NY). X27A uses a single crystal Si(111) monochromator to select the energy of the incident X-ray beam (12 keV). KB mirrors are used to focus the beam down to approximately 9 (vertical) by 15 (horizontal) μm and uses a 13-element germanium detector (Canberra). This beamline was used for imaging larger tissue areas, such as the mouse spinal cords discussed in **Chapter 3** and for XAS measurements on the Alzheimer's disease (AD) plaques discussed in **Chapter 5**. Beamline X3B, also at the NSLS, was used to collect XAS standards of iron-containing proteins (**Chapter 5**) to determine the types of iron-containing proteins in the plaques. X3B is equipped with a single crystal monochromator; KB-focusing mirrors; a cryo-cooled sample chamber, to minimize damage to the protein standards; and a 32-element germanium detector (Canberra). For high-resolution single cell experiments (**Chapter 2**), beamline 2-ID-E was used at the Advanced Light Source (APS) at Argonne National Laboratory (Argonne, IL). This beamline has a Si(111)

monochromator to tune the energy to 10 keV. Zone plates are used to focus the beam down to 500 by 500 nm, and an silicon drift four element detector. Beamline 18-ID-D was used to collect data on the AD plaques (**Chapter 5**). This beamline utilizes a double crystal Si(111) monochromator. K-B mirrors focus the beam to a 5 by 5 μm spot size, and a single element silicon drift detector (Ketek) detects the X-ray fluorescence. The high flux from 18-ID-D enables rapid scanning of larger areas with very short dwell times (0.5 sec).

1.9.2 Fourier Transform Infrared Microspectroscopy (FTIRM) and Imaging (FTIRI)

FTIR provides valuable information regarding the chemical composition of a specimen, which can provide insight into the formation of aggregates and the extent of oxidative damage to lipids. FTIR is a type of vibrational spectroscopy used to probe the vibrational modes of molecules. Infrared (IR) radiation can be absorbed by molecules when the frequency of radiation is equal to that of the natural frequencies at which the molecule vibrates. IR absorption requires molecules to have vibrational modes that contain a net dipole change, such as those containing C-H or C=O bonds. When the radiation is absorbed a transition from one vibrational or rotational state to another occurs. This is seen in the IR spectrum of a molecule [79].

An FTIR spectrometer can be coupled to a microscope to produce spatially resolved data. This is especially important for biological specimens, which contain distinct anatomical regions that are composed of different materials, making them unsuitable for bulk analysis. For example, the spinal cord consists of white matter and gray matter, which are primarily composed of lipids and proteins, respectively; and the disease affects each area in a different manner. Thus, it is critical to obtain spatially resolved information. FTIR microscopes are categorized into two

different techniques: FTIR microscopy (FTIRM) and FTIR imaging (FTIRI). In FTIRM a single element mercury cadmium telluride (MCT) detector is typically used; and an aperture is used to determine the spatial resolution on the sample, which is diffraction-limited (2-10 μm) [80]. A specimen is raster scanned over a region of interest (ROI) and a spectrum is collected at each point. In contrast, FTIRI utilizes a focal plane array (FPA) detector that consists of numerous detector pixels. This technique floods the specimen with IR light, rather than using an aperture. FTIRI is faster than FTIRM, as an entire imaged is collected simultaneously rather than one pixel

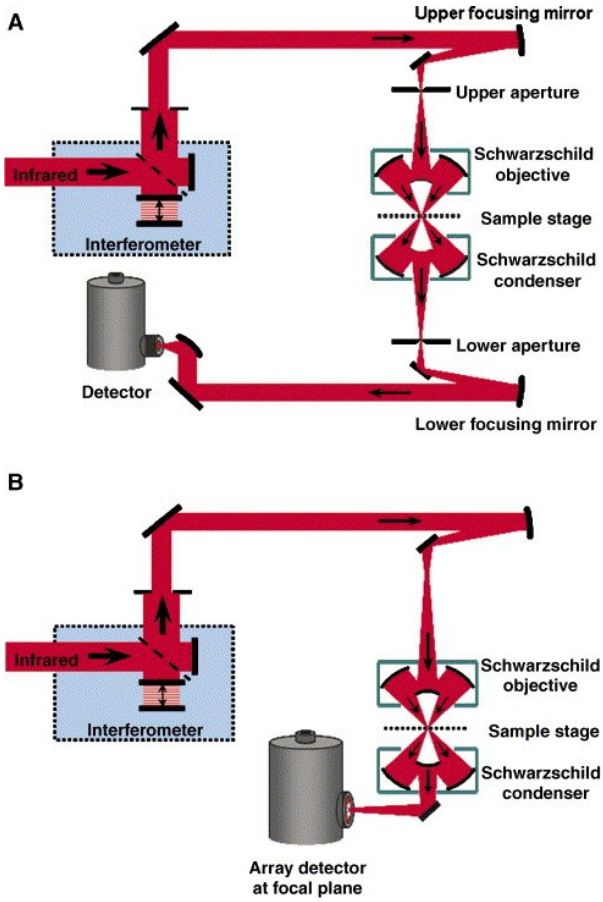

FIGURE 1.6 Schematic of FTIR set up for FTIRM with an MCT detector (A) and FTIRI with an FPA detector (B). FTIRM uses an aperture to determine the spot size of light that is then sent through a Schwarzschild objective, the specimen, and through a second Schwarzschild objective and aperture to a single element MCT detector. For FTIRI, IR light is sent through the Schwarzschild objective, the sample, and a second Schwarzschild objective without the use of an aperture. The light is then imaged onto the FPA detector [82].

at a time. The signal to noise ratio from an FPA is generally better than an MCT detector, but the spatial resolution may be reduced by pixel to pixel blurring [81]. **Figure 1.6** is a schematic of FTIRM and FTIRI setups, showing the light coming from the interferometer through the focusing Schwarzschild objectives and on to the detectors [82].

A synchrotron IR source can provide several significant advantages over a traditional globar source. First, the high brightness of the synchrotron source is approximately 100-1000 times greater than a globar [82]. Thus the amount of time required to collect data with sufficient signal to noise is greatly reduced. Second, the synchrotron beam is collimated to about 20 μm spot size, allowing for a smaller area to be probed down to the diffraction limit with FTIRM and with a good ratio of signal to noise. With a globar source an aperture is typically set between 20 and 100 μm; but below 20 μm the intensity of light is greatly reduced, causing poor signal to noise. Therefore, the brightness of a synchrotron source can improve the signal to noise ratio, reducing the amount of time needed to collect an acceptable spectrum; and it can be focused to a smaller spot size, generating improved spatial resolution.

For biological materials, such as tissues and cells, IR can be a very useful technique providing information regarding the proteins, lipids and nucleic acids. **Figure 1.7** shows a typical FTIR spectrum from a biological specimen. The protein content can be determined using the amide I (1600-1710 cm^{-1}) and amide II (1500-1560 cm^{-1}) bands which arise from the C=O and C-N stretch of the protein backbone, respectively. The integrated values under these peaks are directly proportional to the amount of protein in a specimen. This is useful for determining the relative increase in protein density within an aggregate compared to the surrounding cell or tissue area, which can then be used to normalize data obtained using XFM to avoid over estimating the

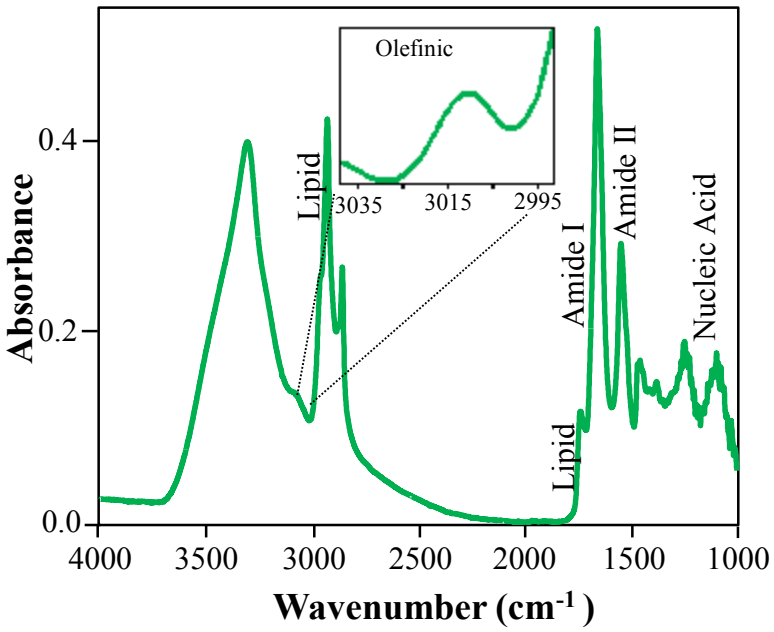

FIGURE 1.7 A typical FTIR spectrum from a biological specimen, containing the lipid region, based on the C-H stretch (2750-3025 cm^{-1}) and C=O stretch (1736 cm^{-1}), the amide I region from the C=O (1600-1700 cm^{-1}) stretch and the amide II region C-N stretch (1500-1560 cm^{-1}) from the protein backbone, and the nucleic acid region from the PO_2^- stretch (symmetric: 1224 cm^{-1} and asymmetric: 1087 cm^{-1}). The olefinic region from the C=C-H stretch (2995-3025 cm^{-1}) is expanded in the inset.

metal content within a plaque due to the increased density [83]. Protein secondary structure can also be determined using the amide I band due to involvement of the protein backbone carbonyl in the hydrogen-bonding network. Thus, the position of the amide I peak is affected by protein secondary structure. A protein rich in β-sheets (1630 cm^{-1}) will have an amide I peak that is shifted to smaller wavenumbers than a more α-helical (1655 cm^{-1}) protein [84, 85]. Many diseases, including ALS, involve misfolded proteins or proteins that change conformational structure and develop into aggregates. IR is a sensitive technique that can be used to understand the mechanisms of protein misfolding and aggregation.

The composition of lipids can also be determined using IR based on the C-H (2800-3000 cm^{-1}) stretching mode in the long aliphatic chain. This can be especially useful in separating the

lipid-rich white matter and the proteinaceous gray matter of the spinal cords when generating ROIs for XFM data analysis. The lipid region of the IR spectrum is also sensitive to the type of lipid observed. For example, the level of unsaturated lipids can be determined based on the olefinic peak (3012 cm^{-1}) that arises from the =C-H stretch of a double bonded carbon [86, 87]. Unsaturated lipids are especially prone to oxidative damage, in which the carbon-carbon double bond is reduced to a single bond by ROS. The relative decrease in unsaturated lipid content is an indication of oxidative damage that is seen diseases such as ALS.

Sample preparation for FTIR is relatively straightforward. Tissue sections are typically cryosectioned to about 10 μm thick, which avoids the saturation of the comparatively tall amide I peak. The IR measurements in this dissertation were all performed in a transmission geometry so cryosections from tissue specimens are placed on an IR transparent material, such as CaF_2 (Korth Kristalle, Germany) or Si_3N_4, to allow the IR light to pass through the specimen and substrate. A monolayer of cells is generally thinner than 10 μm so cells can be grown directly on an IR suitable transparent substrate. Both CaF_2 and Si_3N_4 are reasonably insoluble in water and are non-toxic to the cells. Cells are rinsed with PBS and fixed with methanol to avoid any changes to the cellular morphology without altering the chemical makeup of the cells. All specimens are allowed to dry at room temperature and stored in a desiccator to slow the degradation of the tissues, which can be accelerated in a more humid environment.

FTIR experiments presented in this dissertation were performed at the NSLS. FTIRI measurements on ALS mouse spinal cord cross sections were made on a Bruker Hyperion at beamline U10B for lipid unsaturation levels (**Chapter 4**) and the PerkinElmer Spotlight for PCA analysis (**Chapter 3**). These microscopes provided a rapid method for collecting data on the relatively large spinal cords specimens, while maintaining suitable spatial resolution to

discriminate between the white and gray matter. A Thermo-Nicolet Continμum at beamline U2B was used for all FTIRM measurements to determine the protein density inside the aggregates (**Chapter 2**) and amyloid-β plaques (**Chapter 5**). The small aperture (7 μm) allowed for point spectra to be taken on and off the aggregates or plaques with this method.

1.9.3 ALS MOUSE MODELS

To better understand the disease progression and symptoms of ALS, several transgenic mouse models have been created that mimic the disease. The most common mouse models of ALS involve transgenic mice overexpressing mutations in the protein SOD1. Numerous, well characterized SOD1 mouse models have been created based on several different point mutations in SOD1. These mice developed SOD1 aggregates in their motor neurons and experience progressive degeneration of their motor neurons, leading to paralysis and death [43, 88]. Interestingly, SOD1 knock-out mice fail to develop ALS [89], but the expression of mutated mouse SOD1 (G86R) does result in the ALS phenotype [90]. These findings contributed to the SOD1 gain of function theory in ALS. More recently, with the discovery of the link between TDP-43 and ALS, mouse models have been created that affect the expression rates of human TDP-43 or overexpress mutations of the protein. Mice overexpressing WT TDP-43 lack the cytoplasmic protein inclusions but do show neurodegeneration [91]. However, mice overexpressing TDP-43 mutations show gait abnormalities, paralysis, and reduced survival rates similar to ALS [92]. This effect is exacerbated when TDP-43 mutations are overexpressed with WT TDP-43 [93]. Most mutant TDP-43 mice develop aggregates in the motor neurons, and TDP-43 knockout mice and mice deficient in TDP-43 are not viable [94]. While SOD1 and TDP-43 transgenic mouse models are the most common, other models have been developed by

affecting intermediate filament organization [95-97], microtubule-based transport [98-100], and endosomal trafficking deficits [101-103] that demonstrate motor neuron loss, muscle weakness and/or abnormal gait.

In this dissertation, transgenic mice were used that overexpress mutations in the human SOD1 protein, similar to the mutations found in SOD1-linked ALS patients. Five transgenic mouse lines were used: G37R [line 29] [41], G93A [B6SJL-TgN (SOD1-G93A)1Gur; The Jackson Laboratory] [104], H46R/H48Q [line 139] [105], L126Z, and WT [line 76] [41], as well as a non-transgenic (NTG) control. The transgenic mice over-express human SOD1 approximately 10 fold, and the expression of their own mouse SOD1 is not altered. Transgenic mice were sacrificed at the end-stage of the disease (~ 6-7 months old) when they were completely paralyzed. Mice expressing WT human SOD1 do not develop ALS symptoms and were also sacrificed around 6-7 months, as were the NTG mice. Mice were anesthetized and perfused with PBS. To extract the spinal cords the vertebral column was removed, and a syringe filled with PBS was used to push the spinal cord out of the column. The spinal cords were placed in Eppendorf tubes (Eppendorf, Germany) containing 4% paraformaldehyde to preserve the integrity of the samples and stored in a cold room (4 °C).

1.9.4 CYROSECTIONING

Cryosectioning allows for thin (10-30 μm) sections of uniform thickness to be cut from tissues for imaging or staining experiments. Mouse spinal cords were soaked overnight in a 20% sucrose solution to improve the quality of the sections. The spinal cords were then quickly frozen over liquid nitrogen and embedded in optimal cutting temperature (OCT) (Tissue-Tek, Sakura, Japan) compound. Transverse sections of mouse spinal cords from the lumbar or sacral segments

were cut using a cryo-microtome (Leica, Germany) at -15°C. The thin sections were carefully flattened using a small paint brush and transferred to the substrate. Once the section was positioned on the substrate, it was removed from the cryotome and warmed quickly to room temperature, drying-out in the process. After drying completely, cryosectioned specimens were stored in a desiccator until imaged. After cryosectioning of a specimen is complete, the unused embedded tissue was covered with more OCT on the exposed surface to prevent damage or ice formation on the tissue and stored in a -80°C freezer. For FTIR experiments, 10 μm sections were cut and placed onto calcium fluoride (CaF_2) slides, which is an infrared transparent material. Additional sections were cut to 20 μm thick and placed on Ultralene film for XFM experiments. Ultralene is a thin (4 μm), trace metal free substrate used to avoid interference from excess X-ray scattering and metals in the substrate, and described in more detail in section 1.9.1.

1.9.5 CELL CULTURE

Cell culture models of ALS provide a relatively simple and rapid study in comparison to mouse models. Several cell lines have been transfected to express SOD1, including human motor neurons [106, 107], human embryonic kidney 293FT cells [35], pluripotent stem cells from ALS patients [108], and Chinese hamster ovary cells (CHO-K1) [109]. Many eukaryotic cells can be readily transfected to express human SOD1 (WT or mutant) coexpressed with a yellow fluorescent protein (YFP) tag that enables the visualization of transfected cells and their intracellular aggregates [35, 109]. For the experiments presented here, CHO-K1 cells (ATCC, Manassas, VA) were transfected to overexpress SOD1-YFP. The cells that overexpress mutations in SOD1 develop intracellular aggregates similar to those found in the motor neurons of patients with ALS. This cell line was chosen based on its tendency to grow as a monolayer.

The stacking of multiple cell layers severely complicates XFM data and analysis. This cell line is also readily transfected with high efficiency, providing numerous transfected cells for mapping.

CHO-K1 cells were grown in F12-K medium (ATCC) with 10% fetal bovine serum (FBS) and 1% penicillin/streptomycin (Sigma-Aldrich, St. Louis, MO) added to make the complete medium. The cells were cultured in 10 cm petri dishes with 10 mL of the complete medium and stored in a sterile cell culture incubator at 37 °C with 5% carbon dioxide (CO_2) and 95% humidity. All cell culture work was performed in a UV-sterilized HEPA filtered cell culture hood. The cells were split every two to three days, by removing the medium, rinsing the cells with 2 mL of PBS, and removing the PBS. Subsequently, the cells were trypsinized with 2 mL of trypsin-ethylenediaminetetraacetic acid (EDTA) (Sigma-Aldrich, St. Louis, MO) added to the dish, and approximately 1.5 mL was removed. The dish was returned to the incubator for 5-10 minutes, allowing the trypsin to detach the cells from the dish, which was verified by a light microscope. After the cells detached from the dish, they were re-suspended in 5 mL of media, and this volume was split between two new 10 cm petri dishes and 7.5 mL of fresh media was added for a total volume of 10 mL of media. The dishes were then returned to the incubator.

1.9.6 TRANSFECTION

Transfection is a technique that is frequently used to generate cell culture models of disease, such as SOD1-ALS. Transfection involves the insertion of foreign DNA into a cell and results in the overexpression of a desired protein(s). In this dissertation, cells are transfected to over express mutant or WT SOD1, which was coexpressed with YFP to allow for the visualization of the transfected cells with epifluorescence microscopy. To transfect the cells, the same splitting and trypsinization procedure is followed, as detailed in section 1.9.5. However,

instead of 2.5 mL of resuspended cells added to the new dish, 0.5 mL of resuspended cells was added to each of six 3 mL wells in a 6-well plate. Two silicon nitride windows were placed inside each well, measuring 2.5 mm x 2.5 mm with 500 nm thick membrane that were sterilized by dipping in 80% ethanol and air drying in a sterile HEPA-filtered cell culture hood. Once the cells have been added to the well, an additional 2 mL of media is added to each well for a total volume of 2.5 mL of medium. With 0.5 mL of cells there are a sufficient number of cells of which many will attach to the silicon nitride windows. The cells are allowed to sit overnight and attach to the dish and windows. After being seeded onto the silicon nitride windows, the cells were transfected at approximately 90% confluence, using Lipo-D293 transfection reagent (Signa-Gen Laboratories, Rockville, MD), which permeablizes the lipid membranes of the cells allowing the DNA plasmid to enter the nucleus. The DNA plasmids were generously donated by the lab of Dr. David Borchelt. Each plasmid contained SOD1 (WT, A4V, G37R, H80R or D125H) co-expressed with yellow fluorescent protein (YFP). The transfection procedure is as follows: medium was removed from each well in the 6-well plate and replaced with 1 mL fresh complete medium. Three μL of lipo-D293 transfection reagent were added to 50 μL of medium without FBS in an Eppendorf tube. In a separate Eppendorf tube, 1 μg of DNA plasmid was added to 50 μL of medium, also without FBS. Each tube was quickly vortexed and spun down for three seconds allowing the solution to collect at the bottom of the tube. The transfection reagent solution was immediately added to the DNA plasmid solution, vortexed and spun-down for three seconds again to mix and collect the solution, which was then incubated for 15 minutes at room temperature. After incubation, the DNA/transfection reagent mixture was added to one of the wells in the 6-well plate with a micropipette, and the cells were then returned to the incubator. Cells were monitored beginning 18 hours after transfection began, and the transfection

was stopped once the majority of cells were fluorescent with YFP (19-26 hours). To stop the transfection, the silicon nitride windows were rinsed in PBS and dipped in cold (~80 °C) methanol three times for one second each time. The windows were allowed to dry at room temperature and were stored in a desiccator until imaged.

1.10 Specific Aims and Hypotheses

Altered metal homeostasis is suspected to play a role in many neurodegenerative diseases, including ALS. In SOD1-linked ALS, mutations in the metalloenzyme are directly linked to the disease. Despite significant research, how SOD1 mutations cause ALS is currently unclear. Many *in vitro* studies have shown metal binding characteristics and aggregation propensities of the various SOD1 mutations, but it is unclear if these observations translate *in vivo*. In addition, many studies focus on only one mutation, making comparisons between different mutations difficult. The goal of this dissertation is to determine the role metals play in SOD1-linked ALS. Multiple MBR and WTL mutations in ALS mouse and cell culture models will be used to further understand how the wide variety of SOD1 mutations can cause ALS and, specifically, how the disease affects metal homeostasis and oxidative damage.

1.10.1 Specific Aim 1 – Metallation of Mutant SOD1 Aggregates and Metal Homeostasis in Cells Overexpressing SOD1

The effect of ALS on metal homeostasis in single cells with SOD1 mutations has not been extensively studied and could be heavily altered in the diseased state. The ability of SOD1 mutations to bind metal varies greatly between the WTL and MBR mutations. Thus, the metal ion levels may change with respect to the mutation. *We hypothesize that the metal homeostasis*

will be altered in the cells overexpressing SOD1 mutations. In addition, the formation of SOD1 aggregates is one of the hallmark features in patients with SOD1-linked ALS and could also affect the metal content within the cells. However, the manner in which aggregates form and their metallation state is not well understood. It has been shown that metallated mutant SOD1 is highly stable and not prone to aggregation, while the apo form of mutant SOD1 is significantly more likely to aggregate. Therefore, given the high stability of the metallated SOD1 and *in vitro* studies that suggest insoluble SOD1 lacks copper and zinc as well as post translational modifications, *we also hypothesize that the aggregates will be unmetallated*. *To test these hypotheses*, in **Chapter 2** we studied the metallation state of the SOD1 aggregates and the metal concentration and distribution in individual cells transfected to overexpress human SOD1 mutations (A4V, G37R, H80R, and D125H) in comparison to cells overexpressing WT SOD1 and untransfected cells using XFM. SOD1 was coexpressed with yellow fluorescent protein (YFP) that make locating transfected cells and their intracellular aggregates possible without the need for staining, which may alter some metal ion concentrations. The metal content inside the aggregates was normalized to the total protein content, determined by FTIRM, to account for the increased density within the aggregates. Examining metal concentration/distribution and the metallation state of SOD1 aggregates within single cells could aid in the understanding of how metal homeostasis is affected in ALS and how SOD1 aggregates are formed.

1.10.2 Specific Aim 2 – Metallation Levels and Metal Localization in the Spinal Cords Tissues of ALS Mice

Metal homeostasis is thought to be an important component in the progression of ALS [110]. This is in part due to studies that indicate an increase in copper levels in the erythrocytes

of sporadic and familial ALS patients [111, 112]. However, very little is known about how the metal concentrations are affected within the spinal cord and the motor neurons in ALS or if disease-dependent shift occurs in the localization of the metal ion levels. The presence of metal within the spinal cords may also be altered by the type of SOD1 mutation, where the spinal cords containing WTL may contain significantly more copper and zinc than the MBR mutations that are unable to bind these metals. *We hypothesize that WT mice or mice with WTL mutations will have increased copper and zinc in the gray matter of the spinal cord, where SOD1 is highly expressed, whereas the MBR mutations will not contain the same metallation levels. To test this hypothesis,* in **Chapter 3**, the localization of metals was determined using XFM on spinal cord cross sections of ALS (G37R, G93A, H46R/H48Q, and L126Z) mice with WT and NTG control mice. The same spinal cords were also analyzed for the metallation levels of soluble SOD1 using ICP-MS. In addition, the spinal cord tissues are composed of a network of different cell types than the cell culture model, which provides a more accurate model of ALS. This study demonstrated how SOD1 mutations affect distribution of metals in the spinal cord and metallation levels in SOD1 with respect to ALS.

1.10.3 Specific Aim 3 – Extent of Oxidative Damage in the Spinal Cords of ALS Mice

Oxidative stress is evident in sporadic and familial forms of ALS and has been found in several transgenic mouse models of the disease [46-48, 113]. The effects of oxidative stress can be observed in several ways, including the degree of protein carbonylation, which is a stable product of a reaction between proteins and ROS, or by the degree of lipid unsaturation. Unsaturated lipids are highly prone to oxidative damage that results in the reduction of the carbon-carbon double bond, creating a relative increase in saturated lipids where these reactions

have occurred. The results of previous oxidative damage studies have shown conflicting results between SOD1 mutations [43, 113]. However, these studies utilized different techniques to assess oxidative damage and each only examined one SOD1 mutation, hence the studies are not comparable. It is thought that one source of oxidative damage is catalyzed by the copper bound to SOD1 and its inappropriate reactions with its surroundings. *We hypothesize that WTL mutations will have more oxidative damage than MBR mutants and WT mice* because the WTL mutations are capable of binding copper, but the copper may be inappropriately exposed or loosely bound resulting in aberrant reactions and the production of ROS. *To test this hypothesis*, in **Chapter 4**, the extent of oxidative damage in proteins and lipids was analyzed with four different transgenic mouse models of ALS overexpressing a human SOD1 mutation (G37R, G93A, H46R/H48Q, and L126Z) and WT SOD1 and NTG controls. Levels of protein carbonyls were measured in the SOD1 extracted from spinal cords using densitometry measurements on an oxyblot. Lipid unsaturation was measured by FTIRI data to determine the level of oxidative damage to lipids. A comparison of WTL and MBR mutations will aid in understanding the of role oxidative stress in ALS and how mutations in SOD1 are involved.

CHAPTER 2

UNMETALLATED AGGREGATES AND DIMINISHED COPPER FOUND IN CELLS EXPRESSING SOD1 MUTATIONS THAT CAUSE ALS

2.1 ABSTRACT

Disruptions in metal homeostasis have been associated with amyotrophic lateral sclerosis (ALS) for several years, though the precise role of metals has yet to be ascertained. Metal ions are especially important to familial ALS cases caused by mutations in the metalloenzyme copper-zinc superoxide dismutase (SOD1). To investigate the role of metals in ALS and in the protein aggregates, we have examined the localization of metal ions in a cell culture model of ALS. Chinese hamster ovary (CHO-K1) cells were transfected to overexpress SOD1 coexpressed with yellow fluorescent protein (YFP) to readily identify the transfected cells and the intracellular aggregates that develop in the cells expressing mutant SOD1. The metal concentrations from four different SOD1 mutations (A4V, G37R, H80R, and D125H) that are associated with SOD1-ALS as well as a WT SOD1 control were measured, using X-ray fluorescence microscopy (XFM). The data showed that the intracellular aggregates were unmetallated, containing a net decrease in metal ion concentrations compared to the cytoplasm. These data agree with the recent *in vitro* studies that suggest SOD1 aggregates are composed of unmodified and unmetallated SOD1. Furthermore, all cells overexpressing mutant SOD1, regardless of the mutation's ability to bind copper and zinc, showed significantly reduced copper content compared to the WT SOD1 cells. Thus, no correlation was found between copper content and mutation type. It is possible that copper transport is hindered by the ability of the copper

chaperone for SOD1 (CCS) to effectively deliver copper to mutant SOD1, as the mutations studied here are important for the recognition of SOD1 by CCS. These results indicate that metals are unlikely to participate in the formation of aggregates, but copper dyshomeostasis is involved in the progression of ALS.

2.2 INTRODUCTION

Amyotrophic lateral sclerosis (ALS) is a neurodegenerative disease that affects 30,000 people annually in the United States, making it the most common motor neuron disease [2]. ALS begins with muscle weakness that develops into progressive paralysis and eventually leads to death, which generally occurs within two to five years of the disease diagnosis. There is currently no known cure for the disease and there are very limited treatments available, but they do not significantly alter the course of the disease [114]. Approximately 90% of all ALS cases are sporadic in nature with no known cause. The remaining 10% have a genetic link and are known as familial ALS cases. One such form of familial ALS is caused by a mutation in the gene that codes for the antioxidant protein copper-zinc superoxide dismutase that accounts for 2.5% of all ALS cases.

SOD1 is a metalloenzyme that binds one copper ion and one zinc ion per monomer for the protein's activity and stability, respectively [115]. There are over 160 known mutations in SOD1 that can cause ALS [30, 31]. These mutations are distributed throughout the protein and result in SOD1 mutations with dramatically varied biochemical properties, such as metal binding affinity and antioxidant activity. Thus, mutations are classified into two distinct categories: metal binding region (MBR) mutations, which directly affect the protein's ability to bind metal causing diminished activity levels; and wild type-like (WTL) mutations, which maintain metal binding

ability and have activity level similar to that of the wild-type (WT) protein [33, 34]. In this study, four SOD1 mutations were evaluated, including WTL mutations (A4V and G37R) and MBR mutations (H80R and D125H). The A4V mutation occurs at the SOD1 dimer interface and has very low stability [33, 116], while the G37R mutation is in an electrostatic loop and has much higher stability [117]. The H80R mutation is found in the zinc-binding region, hence zinc binding is diminished [118]. Since the ability of SOD1 to bind copper is thought to be dependent on its ability to bind zinc first, this mutation is also deficient in copper. The D125H mutation occurs in a charged loop that helps coordinate the metal binding site [33]. While it does not directly affect a metal-binding ligand, this mutation severely diminishes metal binding affinity, resulting in a protein with low stability. Despite extensive research, it is currently not understood how such a large distribution of mutations and their properties can all result in the same disease.

Metals have been implicated in a number of neurodegenerative diseases including ALS [119-121]. When improperly regulated, metals such as copper and zinc can be highly toxic to the cells. Copper is especially dangerous due to its catalytic activity and redox potential, resulting in the production of damaging reactive oxygen species (ROS), which lead to the propagation of oxidative stress found in patients with ALS [2, 122]. Alterations in zinc concentrations can also cause problems such as glutamate excitotoxicity, in which excess zinc over stimulates neurons resulting in cell death [69]. Interestingly, the only approved drug for the treatment of ALS reduces excitotoxicity by inhibiting glutamate release. Thus, proper metal homeostasis is critical to maintaining a healthy cellular environment and delaying disease progression.

Aggregates of misfolded SOD1 are found in the spinal cord motor neurons of patients with SOD1-ALS. Protein aggregates are found in several other neurological diseases, such as the amyloid-β plaques found in Alzheimer's disease (AD) and Lewy bodies composed of α-

synuclein in Parkinson's disease (PD). The role of these aggregates in disease has been the subject of great debate for a number of years. Originally, aggregates were thought to be the source of toxicity in these diseases. However, it is now generally accepted that aggregates are a cellular response to sequester toxic soluble proteins, avoiding further damage from the misfolded and aberrant proteins [58]. Unfortunately, the mechanisms of aggregation are not well understood. It has been observed that metals can aid in the precipitation and aggregation of amyloid-β [123] and α-synuclein [124]. Thus, metals are thought to play a significant role in protein aggregation. It was recently shown that the SOD1 aggregates found in a mouse model of SOD1-ALS are composed of unmodified and nascent SOD1 [60]. Nascent and unmetallated SOD1 mutants are relatively unstable compared to nascent WT SOD1, suggesting that mutants are more prone to aggregation than WT SOD1 [34, 125].

To study the metal content of SOD1 aggregates and cells overexpressing SOD-1 mutations we have employed the use of X-ray fluorescence microscopy (XFM), which is an invaluable non-destructive tool to investigate the localization of metals in biological specimens. XFM utilizes micro-focused X-ray photons to eject a core shell electron from the atoms in a specimen. This process results in the emission of a photon with an energy characteristic to that of the element it came from and allowing for the simultaneous collection of atomic elements within the specimen. Traditional metal quantification techniques, such as inductively coupled plasma-mass spectrometry (ICP-MS), are highly sensitive but lack the ability to determine the localization of metal ions within a specimen. More recently, laser ablation ICP-MS has been developed that possesses the ability to image a sample, but it has relatively low spatial resolution and is destructive to the specimen.

In this study, we investigated the role of metal ions in metal homeostasis and in aggregates using XFM in Chinese hamster ovary cells overexpressing WT SOD1 or mutant SOD1 (A4V, G37R, H80R, and D125H). To localize the transfected cells and the aggregates, SOD1 was coexpressed with yellow fluorescent protein (YFP) to provide a visual marker without the need for staining, which can alter the localization of loosely bound metal ions such as calcium. We investigated the relationship between metal content in the transfected cells and their aggregates between the WTL and MBR mutations relative to WT expressing SOD1 and untransfected controls. It was hypothesized that WTL mutations would contain similar metal ion concentrations to that of the WT overexpressing cells, as these mutations are capable of binding metals. Whereas the MBR mutations would show reduced metal concentrations due to their inability to bind copper or zinc. Intracellular SOD1 aggregates were hypothesized to be relatively unmetallated compared to their surrounding cytosol, as recent evidence suggests that aggregates are composed of nascent inactivated SOD1 [60].

2.3 Materials and Methods

Chinese hamster ovary cells (CHO-K1) (ATCC, Manassas, VA) were maintained in F12-K media with 10% fetal bovine serum, 1% penicillin/streptomycin, and 1% amphotericin-β. The cells were stored in an incubator at 37 °C and 5% CO_2. Cells were seeded onto silicon nitride windows (Silson, UK), an IR and X-ray transparent material, with a 500 nm membrane thickness. After 20 hours, when the cells were approximately 80% confluent, they were transfected with plasmid cDNA [126] using lipoD293 transfection reagent (SignaGen, Rockville, MD). CHO-K1 cells were transfected to express a WT or mutant (A4V, G37R, H80R, or D125H) form of SOD1 coexpressed with a YFP tag to visualize the transfected cells and

aggregates without staining. To transfect the cells, the same splitting and trypsinization procedure is followed, as detailed in section 1.9.5. However, instead of 2.5 mL of resuspended cells added to the new dish, 0.5 mL of resuspended cells was added to each of six 3 mL wells in a 6-well plate. Two silicon nitride windows were placed inside each well, measuring 2.5 mm x 2.5 mm with 500 nm thick membrane that were sterilized by dipping in 80% ethanol and air drying in a sterile HEPA-filtered cell culture hood. Once the cells have been added to the well, an additional 2 mL of media is added to each well for a total volume of 2.5 mL of medium. With 0.5 mL of cells there are a sufficient number of cells of which many will attach to the silicon nitride windows. The cells are allowed to sit overnight and attach to the dish and windows. After being seeded onto the silicon nitride windows, the cells were transfected at approximately 90% confluence, using Lipo-D293 transfection reagent (Signa-Gen Laboratories, Rockville, MD), which permeablizes the lipid membranes of the cells allowing the DNA plasmid to enter the nucleus. The lab of Prof. David Borchelt generously donated the DNA plasmids. Each plasmid contained SOD1 (WT, A4V, G37R, H80R or D125H) co-expressed with yellow fluorescent protein (YFP). The transfection procedure is as follows: medium was removed from each well in the 6-well plate and replaced with 1 mL fresh complete medium. Three μL of lipo-D293 transfection reagent were added to 50 μL of medium without FBS in an Eppendorf tube. In a separate Eppendorf tube, 1 μg of DNA plasmid was added to 50 μL of medium, also without FBS. Each tube was quickly vortexed and spun down for three seconds, allowing the solution to collect at the bottom of the tube. The transfection reagent solution was immediately added to the DNA plasmid solution, vortexed and spun-down for three seconds again to mix and collect the solution, which was then incubated for 15 minutes at room temperature. After incubation, the DNA/transfection reagent mixture was added to one of the wells in the 6-well plate with a

micropipette, and the cells were then returned to the incubator. Cells were monitored beginning 18 hours after transfection began, and the transfections were stopped when the majority of the cells were expressing YFP and punctate aggregates could be seen, between 19 and 26 hours [35]. The time to completion varied so that the aggregate levels would be equivalent for each mutation used. To end the transfection the silicon nitride windows were rinsed in PBS and dipped in cold (~80 °C) methanol three times for one second each time. The windows were allowed to dry at room temperature and were stored in a desiccator until imaged. Each transfection was carried out twice, and cells from both transfections were imaged.

FTIR point spectra were then taken on and off the aggregates to determine the protein density in the aggregates. These data were acquired with 4 cm^{-1} spectral resolution over the mid-infrared (IR) region (4000 – 800 cm^{-1}) on a Thermo-Nicolet Continuum using a synchrotron source at beamline U2B in the National Synchrotron Light Source (NSLS) at Brookhaven National Laboratory (Upton, NY). A 7 by 7μm spot size was used with a 32x IR Schwarzchild objective. Between 40 and 45 spectra were collected on the aggregates and off the aggregates of transfected cells, which were used to normalize the additional protein density found in the protein aggregates compared to the rest of the cell. To do this, the Amide I band was integrated from 1610 – 1700 cm^{-1} with a linear baseline from 1480 to 1800 cm^{-1} for spectra both on and off the aggregate and a ratio of the integrated values on to off the aggregate were calculated.

The cells were then imaged at the XFM beamline 2-ID-E at the Advanced Photon Source at Argonne National Laboratory (Argonne, IL) to determine the localization and concentration of metal ions. The incident beam was tuned to 10 keV using a Si(111) monochromator, and the X-rays were focused to 0.5 x 0.5 μm spot size with 20 cm zone plates (Xradia, Pleasanton, CA). The specimen was positioned at a 45° angle with respect to the incident beam and maintained in

a helium-purged box. The X-ray fluorescence was detected with a four element silicon drift detector oriented at 90° with respect to the incident beam and a differential phase contrast detector was used for the transmitted X-ray beam. Approximately 15 cells were imaged in each group with a 0.5-second dwell time per point. A full energy dispersive spectrum was collected at each point. Metal concentrations were determined based on NIST thin film standards 1832 and 1833. To analyze the data, three regions of interest (ROI) were generated around the nucleus, the cytoplasm (excluding the nucleus), and the aggregates (if present) using the MAPS program. The nucleus was analyzed as a separate ROI to provide a more accurate measure of metal concentrations in the cell body where the SOD1 is located. The data points within the ROI were then averaged. The aggregates were readily located using the phase contrast images collected with the XFM data. Statistics were performed on mean values from the ROIs with SPSS software (version 14.0) using the Kruskal-Wallis non-parametric test. Significant groups were then tested with Mann-Whitney U post hoc test. Significance was determined by $p < 0.05$.

2.4 RESULTS

This study measured the metal concentration in cells transfected with SOD1 (WT, A4V, G37R, H80R or D125H) coexpressed with YFP to visualize the transfected cells and SOD1 aggregates. **Figure 2.1** shows representative images of the cells from each group with YFP epifluorescence microscopy images and accompanying iron, copper, and zinc XFM maps. In **Figure 2.2**, XFM data were quantified from images, such as those shown in **Figure 2.1**, to obtain total copper concentrations from transfected with SOD1-YFP and untransfected cells. Copper concentrations were significantly higher in WT SOD1 expressing cells compared to untransfected and all mutant SOD1 cells (A4V, G37R, H80R and D125H). The mutant SOD1

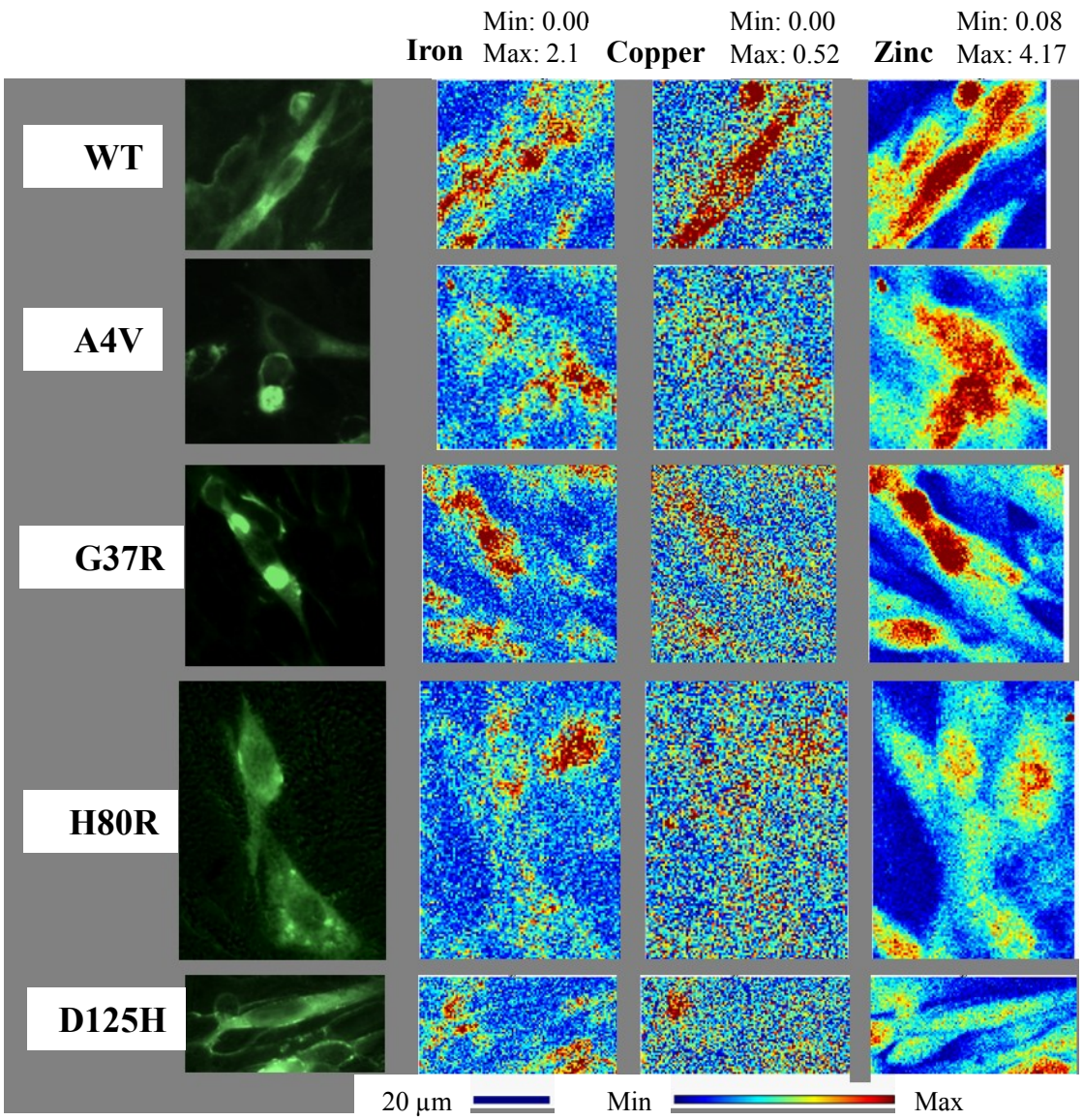

Figure 2.1. Epifluorescence images from SOD-YFP CHO-K1 cells (left column) with WT, A4V, G37R, H80R or D125H SOD. XFM maps shown for iron, copper and zinc in the second, third and fourth columns, respectively. These images show the relatively large amounts of copper and zinc found in the WT cells compared to the mutant SOD cells. Minimum and maximum concentrations are in mM.

overexpressing cells also contained a smaller but significant ($p > 0.05$) increase in copper compared to the untransfected cells. No quantifiable differences were observed between the mutant SOD1 cells, regardless of metal binding ability. However, the WTL mutations, especially

G37R, were expected to bind copper with similar affinity to that of the WT SOD1, based on activity levels in previous *in vitro* studies [117], but this did not occur in these cells.

For the aggregates, there was a two-fold increase in protein density, based on the FTIRM data. Thus, the XFM data for the protein aggregates were normalized by this factor. The aggregates were small 1-3 um, the 500 nm beam size allowed for several pixels (approximately 10) from each aggregate to be analyzed. **Table 2.1** demonstrates the copper and zinc concentrations quantified from the XFM data for the ratio of mutant SOD1-YFP aggregates (A4V, G37R, and H80R) to the total intracellular metal ion concentrations. Aggregates of mutant SOD1-YFP did not contain elevated metal concentrations compared to the surrounding area. In fact, a decrease in copper and zinc concentrations was observed in the aggregates.

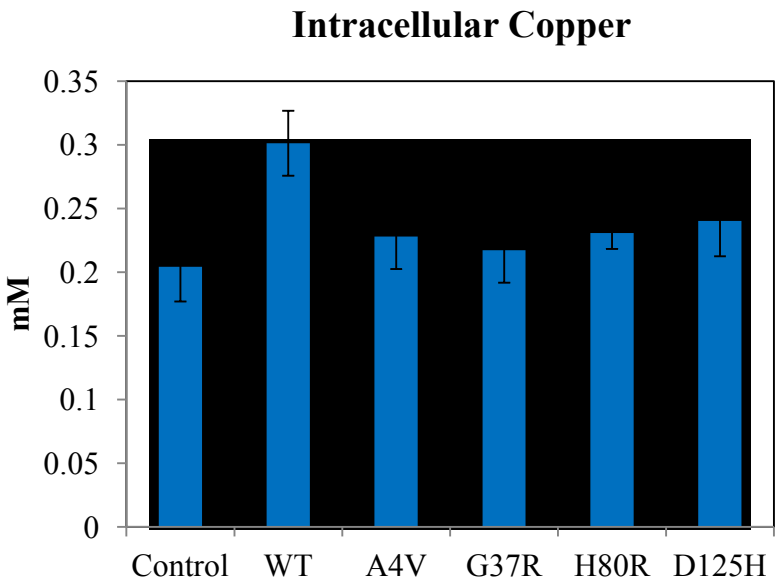

FIGURE 2.2 Bar graph of intracellular copper levels (excluding the nucleus) in mM. The WT cells contained the highest levels of copper in comparison to cells overexpressing mutations in SOD1 and untransfected control cells. All cells overexpressing mutant SOD1 had significantly higher copper content than the untransfected cells. * indicates significantly less than WT cells with $p < 0.001$.

No clear trends were observed in zinc concentrations between the untransfected and transfected cells. However, zinc is known to be involved in numerous cellular processes, such as DNA transcription and neuronal signaling, making its role more difficult to elucidate. Additionally, no differences were observed in the phosphorus, sulfur, potassium, calcium and iron concentrations (data not shown), nor were there any differences within the nucleus between the different cell types.

2.5 DISCUSSION

2.5.1 COPPER CONCENTRATIONS ARE LOWER IN CELLS OVEREXPRESSING SOD1 MUTATIONS

This study utilized two different types of SOD1 mutations, including WTL (A4V and G37R), which are known to bind copper and zinc and MBR (H80R and D125H), which are unable to bind copper or zinc [16, 34, 125]. Our results showed that all mutations contained similar copper concentrations, regardless of metal binding ability, and approximately 24% less copper than the WT cells. This suggests that all the mutations may suffer a serious disruption in copper homeostasis. The increase in copper concentration in the WT SOD1 cells compared to mutant SOD1 cells also demonstrates that there is in fact enough copper available to the cells to metallate at least part of the expressed SOD1.

In previous *in vitro* studies, WTL mutations were able to bind copper with the same affinity as WT SOD1, but MBR mutations showed reduced copper binding [33]. However, these *in vitro* experiments do not provide a representation of how SOD1 acquires copper within the cell. In the case of SOD1, copper is transported to the protein by the copper chaperone for SOD1 (CCS). CCS contains an SOD1 binding domain that has approximately 50% homology to SOD1

[127]. This homologous region in CCS is important for the recognition and binding of SOD1. All four mutations tested in our study have residues that reside in the binding domain of CCS, which may prevent the binding of CCS to SOD1 and, thus, alter the transport of copper. However, it should be further noted that in most eukaryotes an alternative CCS independent pathway also exists for delivering copper to SOD1, but it remains poorly understood [128].

These results are also in contrast to our metal studies of SOD1-ALS mouse models that found copper levels in the gray matter of the spinal cord and in soluble SOD1 were dependent on the ability of the mutation to bind metal discussed in **Chapter 3** [129]. Therefore, the WTL mutations contained increased copper similar to WT, but the MBR mutations did not show an increase. It is very possible that the levels of soluble SOD1 are increased in the mouse model compared to the cell model because the cells produce more dense insoluble aggregates than the mouse model. Another possibility is that the mouse tissues consist of a more complex network of different cell types. Recent studies have shown the importance of other cells, such as astrocytes, in the disease [130, 131]. The elevated copper could be localized in these other cells and not necessarily in the motor neurons, as the spatial resolution in that experiment did not allow for the differentiation between the cell types within the gray matter. Thus, it is possible that these other cells contribute to the maintenance of metal homeostasis and are affecting the copper concentrations in the tissues.

Copper is a vital component in cellular processes; and, due to its potential redox activity, it can be highly toxic when not properly controlled. As a result, copper transporters and chaperone proteins tightly regulate the concentration of copper in the cell. Maintaining a strict copper balance is critical and a disruption in homeostasis is implicated in several diseases, including ALS [132]. The results presented here suggest that cells with mutant SOD1 have a

disruption in copper homeostasis compared to the "healthy" WT SOD1 cells. However, the copper levels in the mutant SOD1 cells were elevated compared to the untransfected cells ($p > 0.05$). Our studies have further identified the localization of copper to the cell body of cytosol in WT SOD1 cells and further implicated that a disruption in copper homeostasis is correlated to the diseased state.

2.5.2 AGGREGATES DO NOT CONTAIN ELEVATED METAL

The formation of SOD1 aggregates in the spinal cord is the primary pathology found in ALS patients with SOD1 mutations, but little is known about the aggregation process. Cells transfected with mutant SOD1 developed intracellular aggregates, similar to those found in ALS patients. The aggregates in the transfected cells did not contain elevated metal. This was true regardless of the mutation's ability to bind copper (WTL and MBR). These data corroborate the hypothesis that SOD1 aggregates contain primarily immature SOD1 that was never properly folded or metallated. This hypothesis was largely based on the high stability of many holo-SOD1 mutations [36] and the lack of post-translational modifications on the SOD1 found in the aggregates [60]. Thus, if the aggregates develop before being metallated then they should not contain copper or zinc from the SOD1. These data also agree with a previous study that showed insoluble or aggregated SOD1 extracted from ALS mouse spinal cords contained no metal [129].

Protein aggregates found in other neurodegenerative diseases, including amyloid-β plaques and Lewy bodies from Alzheimer's disease (AD) and Parkinson's disease, respectively, have frequently been correlated with increased metal ion concentrations (iron, copper or zinc) [83, 133, 134]. In contrast, our study of aggregates in ALS shows that the aggregates were not enriched with metal, and the copper levels were diminished in the cells transfected with mutant

SOD1, implying that metals are not directly involved in the aggregation process. However, our study is limited to the analysis of a cell culture model of ALS, rather than in a mouse model or human ALS samples, as done in previous aggregate studies in other diseases. For example, Alzheimer's disease plaques, which consist primarily of aggregated amyloid-β protein and form in the brain of human patients, were found to be highly enriched in metal (calcium, iron, copper and zinc) compared to the surrounding brain tissue [83]. However, in a mouse model of Alzheimer's disease, it was found that the plaques did not contain elevated metal ions. This has led to the hypothesis that Alzheimer's disease plaques may accumulate metal over time. Thus, the mouse plaques, which are a few months old, contained less metal than the surrounding tissue; but the human plaques, which are many years old, have acquired a significant amount of metal over time. With respect to ALS, it is possible that there is a similar dependency to age of patient and subsequent evolution of the disease.

TABLE 2.1 The ratio of copper and zinc concentrations inside the aggregate to the total metal values in the cytoplasm of cells overexpressing A4V, G37R, and H80R. The aggregate content was normalized to the total protein content inside the aggregate to account for the increased density. The aggregates contained approximately two-fold more protein than the normal cellular area. Aggregates from all mutations contained less copper and zinc compared to the cytoplasm.

Mutation	Type	Copper	Zinc
A4V	WTL	0.53 ± 0.13	0.34 ± 0.21
G37R	WTL	0.45 ± 0.081	0.59 ± 0.27
H80R	MBR	0.41 ± 0.041	0.31 ± 0.14

The precise mechanism of aggregate formation is critical in order to gain an understanding of how aggregates impact disease progression. Recent *in vitro* studies have shown that nascent and unmetallated SOD1 accumulates in aggregates suggesting that much of the SOD1 is aggregated before becoming an active enzyme [60, 129]. This suggests a cytoprotective

mechanism for aggregate formation, as the aggregates prevent nascent SOD1 from activation and potentially damaging the cell. Further studies are also needed to understand the significance between unmetallated aggregates and copper dyshomeostasis seen in these ALS cells, and to determine if the mechanism of protein aggregation and the role of metals is similar to other neurological diseases (AD and PD) or unique to ALS.

2.6 CONCLUSION

Both metal homeostasis and aggregate formation have been implicated in the disease progression of ALS. Our study is the first instance where the metal content in the protein aggregates in ALS have been studied using microspectroscopy. We have investigated the vital components related to ALS and the distribution of metals in cells and aggregates in a systematic manner within the cellular environment. We observed a decrease in copper concentrations in the cells transfected with mutant SOD1 compared to WT SOD1, and unmetallated aggregates in the cells containing mutant SOD1. Our results indicate that there could be a relationship between the unmetallated aggregates and the reduced copper found in the cells overexpressing SOD1 mutations. It is possible that copper transport is affected, limiting the total cellular copper concentrations, and that CCS is unable to deliver copper to the mutant protein, which results in the rapid aggregation of the unstable apo-SOD1 contributing to the reduced copper in the cells.

CHAPTER 3

SPINAL CORDS FROM ALS MICE WITH MUTANT SOD1 ENRICHED WITH ZINC IN THE WHITE MATTER OF ALL MUTANTS AND COPPER IN THE GRAY MATTER OF WILD-TYPE LIKE MUTANTS

3.1 ABSTRACT

Metals are thought to play an important role in the progression of amyotrophic lateral sclerosis (ALS) and are a vital component of copper-zinc superoxide dismutase (SOD1), a metalloenzyme that causes ALS when mutations occur. However, the changes in metallation levels in ALS and the metallation status of soluble SOD1 *in vivo* have not been well characterized. Thus, the metal concentration and the metallation state of SOD1 in the spinal cords of transgenic ALS mice that overexpress a mutation in human SOD1 (G37R, H46R/H48Q, G93A or L126Z) were investigated. We have used X-ray fluorescence microscopy (XFM) to image the localization of metal ions and inductively coupled plasma mass spectrometry (ICP-MS) to determine the total metal concentrations of spinal cords, livers, and brains as well as the metallation status of SOD1 extracted from ALS mice (NTG, WT, G37R, H46R/H48Q, and G93A). While the total zinc concentrations did not change, a disease dependent shift in zinc from the gray matter to the white matter was found, which could be associated with glutamate excitotoicity. In addition, copper and iron were elevated in the gray matter of WT, G37R, G93A, and L126Z spinal cords, which are all capable of binding copper but not elevated in H46R/H48Q, as these mutations preclude the binding of copper. It was also found that soluble

forms of SOD1 were highly metallated in the WT, G37R and G93A mice. This indicates that mutations in SOD1 can be metallated *in vivo,* and it is likely that the increased copper in the gray matter can be attributed to the overexpression of SOD1, where the protein is also highly expressed. These data demonstrate a change in metal homeostasis that could have larger implications to the disease pathology of ALS.

3.2 INTRODUCTION

Amyotrophic lateral sclerosis (ALS) is a progressive neurodegenerative disease that affects the motor neurons of the spinal cord. The majority (90%) of ALS cases are sporadic and have no known cause. The remaining 10% of ALS cases are linked to a genetic mutation, such as those associated with the antioxidant protein copper-zinc superoxide dismutase (SOD1). In patients with mutations in SOD1, aggregates of the mutant protein form in the motor neurons of the spinal cord, and SOD1 is thought to become a pro-oxidant that contributes to the development ALS [43]. However, the mechanism of how SOD1 mutations cause ALS is not understood.

SOD1 is a metalloenzyme that binds one zinc ion, which imparts the protein's stability, and one copper ion for its catalytic activity converting superoxide into molecular oxygen. SOD1 is ubiquitously expressed but is more highly expressed in the central nervous system (CNS) and in the liver, where metabolic processes are generally higher requiring increased antioxidant activity. Interestingly, mutations in SOD1 exclusively affect the motor neurons of the spinal cord, leaving the rest of the CNS and liver undamaged. There are over 160 known mutations in SOD1 that can cause ALS, and these mutations are classified as either wild type like (WTL) or metal binding region (MBR) mutations [30, 31]. WTL mutations maintain similar activity and

metal binding capabilities to that of the unmutated wild-type (WT) protein. In contrast, MBR mutations affect the metal binding sites of SOD1, reducing its affinity for copper and/or zinc, and therefore limiting the activity levels [16]. Despite these dramatic differences in properties, both types of mutations are capable of causing ALS.

Due to the presence of copper and zinc in SOD1, metal ions are thought to play an important role in ALS. Copper is a biologically redox active metal that is capable of inducing oxidative stress and increasing the production of damaging reactive oxygen species (ROS). Hence, copper is tightly regulated within the cell. Zinc is not redox active but is toxic at both high and low concentrations, thus a proper balance of zinc is also essential to maintain a healthy cellular environment [69]. If the metal homeostasis of copper and/or zinc is altered, it could have a dramatic effect on the progression of ALS, and could direct treatment options towards reestablishing a proper homeostasis of metal ions.

This study is aimed at understanding the metallation levels in the spinal cords of transgenic mice that overexpress human SOD1 mutations, including WTL mutations: G37R, G93A, and L126Z and the MBR mutation, H46R/H48Q. The localization of metals in the spinal cord was determined using X-ray fluorescence microscopy (XFM) on cross sections of the mouse spinal cords. Metallation levels of spinal cord, brain and liver tissue from the same mice were measured using ICP-MS. Additionally, the metallation status of soluble SOD1 extracted from the tissues was studied using HPLC-ICP-MS. It was hypothesized that metal concentrations and SOD1 metallation status from the tissue specimens would be influenced by mutation type, where specimens with WTL mutations would contain similar metal content to that of the WT specimens and the MBR mutations would show reduced metallation levels.

3.3 MATERIALS AND METHODS

3.3.1 XFM

For XFM, end-stage mutant (G37R, H46R/H48Q, G93A, and L126Z hSOD1) and age-matched control mice (WT and NTG) (n = 4 for all groups) were euthanized and perfused with trace metal-free 4% paraformaldehyde in phosphate buffered saline (PBS) to remove blood from the vasculature [105]. Spinal cords were fixed and stored in 4% paraformaldehyde, and soaked overnight in 20% sucrose for improved sectioning. After soaking in the sucrose, the spinal cords were rapidly frozen over liquid nitrogen and embedded in the optimal cutting temperature OCT compound. One thin section was cryotomed to 20 μm thick from each mouse and carefully deposited on a 0.5 μm-thick silicon nitride window (Silson, UK) for FTIR imaging (FTIRI) and XFM. Specimens were allowed to dry on the window and kept in a desiccator until measurements were taken. In order to distinguish the white versus gray matter without staining, FTIRI was employed. FTIR images were collected using a Perkin Elmer Spectrum Spotlight infrared microscope in the mid-infrared region (4000-800 cm^{-1}) using a 6.25 μm pixel size, 8 cm^{-1} spectral resolution, and 8 scans co-added per pixel. The white and gray matter were distinguished from the FTIR images using unsupervised principal components analysis (PCA) based on difference in lipid and protein composition between these anatomical regions. After FTIR imaging, the metal content in the same samples was imaged using XFM at beamline X27A at the National Synchrotron Light Source (NSLS) at Brookhaven National Laboratory (BNL). X-ray fluorescence spectra were collected using an X-ray excitation energy of 11 keV, a beam size of 9 μm (vertical) by 17 μm (horizontal), and 15 μm steps, with an integration time of 7 sec/pixel. Based on the symmetry of the spinal cords only one half containing a dorsal and

ventral horn was imaged. The intensity for each metal was quantified by integrating the area under the curve for the respective peak in the XFM spectrum (copper Kα = 8047.8 eV and zinc Kα = 8638.9 eV). NIST thin film standard reference materials 1832 and 1833 were used to calculate concentration and to normalize any differences between the multiple beamtime runs required to collect the data. The concentrations of zinc and copper in the standards were 3.75 $\mu g/cm^2$ and 2.52 $\mu g/cm^2$, respectively. To convert from $\mu m/cm^2$ to mM, the $\mu m/cm^2$ values were divided by the product of the volume of X-ray beam on the sample (area x thickness of the sample), the density of tissue (estimated to be 0.9 g/cm^3), and the molecular weight of the element.

Statistical analysis: The white and the gray matter in the spinal cord cross-sections were distinguished based on the PCA of the FTIR images. The FTIR PCA images were overlaid onto the iron, copper, and zinc XFM images and masks were generated for the white and gray matter. Additionally, outlier pixels were identified as those pixels with a value >100x the median value and were excluded. Median values were calculated for both the gray and white matter of the copper and zinc maps.

All statistics were performed using SPSS (version 14.0). To test for significance within the regions of interest (ROI) for the mutants, WT and NTG mice, the Kruskal-Wallis test was performed on the medians for each group. Groups that satisfied $p < 0.05$ were then subjected to post-hoc analysis using the Mann-Whitney U test to determine the significance within the groups. A significance level of $p < 0.05$ was also used for the Mann-Whitney U test.

3.3.2 ICP-MS Analysis of Whole Tissues

For ICP-MS analysis, mice were sacrificed and perfused in the same manner as the XFM mice [129]. Spinal cords, brains, and liver from mice were analyzed for metal content, including: 8 WT, 8 G37R, 6 H46R/H48Q, 8 G93A, and 7 NTG mice. Samples were cut, weighed (20-25 mg/sample), and digested in 25 μL of concentrated nitric acid for four hours at 95 °C. The digests were then diluted in 2 mL of 2% nitric acid, and the total metal concentrations were determined using an ICP- MS (Agilent 7500).

3.3.3 Isolation of soluble SOD1 and Metallation State

Spinal cord, brain or liver specimens were homogenized in chilled trace-metal free PBS using an ultrasonic disintegrator [129]. Homogenates were then centrifuged and the supernatants were loaded on to a gravity-flow G-75 size exclusion column to isolate SOD1 with about 75% purity. Metallation state of the soluble SOD1 was determined using high-pressure liquid chromatography (HPLC) ICP-MS. The HPLC (Agilent 1200) was used to separate out the contaminating species using the absorbance at 214 and 280 nm. The human SOD1 separated out at about 15 minutes, while the endogenous mouse SOD1 separated out at 16 minutes allowing for a clear separation between the two proteins. A minimum of three mice with at least three replicates from each mouse was used for each genotype. The exact metallation state was determined by dividing copper or zinc levels by the SOD1 concentration to yield the metal/dimer levels. The ICP-MS and HPLC-ICP-MS methods are described in further detail in Lelie, et al. [129].

3.4 RESULTS

Due to the tight regulation of intracellular metal ions, it was difficult to ascertain how the overexpression of SOD1 would affect metallation levels in mice. To determine the effects of SOD1 overexpression and/or the disease on metallation state, spinal cord tissues were imaged using XFM. These data were compared to ICP-MS data using mice with the same genotypes (except L126Z, which was only used in the XFM study). The metal concentrations of spinal cord, brain and liver, where SOD1 is highly expressed, were compared to determine if the tissues unaffected by the disease (brain and liver) contained similar metallation trends to that of the spinal cord. In addition, HPLC-ICP-MS was used to measure the metallation state of soluble SOD1 extracted from the tissue specimens.

3.4.1 METAL LOCALIZATION IN THE SPINAL CORD

In order to establish the location of the white matter, gray matter, dorsal horn, and ventral horn without staining, FTIRI was first performed on spinal cord cross-sections. Principal components analysis (PCA) based on the lipid region (2750-3025 cm^{-1}) and the amide I region (1600-1710 cm^{-1}) of the infrared spectrum revealed deep contrast between the white versus gray matter (**Figure 3.1**, top row). The white and gray areas reflect the white and gray matter respectively, the left gray matter lobe represents the ventral horn, while the right gray matter lobe represents the dorsal horn. Somatic motor nuclei cell bodies originate in the ventral horn of the gray matter and descend their tracks through the surrounding white matter. Some of these tracts are visible as streaks across the white matter in the FTIR images.

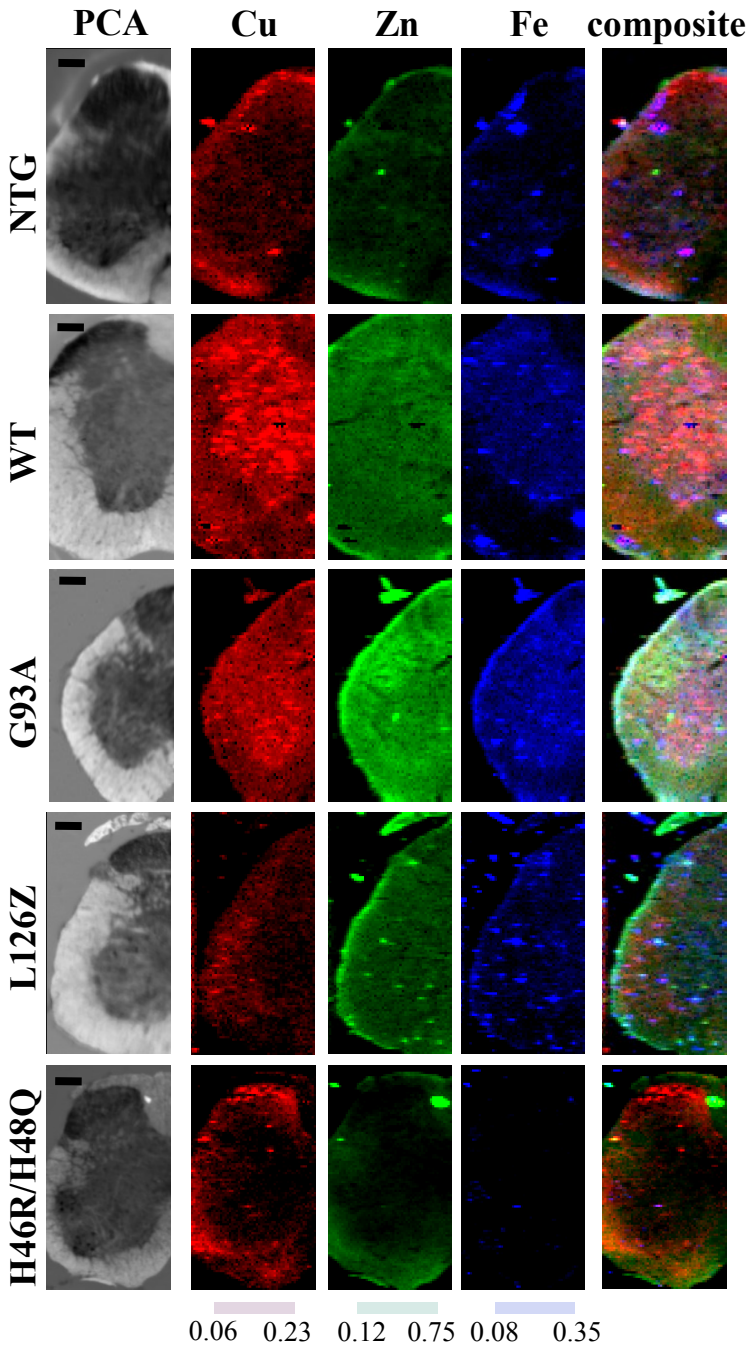

FIGURE 3.1 Infrared and X-ray fluorescence microscopy (XFM) images of half a spinal cord cross section from a normal mouse (non-transgenic), a healthy mouse expressing normal SOD (wild-type), and diseased ALS mice with SOD mutations G93A, L126Z, and H46R/H48Q (G37R not shown). The left row contains infrared PCA data showing the lipid-rich white matter around the protein-rich gray matter. The second, third, and fourth columns show the copper, zinc, and iron content from X-ray fluorescence microprobe X27A. Copper and iron were decreased in gray matter of the H46R/H48Q mutations, which does not bind copper. All of the spinal cords from the sick mice contain more zinc in the white matter compared to the healthy mice. The black scale bar represents 0.1 mm, and the XFM scale bars are in concentration units of mM (adapted from [129]).

Copper and zinc distribution were determined with XFM on the identical tissue sections (**Figure 3.1**, center and bottom rows, respectively). The different types of mutants showed uniquely distinct results. A trend was observed for zinc content which appeared higher for the mutants relative to the controls. In addition, zinc levels were consistently higher in the white matter compared to the gray matter for all samples analyzed. The major zinc trend did not reflect metallated SOD1 expression. Intriguingly, the diseased G37R, H46R/H48Q, G93A, and L126Z mice had statistically significant levels of elevated zinc relative to the control NTG mice in the white matter, possibly reflecting a phenomenon that may be associated more with disease than with over-expression (**Figure 3.1**). An increase in zinc concentrations associated with white matter has been previously detected by XFM on cerebellum tissue cross-sections. It was postulated that this increase may be due to the requirement of zinc for myelin synthesis, structure and maintenance [135]. Alternatively, the increase in zinc in the white matter could be attributed to glutamate excitotoxicity seen in ALS patients.

Upon comparison to the NTG animals, it was apparent that there were copper concentration increases within the gray matter for the WT, G37R, G93A, and L126Z transgenic mice, which overexpress SOD1 with a high ability to bind copper. Conversely, the H46R/H48Q, which have very low SOD1 copper metallation showed lower copper levels in the gray matter. Statistically significant increases in gray matter copper were observed between NTG versus G93A and WT mice (*) and between WT versus H46R/H48Q mice (**), confirming the observation described above (**Figure 3.2**). The expression of SOD1 is enhanced in the gray matter compared to the white matter [136], and this can explain why copper levels would be higher for transgenic mice that overexpress copper bound SOD1.

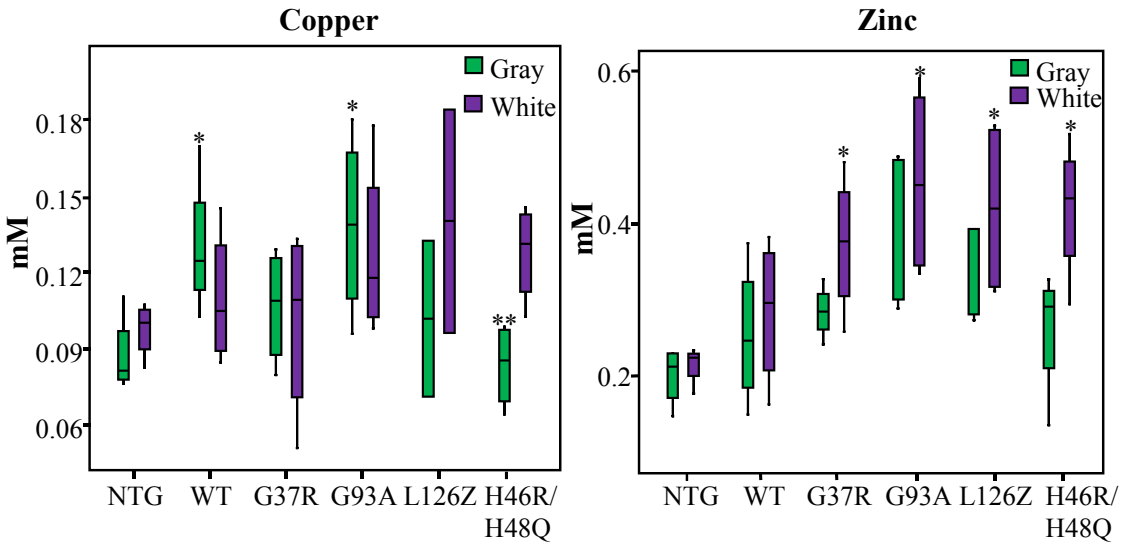

FIGURE 3.2 Box plots of median copper and zinc concentrations (mM) shown in the same cross-sections of spinal cord, as measured by XFM. All spinal cords from mice expressing mutant human SOD1 showed elevated zinc in the white matter compared with the NTG. In the gray matter, copper was elevated over NTG in WT, G37R and G93A but not the double mutant H46R/H48Q, which does not bind copper (*, significantly different from NTG; **, significantly different from WT by Kruskal-Wallis and Mann-Whitney U test). At least three cross-sections were analyzed from four mice of each genotype (adapted from [129]).

Iron concentrations in the spinal cords were well correlated with those of copper. Increased iron was found in the gray matter of the transgenic mice WT, G37R, G93A, and L126Z, but not in the double mutant, H46R/H48Q. These findings are similar to those found by previously in the G37R mouse [137]. The presence of iron in the WT mouse decreases the likelihood that this is related to ALS. However, SOD1 is a significant source of copper and zinc so it is not surprising that it may affect the localization of other metals such as iron.

3.4.2 METALLATION LEVELS IN SPINAL CORD, BRAIN, AND LIVER

ICP-MS analysis of whole spinal cords from mice of the same genotypes revealed no significant variation in the total copper or zinc concentrations, despite a 10-fold increase in SOD1 expression, as shown in **Figure 3.3**. The copper levels were very consistent, with the

lowest levels of 4 µg/g in the H46R/H48Q mice and 6 µg/g in the NTG mice, which had the highest copper levels. A larger amount of zinc than copper was found in the spinal cords, which is consistent with the higher abundance of zinc in biological samples. However, the zinc levels did correlate with the mutation type, where H46R/H48Q contained the lowest levels of zinc and WT and G93A contained the highest zinc concentrations. These data demonstrate the importance of spatially resolved techniques such as XFM to determine where changes in metal ion concentrations are occurring.

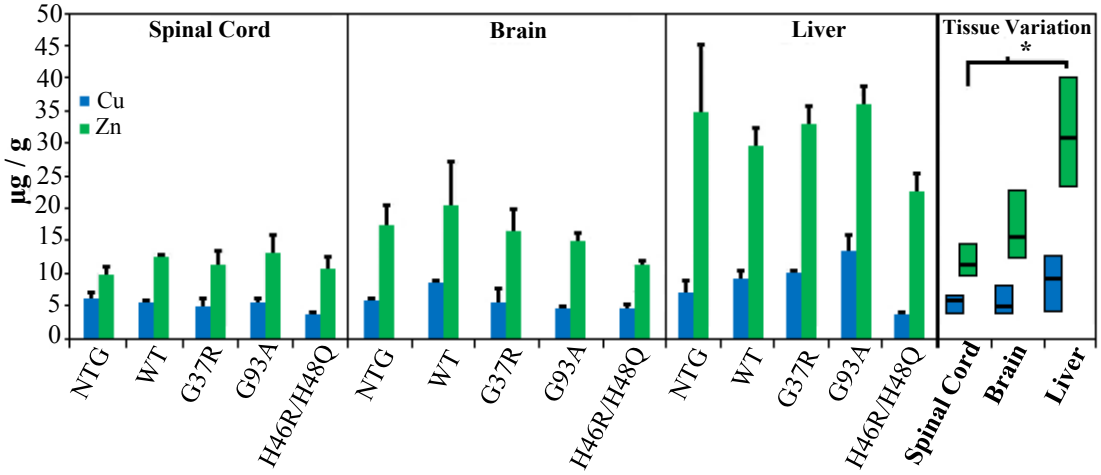

FIGURE 3.3 Selections of spinal cord, brain, and liver from a NTG and transgenic mice overexpressing human WT, G37R, G93A and H46R/H48Q SOD1 were weighed, completely digested in nitric acid, then subjected to metal quantification by ICP-MS. The H46R/H48Q mouse brain and liver zinc concentrations were consistently lower than all other mice (arrow, $p < 0.005$). Far right panel, a box plot graph incorporating all measurements from the same tissue demonstrated that copper concentrations remain relatively constant in the brain and spinal cord, whereas zinc was lower in the spinal cord, somewhat higher in the brain (p value 0.019), and highest in the liver (*, $p < 0.0001$ relative to spinal cord). The bar graph results are reported in mean µg of metal/g of tissue (wet weight), and error bars represent the S.D. of three or more independent mice per genotype (adapted from [129]).

The liver showed the highest levels of copper and zinc compared to the spinal cord and brain, which is likely due to liver's role in metal storage. The copper levels were significantly elevated in the liver of WT mice and mice with WTL mutations (G37R and G93A) compared to NTG and H46R/H48Q. However, there was no significant change in copper in the brains based on genotype. A significant decrease was seen in zinc concentration of the H46R/H48Q mutation

compared to all other mice in the liver and the brain. Interestingly, total metallation levels of spinal cords were the least affected by mouse genotype, whereas the brain and liver specimens showed some changes in copper and zinc levels.

3.4.3 METALLATION STATE OF SOLUBLE SOD1

The HPLC-ICP-MS measurements revealed that the soluble SOD1 from the spinal cord, brain, and liver was highly metallated in the WT and WTL mutations. However, the H46R/H48Q mutation contained copper and had significantly reduced zinc; but this mutation affects the metal binding region and has reduced copper and zinc affinity [138], which explain the change in metallation levels. The neuronal tissue (brain and spinal cord) contained approximately 1-1.25 copper/dimer of SOD1 and 2.6-3.2 zinc/dimer of SOD1 in the WT and WTL mutations. These levels are similar to those found when human SOD1 was over expressed in *Saccharomyces cerevisiae*, where copper varied between 0.5-1.5 copper per dimer and 2-3 zinc per dimer [139, 140]. Number of metal ions is nearly four ions per dimer, suggesting that each of the two metal binding sites per SOD1 monomer is metallated. Interestingly, human WT SOD1 had slightly but significantly lower zinc content than G37R and G93A SOD1. Also the endogenous mouse SOD1 from the NTG mice contained the most even copper to zinc ratio with two copper and two zinc ions per dimer. The metallation levels of the liver SOD1 showed similar trends to the metallation levels of the neuronal tissue but had reduced total metallation, specifically in zinc content. This suggests that the excess metallation of SOD1 with zinc is associated with the CNS tissue. **Figure 3.4** illustrates the total copper and zinc levels in the soluble SOD1 from the spinal cord, brain and liver tissues.

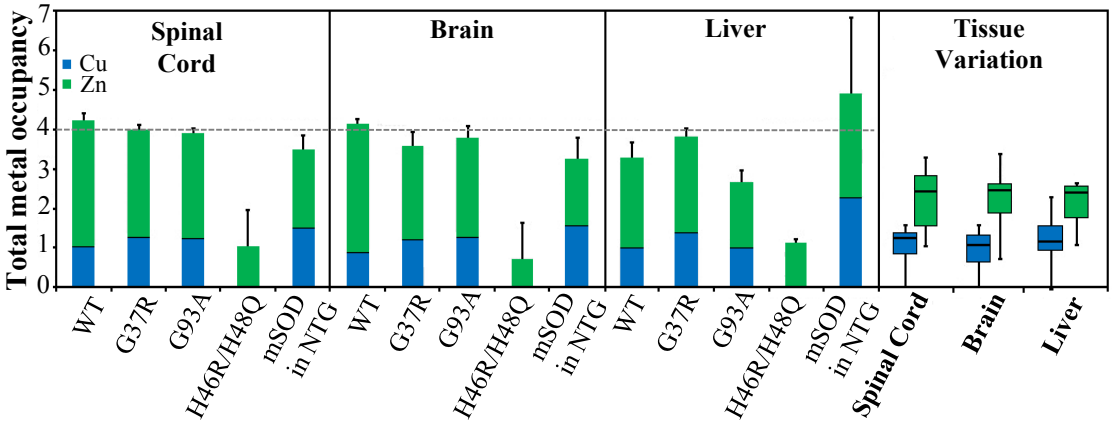

FIGURE 3.4 SOD1 metallation in various tissues from transgenic mice. A stacked bar graph representation of metallation to illustrate total metallation of SOD1. The dashed line at four metals/dimer delineates a fully occupied metal binding site. With the exception of the H46R/H48Q mutant, most other SOD1s are highly metallated. Left, shown is the box plot graph of combined metallation states for each tissue demonstrating disuse variability. Despite the vastly different trends among mutant metallation states, it is interesting to note that median copper and zinc values remain consistent across all tissues examined. All bars represent the mean S.D. of three of more independent mice per genotype. Box plots represent median values and 25th and 75th percentile ranges (adapted from [129]).

3.5 DISCUSSION

Copper and zinc play an important role in the function and structure of SOD1 and thus they are considered to play an important role in the disease pathology. A disease dependent shift in zinc concentration to the white matter in all SOD1 mutations demonstrates a change in zinc homeostasis associated with ALS. Most of the expected changes in copper and zinc concentrations were anticipated to be in the gray matter, where SOD1 is expressed in the cell bodies, but this was not observed for zinc. As a vital component in neurotransmission and many metalloproteins, proper regulation of zinc is of significant importance. The effects of elevated levels of zinc, found in ALS, could have a cascade of detrimental neuro-toxic consequences.

Glutamate excitotoxicity is a potential source of excess zinc in the white matter and one of the major pathological features of ALS [141]. Riluzole, the only currently available treatment for ALS patients, is a glutamate release inhibitor [69]. While generally considered neuroprotective, glutamate release can be over-stimulated in diseases such as ALS and become a potent neurotoxin. It is hypothesized that the release of glutamate is accompanied by a release of zinc, as the two are often colocalized and the presence of zinc can exacerbate glutamate release. The increase in zinc found in the white matter, which contain the axons and where neurotransmitters are released, could be linked to the glutamate excitotoxicty, seen in ALS.

The increase of zinc in the white matter is contrary to the findings of a preliminary study with human ALS specimens [142]. In this study, zinc was lower in the white matter than in the gray matter, and a marked increase in zinc was found in the neurons of the spinal cord compared to the surrounding tissue. Additionally, they did not observe a significant increase in white matter zinc in the ALS specimens compared to the control tissue. However, the study only contained three sporadic ALS cases, and only small regions of the spinal cords were mapped (20 x 20 μm) so it is possible that the regions mapped were not representative of the entire spinal cord.

Aside from SOD1, metallothionein is another zinc-binding protein that is affected in ALS patients, where it is elevated in the brain and liver [143, 144]. In G93A SOD1 mice increased labile zinc was found [145] and metallothionein was also increased in the astrocytes and neurons [146]. Interestingly, depletion of metallothionein in G93A SOD1 mice exacerbated the ALS phenotype [147, 148]. As a result, the expression of metallothionein is thought to be neuroprotective compensatory mechanism to handle excess zinc. The expression of metallothionein occurs primarily in the gray matter, where small but only statistically

insignificant increases in zinc were found. These results underscore the importance of zinc homeostasis in ALS.

The increase in copper and iron in the gray matter of WT and WTL mutations compared to NTG mice shows that an increase in copper and iron is likely a result of the overexpression of SOD1, as both metal ions can bind to the copper active site. The double mutant H46R/H48Q, which cannot effectively bind copper, did not show this increase. The lack of copper in the gray matter of the spinal cord of the H46R/H48Q, as well as in the soluble SOD1 of the double mutant, indicates that copper-bound SOD1 is not the cause of ALS. However, the total copper levels do not change significantly, which may be a result of an over burdened copper pathway. Additionally, copper levels in SOD1 were found to be lower than expected for a "normal" SOD1 dimer (two copper and two zinc ions). The soluble SOD1 from WT and WTL mutations contained more than two zinc ions per dimer and less than one copper ion for WT and WTL mutations. This indicates that there may not have been sufficient copper present to fully metallate all of the SOD1.

3.6 CONCLUSION

In summary, these data suggest that zinc homeostasis is disrupted in the spinal cords of ALS mice. This could be in part due to glutamate excitotoxicity, which can lead to excess zinc release from the axons in the white matter. Copper was elevated in the WT and WTL mutation mice as shown by an increase in the gray matter copper levels and in the copper bound to soluble SOD1. This is consistent with the overexpression of SOD1, which requires the presence of copper for its activity. In contrast, copper was not elevated in the MBR mutation, H46R/H48Q, which indicates that SOD1 bound copper is not likely to be a cause of ALS, suggesting that

copper concentrations are influenced by the ability of the mutation to bind metal. These results provided a unique insight into the role of metal ions specific to this disease.

CHAPTER 4

ALS MICE WITH THE G37R SOD1 MUTATION SHOW FEWER SIGNS OF OXIDATIVE STRESS THAN OTHER SOD1 MUTATIONS

4.1 ABSTRACT

There are over 160 known mutations in the gene that codes for copper-zinc superoxide dismutase (SOD1) that can cause a familial form of amyotrophic lateral sclerosis (ALS). These mutations vary greatly in biochemical and biophysical properties, such as metal binding ability, activity, and life expectancies in patients; but they all result in the same fatal disease. Oxidative stress is a major component of motor neuron death and the progression of ALS. In this study, the products of oxidative stress reactions were investigated in both proteins and lipids in transgenic mice overexpressing wild-type (WT) human SOD1, as well as four transgenic mice overexpressing mutations in human SOD1 (G37R, G93A, H46R/H48Q, and L126Z). Oxidative damage in the spinal cord was assessed by measuring protein carbonyls using densitometry measurements of SOD1 oxyblots and lipid unsaturation with Fourier-transform infrared microscopy (FTIRM) based on the olefinic peak (=CH stretch) at 3012 cm^{-1}. Our results showed elevated protein carbonyls and decreased levels of lipid unsaturation in the WT SOD1 mice compared to the NTG, indicating increased levels of oxidative damage. The G93A, H46R/H48Q, and L126Z mice contained similar levels to the WT. In contrast, the G37R mice contained significantly higher lipid unsaturation and lower protein carbonyls compared to other transgenic mice, suggesting reduced oxidative stress. The relatively unperturbed copper-binding site of G37R may lead to less aberrant redox chemistry compared to the other mutations. Additionally,

the G37R mutation also reduces the net negative charge of SOD1 making the mutant more prone to aggregation, which may reduce the amount of the soluble protein present in the cell. ALS patients with the G37R mutation live an average of 17 years, which is significantly longer than most patients with other SOD1 mutations, who live on average two to five years after diagnosis. It is possible that the reduced oxidative stress found in this mutation allows for the increased longevity of patients and suggests that a reduction in oxidative stress may increase the life expectancy of ALS patients.

4.2 INTRODUCTION

Amyotrophic lateral sclerosis (ALS) is a neurodegenerative disease; and, with a life time risk of 1 in 2000, ALS is the most common motor neuron disease [16]. It is characterized by muscle weakness, progressive paralysis and eventually death. While 90% of ALS cases are sporadic, with no known cause, the remaining cases have a genetic link. Approximately 25% of the genetic or familial ALS cases are caused by a mutation in the gene *SOD1*, which codes for the antioxidant protein copper-zinc superoxide dismutase (SOD1) [16]. SOD1 is a metalloprotein that binds one zinc atom for stability and one copper ion for its activity. The mutated SOD1 forms aggregates in the motor neurons of the spinal cord of ALS patients [2].

SOD1 is an abundant antioxidant protein and mutations may disrupt the protein's ability to function properly. There are over 160 known mutations that occur in SOD1, and only one of these mutations is required to cause SOD-related ALS (SOD1-ALS) [30, 31]. These mutations are scattered throughout the protein and possess a wide variety of properties, making it challenging to understanding how they all cause ALS. For example, wild-type like (WTL) mutations, such as G37R, G93A, and L126Z, are capable of binding copper and zinc and often

maintain similar activity levels to that of the wild-type (WT) protein. However, other mutations are in the metal-binding region (MBR), such as H46R and H48Q, which affect the protein's ability to bind copper and/or zinc. Without the copper ion the protein is unable to function effectively. Additionally, there is a wide range of average survival times for human patients with these mutations. On average, a patient will live two to five years after diagnosis [16]. However, patients with some mutations, such as G37R and H46R, are especially long lived, i.e. approximately 17-18 years after the onset of symptoms. It is currently unclear how the variety of biochemical properties of the SOD1 mutations can all lead to the same disease.

It has been hypothesized that the copper and zinc may not be properly bound to the protein or the protein may not be properly folded, resulting in improper exposure of the redox active copper (Cu^{+}/Cu^{2+}) to the surrounding environment, inducing the production of ROS and oxidative damage. For example, copper can be improperly incorporated into the zinc binding site of SOD1 [149] or the H46R mutant of SOD1, which contains a surface exposed cysteine residue capable of binding copper [65].

Oxidative damage is one characteristic of ALS that is seen in both the familial and sporadic versions of the disease [150-152]. It is caused by the production of reactive oxygen species (ROS) such as superoxide or hydrogen peroxide, which subsequently attack lipids and proteins inside the cell. These reactions result in detrimental cellular damage, such as weakened cell membranes, through lipid peroxidation and increased protein carbonylation to mark proteins for degradation. The effects of oxidative stress on proteins can be measured by the concentration of protein carbonyls. ROS are capable of oxidizing the side chains of amino acids, especially proline, lysine, arginine and threonine [153]. The products of these reactions are highly stable

and readily detected. Thus, levels of protein carbonyls have become widely used as a measure to detect oxidative stress reactions on proteins.

Oxidative damage to lipids can be determined using Fourier-transform infrared imaging (FTIRI) by measuring lipid unsaturation, which is directly associated with the intensity of the olefinic peak at 3012 cm^{-1} [86, 87]. FTIR measures the frequency of vibrational bonds, providing valuable chemical information. For example, lipids contain numerous C-H bonds (~3000 cm^{-1}). The adjacent bonds alter the precise frequency of the bond vibration. Thus, unsaturated lipids, which contain C=C-H, appear at 3012 cm^{-1}. Unsaturated lipids are especially prone to oxidative stress, which reduces the double bond to a single bond, resulting in increased saturated lipids. Therefore, a smaller olefinic peak is correlated with a decrease in unsaturation and an increase in the degree of oxidative damage.

In this study, lipid unsaturation and protein carbonyl levels were examined in the spinal cords of mouse models of the SOD1-ALS. WT, G37R, G93A, H46R/H48Q (an unnatural double mutation), and L126Z mutants were compared to NTG animals to determine the degree of oxidative damage. These results were then correlated with the known biochemical properties of each mutant.

4.3 Materials and Methods

4.3.1 Animals

All animal experiments were approved by the University of Florida Institutional Animal Care and Use Committee. Five transgenic mouse lines were used: G37R [line 29] [41], G93A [B6SJL-TgN (SOD1-G93A)1Gur; The Jackson Laboratory] [104], H46R/H48Q [line 139] [105], L126Z,

and WT [line 76] [41], as well as a nontransgenic (NTG) control (n = 4 for each mouse type). On average, mice were seven months old when sacrificed; and the G37R, G93A, H46R/H48Q, and L126Z mice were at the end stage of motor neuron degeneration. The animals were anesthetized, perfused and fixed with 4% paraformaldehyde in phosphate buffered saline (PBS), which is described in further detail by Wang et al. [105]. The spinal cord tissues used for imaging experiments were soaked overnight in 20% sucrose for improved sectioning.

4.3.2 Protein Carbonyl Detection with Oxyblot

Soluble extract isolated from mouse spinal cords were run on standard SDS-PAGE [154]. The procedure from the Chemicon OxyBlot kit (Milipore) manual was followed. Briefly, the gel was transferred to a PVDF membrane and immediately derivatized after the western transfer. This involved rinsing the membrane with methanol and 2 Normal hydrochloric acid, followed by incubation on a rotary shaker for exactly five minutes with 2,4-dinitrophenylhydrazine (DNPH) to derivatize protein carbonyl groups in the protein side chains, converting them to 2,4-dinitrophenylhydrazone (DNP-hydrazone). The membrane was then washed three additional times with 2 Normal hydrochloric acid and five times with 100 % methanol for five minutes each and then blocked for 30 minutes in a blocking solution (PBS, 5 % non-fat dry milk w/v, 1% TWEEN-20 v/v). The blocking solution was replaced and the membrane was blotted for two hours with a primary antibody against the DNP moieties. The membrane was washed five times for five minutes each in blocking solution and then incubated with a rabbit secondary conjugated to alkaline phosphatase (Sigma-Aldrich) for one hour. The blot was washed as previously described and then transferred from blocking solution to an alkaline phosphatase buffer (0.1M NaCl, 3mM $MgCl_2$, 0.1 M TRIS, pH 9.5) and washed three times with alkaline phosphatase

buffer. The western blot was visualized with a solution containing nitrotetrazolium blue and 5-bromo-4-chloro-3 indolyl phosphate. A simultaneous western was run probing for SOD1 to determine its migration on the oxyblot western. Densitometry was then used to determine the band intensity of SOD1 protein carbonyls from the oxyblot and SOD1 levels from the SOD1 blot. The dennsitometric signal of oxyblot SOD1 was divided by SOD1 blot to render a relative value of protein carbonyl level per SOD1 levels.

4.3.3 Sample Preparation for FTIRI

The spinal cords were soaked in 20% sucrose overnight and frozen over liquid nitrogen vapor. The frozen tissues were then embedded into the optimal cutting temperature (OCT) compound for cryosectioning. Specimens were cryosectioned into 10 µm sections, carefully placed on to 1 mm thick calcium fluoride slides (Korth Kristalle GMBH, Kiel, Germany), allowed to dry at room temperature, and stored in a dessicator until imaged.

4.3.4 FTIRI Data Collection

All FTIRI data were collected using a Bruker Vertex 80V infrared spectrometer and Hyperion 3000 infrared microscope. The microscope was equipped with a liquid nitrogen-cooled, 64 x 64 pixel focal plane array (FPA) detector with a pixel size of 10.9 microns (15x objective and 4x4 binning) and 128 scans per pixel. A spectral range from 850 to 3900 cm^{-1} and a spectral resolution of 8 cm^{-1} were used. Background spectra were taken from a clean area of the calcium fluoride slide (256 scans, 8 cm^{-1} resolution). Due to the symmetry of the spinal cord, one half (including a dorsal and a ventral horn) of the spinal cord was imaged from each section. Each tissue section was imaged over an area approximately 1 mm by 1.5 mm and contained

approximately 10,000 pixels per map. Four spinal cord sections, one from each mouse, were imaged from each of the six groups, NTG, WT, G37R, G93A, H46R/H48Q, and L126Z, for a total of 24 images.

4.3.5 FTIRI DATA ANALYSIS

Data were analyzed using Cytospec (version 1.4.02). Quality tests based on sample thickness and signal to noise ratios were performed on each pixel to remove bad spectra. The sample thickness was determined by the integration over the region from 950-1710 cm^{-1}, where the lower and upper limit integration values were 70 and 360, respectively. This primarily removed bad pixels from the edge of the tissue where the tissue was either too thin or folded. The signal to noise ratio was determined over the 1600-1700 cm^{-1} for the signal region and the 1800-1900 cm^{-1} for the noise region. Spectra with a signal to noise ratio below 90 were eliminated to remove spectra of poor quality. Of the spectra that passed the quality tests, the first derivative was taken, using a 9-point Savitzky-Golay algorithm. To separate different histological regions, i.e. the gray versus the white matter, a hierarchical cluster analysis (HCA) was performed on the first derivative spectra based on the protein (1600-1710 cm^{-1}) and lipid (2570-3025 cm^{-1}) spectral regions. On average, three clusters were required to distinguish the regions of interest (ROIs), namely the gray and white matter. The third cluster contained a mixture of the gray and white matter at the interface of the two regions and was not analyzed. Masks were created based on the HCA for the gray and white matter. The masks contained a matrix of ones and zeros, which were multiplied by the FTIR images, creating an image with only data points in the white matter or gray matter, enabling each region to be analyzed separately.

The level of unsaturated lipid was determined based on the olefinic =C-H vibrational mode at 3012 cm^{-1}. Specifically, the olefinic lipid peak was integrated from 2995-3025 cm^{-1}. This region was normalized to the total lipid region (C-H stretch) from 2750 and 3025 cm^{-1}, which accounts for any variation in sample thickness. A linear baseline was used over the same spectral region for both the olefinic and total lipid regions. Due to the low levels of unsaturated lipids, we chose to represent the data as a percentage of total pixels that contained zero olefinic content. This percentage shows the fraction of pixels with no detectable unsaturated lipids. Therefore, a higher percentage of zero olefinic values suggest lower levels of lipid unsaturation and more oxidative damage.

Mean values were obtained for the integration profile for both the gray and white matter, separately. An independent-sample t-test was performed between each group to determine statistically significant differences using SPSS software (version 14.0). Significance was achieved for $p < 0.001$.

A principle component analysis (PCA) was also performed on the FTIRI data using the Perkin-Elmer Spotlight program. This program enabled the separation the gray and white matter using lipid and protein regions of the spinal cord and generated an image that is similar to that of a visible microscope but showing contrast between the gray and white matter. These images were used for comparison with the FTIRI images shown in **Figure 4.2**.

4.4 RESULTS

Figure 4.1 shows the oxyblot results and relative levels of protein carbonylation from the WT, G37R, G93A, and H46R/H48Q mouse spinal cords [154]. These results show that G37R mice contain significantly lower protein carbonyls in the SOD1 protein than the WT,

H46R/H48Q, and G93A samples. The decrease in protein carbonyls is associated with lower protein oxidation, a result of oxidative stress.

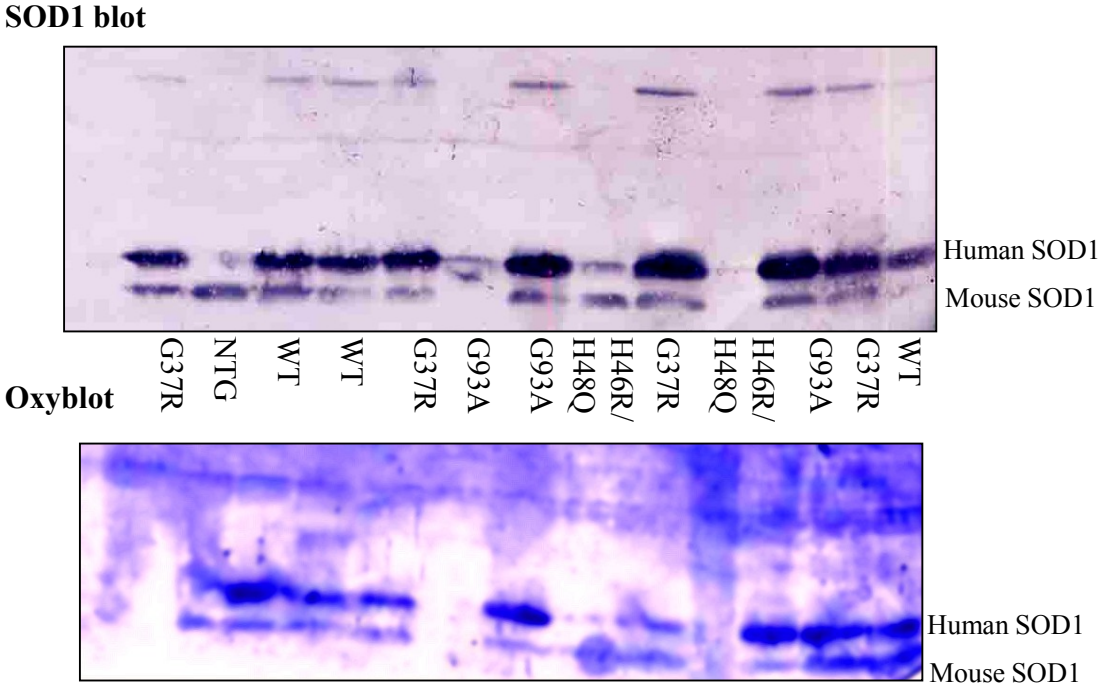

FIGURE 4.1 SOD1 Western blot and oxyblot from spinal cord extracts of SOD1 to determine the levels of protein carbonylation. The WT, G93A, and H46R/H48Q SOD1 contained elevated levels of protein carbonyls compared to the G37R SOD1 [154].

Figure 4.2 shows representative FTIR images from the spinal cords of each mouse genotype: NTG, WT, G37R, G93A, H46R/H48Q, and L126Z. The olefinic / total lipid ratios for the gray matter were extremely low and no statistically significant differences were seen. The gray matter consists primarily of cell bodies so the lower lipid content was expected and the level of unsaturated lipid was undetectable by FTIRI. Conversely, the white matter consists of myelinated axons so the olefinic lipid content was higher. **Figure 4.3** shows a box plot of the "percentage of zero pixels" in the white matter.

Results showed the level of lipid unsaturation in the white matter of the WT mice was significantly lower than the NTG (percent difference = 60.66%), suggesting that these mutations had increased lipid damage. In contrast, the mice overexpressing SOD1 mutations had similar levels of lipid unsaturation in comparison to the WT mice. However, the level of lipid unsaturation in the G37R mice was significantly higher than the other transgenic mice, suggesting reduced lipid peroxidation.

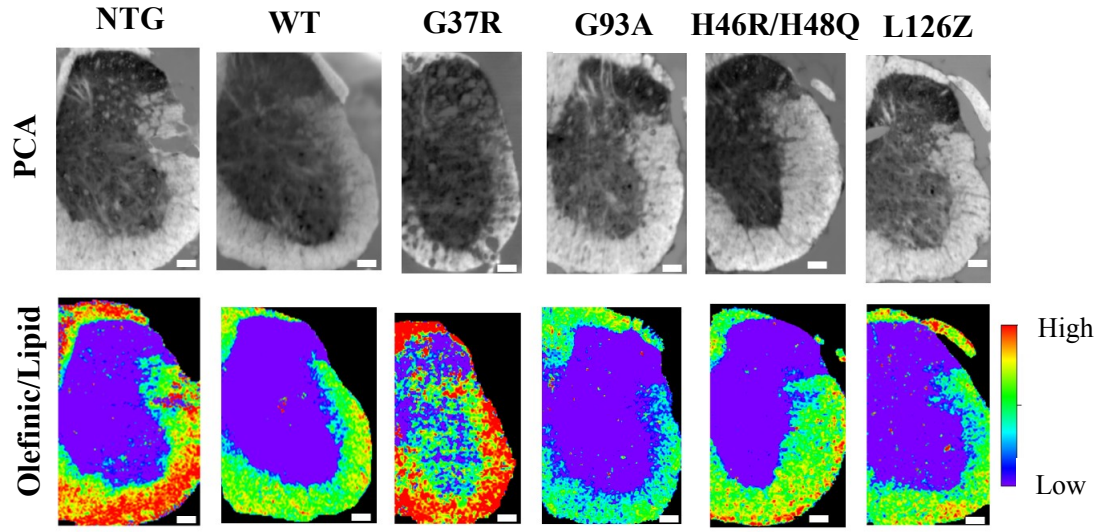

FIGURE 4.2 Infrared images from spinal cords of SOD transgenic mice and NTG control. Principle component analysis (PCA) images are shown in the top row that shows the gray matter in the center of the spinal cord and the white matter on the outside. The PCA divided these two regions based on the high protein content in the gray matter and the high lipid content in the white matter. The bottom row shows images from the olefinic to lipid ratio, a measure of lipid unsaturation. These images show the relatively high levels of unsaturated lipids in the NTG and G37R mice compared to the WT and other SOD mutants.

4.5 DISCUSSION

Oxidative stress is commonly seen in ALS, and it is thought to play a role in the death of motor neurons. Results showed that the spinal cords from WT SOD1 mice contain decreased lipid unsaturation compared to NTG mice. This is an especially intriguing outcome since the WT

mice do not develop ALS symptoms, and the WT mutation should be properly metallated and fully functional. This suggests that there is some oxidative damage associated with the overexpression of WT SOD1 in mice. WT SOD1 overexpression has been shown to have a beneficial effect on cells [155], though overexpression of WT SOD1 in mice is associated with some evidence of ALS-like symptoms [156]. In mice over 30 weeks old an increase in the number and size of mitochondria has been found, and there was evidence of vacuoles with remnants of mitochondria [44]. These mice also showed axonal degeneration and can accumulate WT SOD1 in their motor neurons. In older mice (70+ weeks) motor performance was impaired compared to non-transgenic mice of the same age, which was also accompanied by motor neuron loss [157]. Additionally, the co-expression of WT-SOD1 in a G93A mouse drastically increased the progression of the disease. This suggests that high concentrations of WT-SOD1 may be deleterious. The ALS-like symptoms caused by the WT-SOD1 overexpression in mice may help to explain the increased markers for oxidative stress in the WT mice.

The levels of protein carbonyl and lipid unsaturation were very similar between the WT and the mutants: G93A, H46R/H48Q, and L126Z. The presence of oxidative stress markers in the G93A mouse agrees with a previous study that found a 557% increase in protein carbonyls in G93A mice between 100 and 120 days old compared to WT SOD1 and non-transgenic controls, indicating increased hydroxyl radical production is associated with the expression of the G93A mutation [113]. Also, in G93A increased oxygen radicals have been detected using *in vivo* spin trap experiments [158]. However, these studies have compared a single mutation to WT-SOD1, rather than several different mutations. In the present study, both WTL and MBR mutations were studied to determine how they affect levels of oxidative stress. We found evidence of oxidative

damage in both types of disease-conferring mutations, indicating that the metal binding ability of the mutant SOD1 is not a factor in oxidative stress.

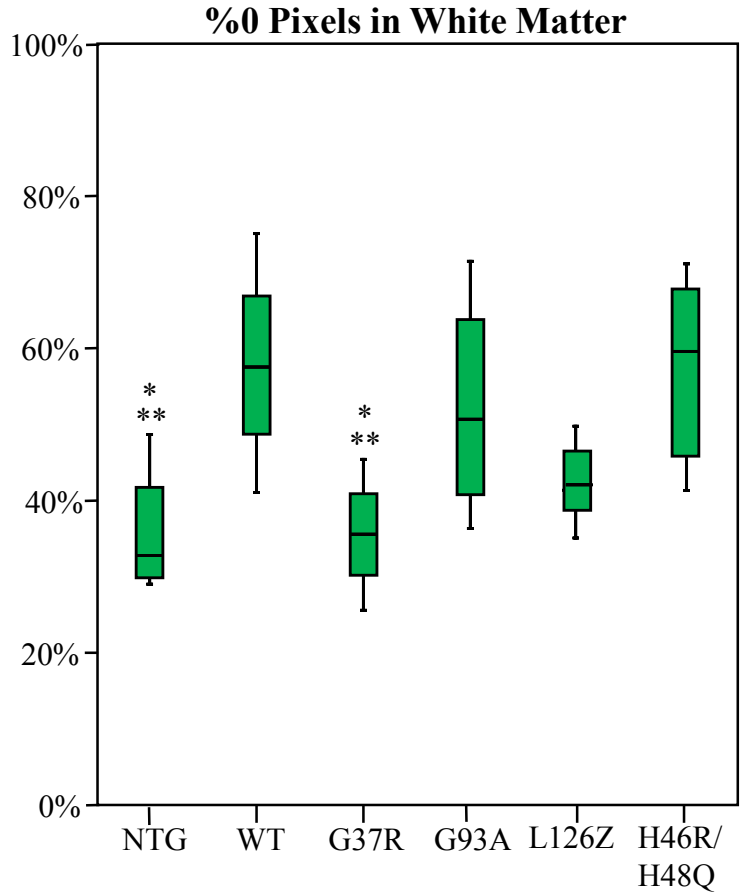

Figure 4.3. Box plots of the percentage of pixels with a zero value for the olefinic to lipid ratio in the spinal cord white matter from NTG, WT, G37R, G93A, H46R/H48Q, and L126Z SOD transgenic mice. The decrease in percent zero can be seen in the NTG and G37R mice compared to the WT and other mutations (*, significantly different from WT; **, significantly different from H46R/H48Q by Kruskal-Wallis and Mann-Whitney U tests).

Interestingly, the results showed that G37R mice contained the lowest levels of protein carbonyl and the highest levels of lipid unsaturation compared to the other mutations and the WT mice. These results indicate that G37R has reduced oxidative damage compared to the other transgenic mice. A previous study also found no increase in protein-bound nitrotyrosine or hydroxyl radicals in the G37R mice compared to WT-SOD1 and non-transgenic mice [88]. Thus it appears that G37R has uniquely reduced markers for oxidative stress.

The copper bound to SOD1 is responsible for its antioxidant activity, but it is also hypothesized to play a role in the toxic gain of function of SOD1 in ALS. Specifically, the SOD1 mutations are thought to have the copper loosely bound [159] or improperly exposed copper to the surroundings [160], generating ROS and subsequently resulting in increased oxidative stress. The G37R mutation alters the structure of SOD1 in relatively minor ways and does not appear to significantly affect the metal binding region [158]. Therefore, the copper site should be properly protected as in the WT protein and should not increase the likelihood of aberrant copper reactions.

In contrast, the other mutants involved in this study affect the copper binding in SOD1 in different ways. For example, the G93A mutation affects the distant metal binding region [161] and may result in increased exposure of the copper ion. While the MBR mutations are often considered relatively inert because they lack the ability to bind copper, the copper may still be present in the CCS bound to the SOD1. The copper chaperone for SOD1 (CCS) is responsible for delivering the copper to SOD1 and forming the disulfide bond found in a normal SOD1 monomer. It was recently shown that CCS forms a very stable complex with the H46R/H48Q mutant [138]. The CCS is a possible source of reactive copper in the MBR mutations that could lead to an increase in oxidative stress through aberrant copper binding or improper exposure of copper. The L126Z is mutation an unstable and short-lived protein that lacks the beta strand required for CCS recognition. The beta strand also includes the cysteine residue at position 146 used in the disulfide bond [162], which accounts for the instability of L126Z. Though not statistically significant, L126Z has increased levels of lipid unsaturation compared to WT, G93A, and H46R/H48Q. This may be due, in part, to the protein's short lifetime and lack of copper. Thus, the relatively unperturbed copper binding site of G37R may lead to less aberrant

redox chemistry compared to the other mutations that have altered structure or strong associations with the CCS protein and could result in reduced oxidative stress.

In addition to the relatively protected copper site of SOD1, the G37R mutation may also be more prone to aggregation. One of the mechanisms proteins employ to prevent aggregation is to possess a large net charge (either positive or negative), because the electrostatic forces will repel the proteins away from one another [163]. At physiological pH, SOD1 contains a net negative charge between -6 and -7 [164]. The point mutation G37R results in a reduction of the net negative charge in SOD1, making the protein more prone to aggregation [163]. It is widely believed that the soluble form of mutant SOD1 is most toxic to the cells and that aggregation is a defense mechanism to sequester the aberrant proteins. Therefore, a mutation that encourages aggregation, such as the net charge decrease in G37R, may aid in sequestering the mutant protein and result in reduced levels of oxidative stress. To confirm this hypothesis, other mouse models of SOD1 mutations with a net decrease in charge, such as the single mutation H46R, need to be studied. However, in an extensive study of SOD1 mutations in transfected cells, changes in net charge did not explain aggregation propensity, and the G37R mutation showed only moderate aggregation compared to the other mutations [35]. Interestingly, some SOD1 point mutations with a net charge decrease are associated with some of the longest survival times of FALS patients. For example, the average survival time of a patient with the G37R or H46R point mutation is over 17 years [165]. This is a significant increase compared to most other mutations with average survival times between two and five years. An increase in G37R aggregation could reduce levels of oxidative stress from the toxic soluble protein, which may help to increase the survival times in human patients with this mutation.

The reduction in oxidative stress markers in the G37R mice and the longer survival time of humans with the G37R mutation argues that reducing the levels of oxidative stress through the use of antioxidant drugs may be useful in prolonging the lives of ALS patients. Interestingly, riluzole, the only approved drug for ALS patients which inhibits glutamate release [166], has also been shown to be an antioxidant in cultured cortical neurons [167]. Other antioxidants, such as vitamin E, have been used with some success in delaying symptoms in mouse models [168]; but in clinical trials there have been few successes [169, 170]. However, the translation between mouse studies and human clinical trials has faced significant challenges [171, 172]. For example, many mouse studies rely on the SOD1 mutation, which only affects 2.5% of all ALS patients [172]. Additionally, many treatment studies in mice begin before the onset of the disease. While this does provide the best opportunity to delay the disease onset and slowing of the disease, it is not currently possible in a clinical setting with human patients.

4.6 CONCLUSION

There is significant evidence that oxidative stress is a major factor in the progression of ALS. We have investigated how markers of oxidative stress, protein carbonyls and lipid unsaturation are affected in transgenic mice overexpressing WT SOD1 as well as WTL and MBR mutations. While no correlation was found between the different types of mutations and the degree of oxidative damage, the G37R mutation showed no observable oxidative stress. This mutation is associated with a protected copper site, a net charge decrease that may make this mutant more prone to aggregation, and a longer life expectancy in human patients. In the future, additional studies could examine oxidative stress in other mutations that possess similar

properties, such as H46R or E100K. Reducing levels of oxidative stress has the potential to be a viable treatment option for ALS patients.

CHAPTER 5

FUTURE DIRECTIONS

5.1 LIVE CELL INFRARED IMAGING TO UNDERSTAND THE MECHANISMS OF PROTEIN MISFOLDING AND AGGREGATION IN ALS

5.1.1 ABSTRACT

FTIR provides valuable chemical information about biological systems including protein secondary structure. Monitoring these changes in real time with respect to disease progression or exposure to a potential drug is very useful in determining the underlying mechanisms of biological processes. However, FTIR imaging (FTIRI) of live cells is complicated by the large IR absorbance of water. Specifically, the strong water absorption band at 1640 cm^{-1} overlaps with the amide I region, where protein secondary structure can be identified. Thus, most FTIRI of biological specimens is performed on dried cells. However, many diseases are accompanied by dynamic changes in protein secondary structure, and these processes are not well understood. The ability to image living cells in real time can provide significant insight into the process of protein misfolding in real time. Imaging live cells requires the consideration of several factors to maintain cells for a long period of time and minimize water absorption. Cells require a sterile, nutrient filled, warm environment to survive. In this chapter the ongoing efforts to develop a cell incubator to accommodate the needs of the cells during the course of the experiment will be discussed. To minimize the water absorption, the path length of the chamber will be limited to 10

μm or less, and water subtraction methods from the spectra will also be utilized. The incubator will use a pump to flow media through the chamber to ensure the cells have sufficient nutrients, and the cells will be kept warm on a heated stage. This will allow for the imaging of the same group of cells over the course of an experiment.

5.1.2 INTRODUCTION

Live cell imaging has become an important tool to monitor biological processes as they occur dynamically in live cells, rather than in fixed and dried samples. This technique allows the same cells to be imaged repeatedly over the course of an experiment, thus reducing the variability added by studying different cells as typically done in time course studies that are used to study cellular processes. However, in the infrared region live cell imaging is challenging due to the strong absorption of water from the H-O-H bending mode at 1640 cm^{-1}, which overlaps with the amide I absorption band (C=O stretch from the protein backbone). Water also contains two other modes in the mid-infrared region: the symmetric and asymmetric O-H stretches at 3277 cm^{-1} and 3490 cm^{-1}, respectively; and mixture of the bending and libration (frustrated rotation) modes at 2150 cm^{-1} [173, 174]. **Figure 5.1** shows the overlaid spectra from water and from a cell with the overlapping absorption bands around 1640 cm^{-1}. The amide I band is an important feature in the infrared spectrum because it is very sensitive to protein secondary structure. In many diseases, such as ALS and AD, misfolded proteins lead to the formation of aggregates. In the IR spectrum this process can be observed by the peak shift in the amide I band based on the hydrogen bonding environment within the protein. Assignments have previously been made to alpha helical structure which appears at 1654 cm^{-1}, beta sheets at 1630 cm^{-1}, and aggregated beta sheet at 1620 cm^{-1} [84]. To analyze the amide I band in hydrated live cells, the amount of water needs

to be minimized so the absorption is attenuated and/or the water needs to be mathematically removed from the spectra. The ability to monitor biological processes in living cells, such as protein aggregation, would be a valuable tool to understanding cellular events. This is an ongoing project to develop a chamber or incubator to maintain living cells while collecting infrared data to study biologically relevant processes in a time resolved manner.

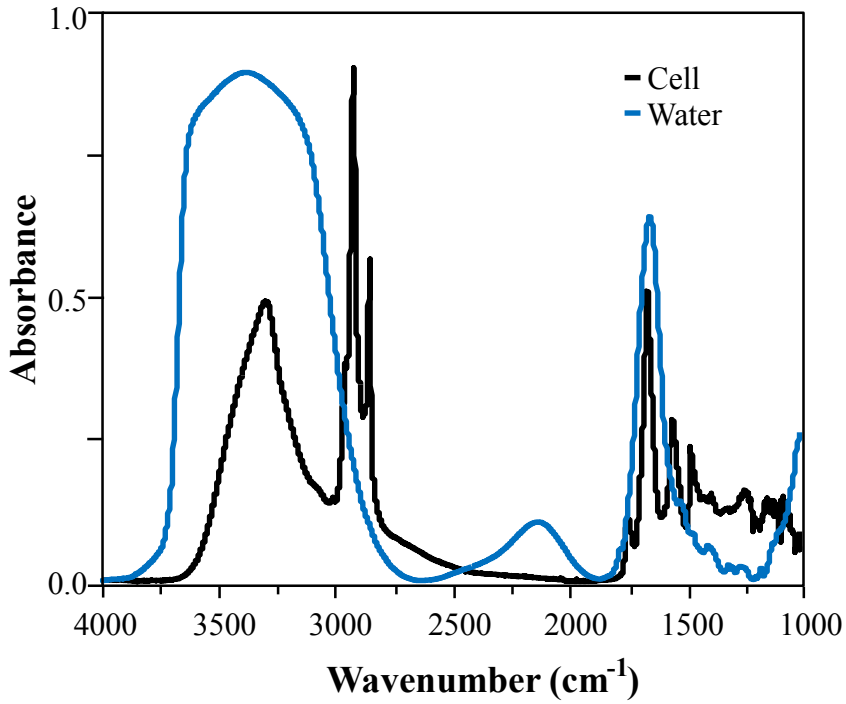

FIGURE 5.1 IR spectra of water (blue) and a biological specimen (black) demonstrating the overlapping vibrational mode of water at 1643 cm^{-1} with the amide I band from the protein content.

Several other groups have also worked on FTIRI of live cells by creating novel chambers to serve as incubators for live cells during experiments. One such design uses sub-micrometer diamond windows, which are IR and visible light transparent, to aid in minimizing the chamber thickness [175]. Other designs utilize lithography to pattern spacers of precise thickness onto calcium fluoride windows [176, 177] and microfluidics to flow media to the cells [178]. Additionally, modifications have been made to commercially available flow cells to

accommodate the needs of live cells with thinner spacers and micro-patterned channels for flow [179]. Other groups have also implemented the use of attenuated total internal reflectance (ATR), a technique that can improve the spatial resolution, to study cancer cell growth [180, 181]. In a more recent study, the ATR crystal was attached to the IR objective allowing data to be taken directly from a petri dish [182]. These chambers vary significantly in design, but they all maintain a low profile to accommodate small working distances and/or to minimize water contribution, and they flow nutrients to the cells.

Live cell imaging experiments have been used study a wide range of biological processes. In experiments to monitor the cell cycle in human fibroblasts and bacterial biofilms with IR, where relative increases in DNA were observed during DNA replication [178, 183], while subtle decreases in protein content were observed during cell starvation [184]. The effects of mechanical compression showed alterations in protein biosynthesis and lipid metabolism upon deformation of the living cells [177]. The effects of drug response have also been studied in HeLa cells exposed to antitumor agent, in which principle component analysis (PCA) showed minor alterations in spectra compared to untreated cells [185]. However, these previous studies generally focus on the nucleic acid region or lipid regions of the IR spectrum, which are less affected by the presence of water; and no previous study has examined protein secondary structure in living cells.

The ultimate goal of this work is to study changes in protein secondary structure during aggregate formation of copper-zinc superoxide dismutase (SOD1) in living cells using the Amide I band.

5.1.3 APPLICATION OF LIVE CELL FTIRI TO ALS

Mutations in the protein copper- zinc superoxide dismutase (SOD1) have been linked to a familial version of the disease, and the mutant SOD1 forms aggregates in the motor neurons in the spinal cord of ALS patients. The process of aggregation is not fully understood, so insights into the changes in protein secondary structure may help to determine the molecular events in protein aggregation. Cells transfected to express mutant SOD1 will be used to monitor the formation of intracellular aggregates of SOD1 that develop. There are a variety of different mutations that occur in SOD1 that affect metal binding affinity and activity so several different mutations will be considered. A4V and G37R mutations are wild-type like mutations, which bind copper and zinc and maintain a similar activity to the wild-type protein. H80R and D125H are mutations that affect the metal binding region and, as a result, significantly reduce the activity of the protein. These different properties in the mutants may influence the aggregation pathway. The SOD1 will be co-expressed with YFP to confirm the presence of the aggregates in the cells. The goal of this experiment will be to monitor changes in protein secondary structure in the various SOD1 mutations as aggregation occurs in transfected living cells using FTIR imaging.

5.1.4 LIVE CELL CHAMBER DEVELOPMENT AND DESIGN CRITERIA

Accommodating the requirements of both the cells and the infrared experiment is very challenging. A basic chamber for live cell FTIRI is modeled after a cell culture incubator and an IR cell for collecting data of bulk solutions.

Thickness minimization: Limiting the thickness of water to below the diffraction limit (~10 μm) is very useful in reducing the amount of water absorption seen in the infrared spectrum. However, most cells are just under 10 μm thick so care must be taken to avoid damage to the cells in the process of minimizing the water. Pressure and stress on the cells add more unnecessary variables to the experiments. Thus, spacers are used to maintain an appropriate thickness and to avoid damaging the cells. Spacers are made using a photoresist, patterned onto one of the calcium fluoride windows with lithography. Two different photoresist materials were tested, SU-8 and AZ4620. Neither material affected cell growth, but the AZ4620 photoresist detached from the windows when used with the cell culture media. The SU-8 photoresist was more resilient and can be permanently attached and was chosen as the ideal material. The thickness of the photoresist can be carefully selected based on the viscosity of the material and the revolutions per minute (RPM) at which the photoresist was applied. This process allows for an optimal spacer thickness of approximately 8-9 μm to be reliably produced. Another advantage of using the photoresist spacer is that it can be permanently adhered to the window so it is not easily lost or difficult to handle, as traditional spacer materials of similar thickness tend to be.

Cell culture requirements: Providing the appropriate level of nutrients to the cells with minimal coverage of aqueous media is an important consideration. We have calculated that the total volume of media in the chamber is about 1 μL, which is quickly consumed by the cells resulting in increased cell death. Thus, to provide sufficient nutrients to the cells, the media will be slowly circulated through ports to the chamber using a peristaltic pump, allowing fresh nutrients to circulate constantly. Cells also require a warm environment (37 °C) so a warm stage (Linkam THL60-8) is used to keep the cells at a stable physiological temperature. The stage has

a small hole (~2 cm in diameter) in the center to allow for the transmission of IR light. In addition, a typical incubator is supplied with ~5% CO_2 to maintain a neutral pH in the media, but adding CO_2 into the circulating media created bubbles in the chamber that led to the cells drying out from exposure to air rather than media. To circumvent this problem, ultra-buffered CO_2 independent media was used. Commercially available CO_2 independent media can also be used with added supplements as needed for each cell line, including the CHO-K1 cells. However, cell transfections were not successful with this media. Thus, buffer solutions were added to the typical media to create a CO_2 independent formula. HEPES and potassium phosphate buffers were both tested separately in 10 and 20 mM total concentrations to determine the optimal buffer and concentration for the transfection media. Cells were acclimated to the buffer solutions with a 50/50 mixture of normal buffer and the CO_2 independent media for two days before changing to 100% CO_2 independent media. The cells cultured with a potassium phosphate buffer had a lower survival rate, and it was eliminated as a possible buffer for CO_2 independent transfections. However, the CHO-K1 cells were best with 20 mM HEPES (4-(2-hydroxyethyl)-1-piperazineethanesulfonic acid) buffer added to the normal F12-K media allowing for CO_2 independent transfections with approximately the same transfection rates as the cells in normal media with CO_2 added. HEPES is known to become cytotoxic when exposed to light. Thus, cells were maintained in the dark, except when images were acquired, and no adverse effects were observed. These adjustments have been very useful in sustaining the cells in the chamber for a period of approximately 24 hours, which is long enough to do many biological experiments.

FTIR microscope considerations: This experiment is well suited for an FTIR microscope with a focal plane array (FPA) detector, such as the Bruker Hyperion. The FPA detector acquires an

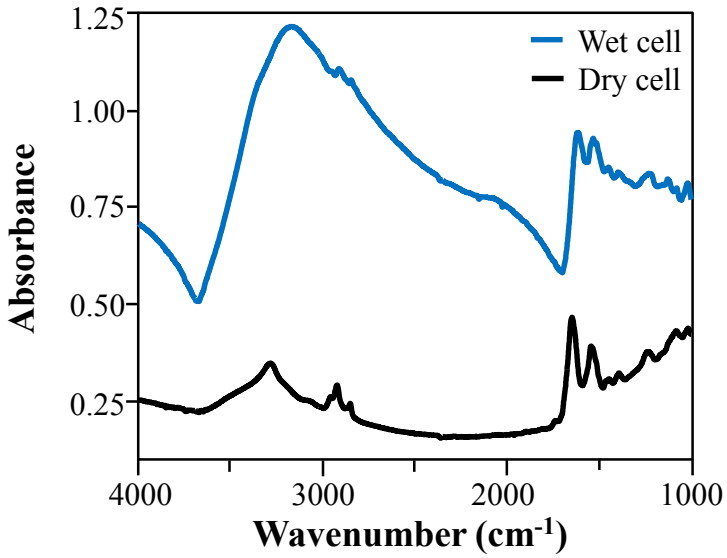

FIGURE 5.2 FTIR spectra from a dried cell (black) and from a hydrated cell (blue) grown on an ATR hemisphere in a chamber with a gold mirror to reflect more IR light. Using a water background, the amide and lipid peaks are visible, but the apparent peak shift is a result of poor background subtraction.

array of spectra from an area of the sample simultaneously and quickly, without the need to raster scan across the sample. This drastically reduces the amount of time spent collecting each data point. The working distance of the 74x objective is 1.5 mm. Thus, the distance from the objective through the chamber and its top window to the cells must be less than 1.5 mm. This adds an additional engineering constraint to the chamber and requires the minimization of material above the sample. A lower power objective, with a larger working distance, could be used; but this will increase the pixel size. As a result, several chamber designs have been tested to accommodate the high-powered objective, and they utilize thinner (0.5 mm) calcium fluoride windows, which are typically 1 mm. Unfortunately, these thinner windows are more flexible so when pressure is applied to the edges, as in the chamber designs, the window bows and causes the middle of the chamber to be thicker than on the outer edges. The additional thickness adds

more water to the area, creating a larger and undesirable water absorption band. The use of stronger and less flexible IR transparent materials, such as diamond, is under consideration.

Attenuated total reflectance: To further enhance the spatial resolution of FTIR, attenuated total reflectance (ATR) can be used. With ATR, the spatial resolution is improved by a factor of the refractive index of the ATR material used (i.e. 2.4x for zinc selenide (ZnSe)). For ATR to occur, the light must enter the material at an angle greater than that of the critical angle. At each bounce of the light within the ATR crystal an evanescent wave escapes. It is this wave that is used to probe a sample on the ATR crystal. The evanescent waves are small and have a penetration depth of approximately one micron (depending on the refractive index of the crystal, the wavelength of light, and the angle of incidence) [186]. On a cellular level, this correlates to the evanescent wave penetrating though the cell membrane and into the cytosol. In the future, cells could be grown on an ATR material, such as ZnSe, rather than an FTIR window. In addition to the added spatial resolution provided by the ATR crystal, the evanescent wave that is collected only penetrates the sample about one micrometer, which avoids the bulk water in the media. This could improve the quality of the data and reduce the constraints on thickness of the spacers used, creating a more cell culture-like environment for the cells. **Figure 5.2** shows representative spectra taken from a dried cell that was then rehydrated with PBS. The cells were grown on the ATR crystal, and to improve the signal a gold mirror was also used to reflect the IR light. The peaks shown in the wet cell spectrum are shifted and misshapen due to improper background subtraction from the hydrated cell so water subtraction is necessary.

Current Chamber: The most recent chamber model, shown in **Figure 5.3**, contains two IR transparent calcium fluoride windows with a spacer and sample solution in between the windows. Here adherent cells are grown on one of the windows in a typical cell culture incubator and petri dish. Once the cells have attached to the window they can be transferred into the chamber, covered with cell culture media, and used in an FTIRI experiment.

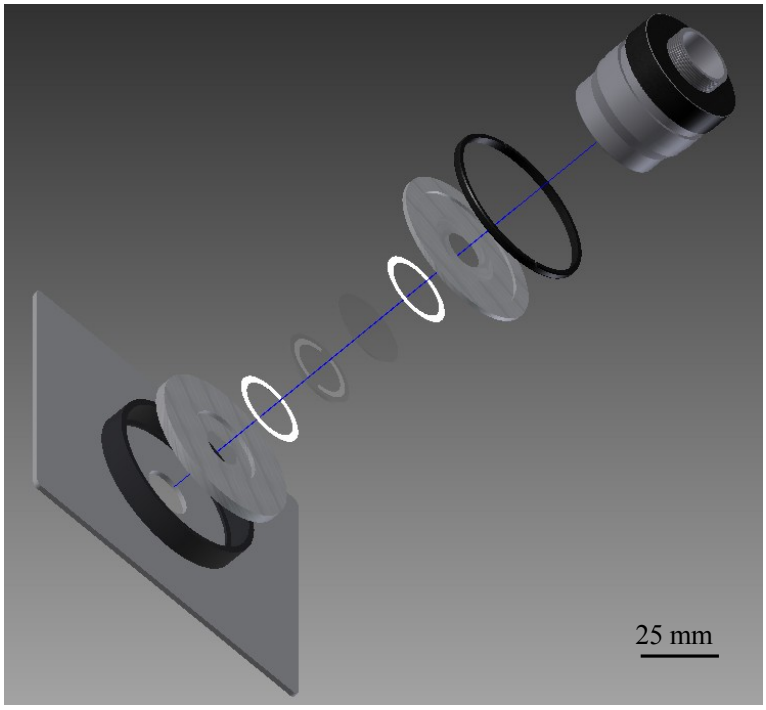

FIGURE 5.3 Schematic of chamber for live cell imaging. An aluminum bottom piece has a hole cut into it to allow the IR light to come through the chamber and has a groove cut into it to allow a 25 mm diameter calcium fluoride window to sit inside. This window is 1 mm thick and contains an 8 μm SU-8 photoresist spacer. The top window is also 25 mm in diameter but only 0.5 mm thick. The cells are grown on the center of this window. A thin aluminum top, designed to apply pressure uniformly, is placed on top of this calcium fluoride window. This top aluminum piece also has a groove cut into it to allow the IR objective to fit inside of the chamber, which is needed due to the 1 mm working distance. Teflon spacers are used between the calcium fluoride windows and the aluminum surfaces to prevent scratching and breaking of the windows. All components of the chamber fit inside the black threaded column; and the top ring, which can be screwed into the threaded base, seals the chamber. This design allows the chamber to sit under the 74x objective at the Bruker Hyperion microscope.

5.1.5 WATER THICKNESS AND ABSORBANCE TESTING

Understanding the relationship of water absorbance with respect to the thickness of the water is important in determining the optimum water thickness. The strong H-O-H bending mode of water at 1640 cm^{-1} is easily saturated, causing problems when taking background measurements on water, without cells, and for water subtraction. Both of these methods require the precise absorbance of water to be accurately measured to remove the water peak and reveal the amide I band. The Beer-Lambert law allows for the calculation of water absorbance at different thicknesses:

$$A = b\ c\ \varepsilon \qquad \text{(Equation 1)}$$

where A is the absorbance, b is the path length (or thickness of water), c is equal to the molar concentration, and ε is the absorption coefficient at 1640 cm^{-1}. The absorption coefficient of water was determined to be 21.8 M^{-1} cm^{-1} [187], and the molarity of pure water is 55 M. At an absorbance greater than 1.5, the only 3.2% of the light is transmitted. Thus, to maintain sufficient transmittance, the thickness of water must be below ~10 μm. The calculated 10 μm maximum thickness was confirmed experimentally using IR fringing patterns to determine the thickness of water [188]. Specifically, an empty (liquid free and air filled) flow cell was measured with different spacer thicknesses to obtain the fringing patterns, which are more obvious with air than in water due to the greater difference in refractive index between air and the calcium fluoride windows. Then, water was injected into the flow cell to determine the IR absorbance of water without opening the cell or changing the thickness. The results of this experiment and the calculated values were nearly identical and are summarized in **Figure 5.4**. Based on this information, the optimum thickness of water is below 10 μm, to avoid a saturated peak and greater than 7 μm to avoid damaging the cells or depriving them of water and nutrients.

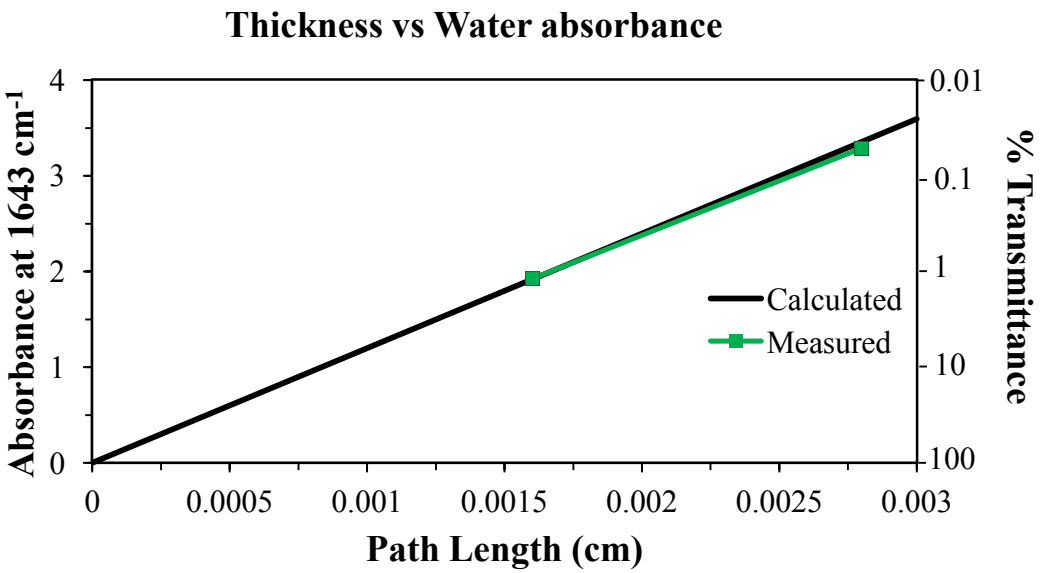

FIGURE 5.4 Calculated and measured absorbance of water with respect to thickness, based on the Beer-Lambert law. At an absorbance of 1.5, the transmittance is only about 3%. Thus, the thickness of water should be less than 10 μm thick to allow adequate transmittance of light.

5.1.6 PRELIMINARY EXPERIMENTS WITH POLYSTYRENE

Preliminary experiments and testing of chambers were performed with polystyrene (PS) beads that are 2, 6 or 10 μm in diameter. PS beads are useful to test new chamber designs because they are approximately the same size and shape as the cells, but they do not have any life-sustaining requirements, unlike live cells. When exposed to ultraviolet (UV) light, PS can undergo a photooxidation reaction resulting in the formation of a carbonyl peak at 1725 cm^{-1}. The reaction begins with a radical abstraction of hydrogen from the polymer backbone, followed by β-scission, which leads to the formation of a ketone and the generation of the peak at 1725 cm^{-1} [189]. **Figure 5.5** shows the changes in the FTIR spectra before and after 30 hours of UV irradiation. This peak also overlaps with the strong water absorption band at 1640 cm^{-1}, so it provides a good test for the water subtraction and for the real time monitoring of changes in this region without the use of more complicated cells and transfection experiments.

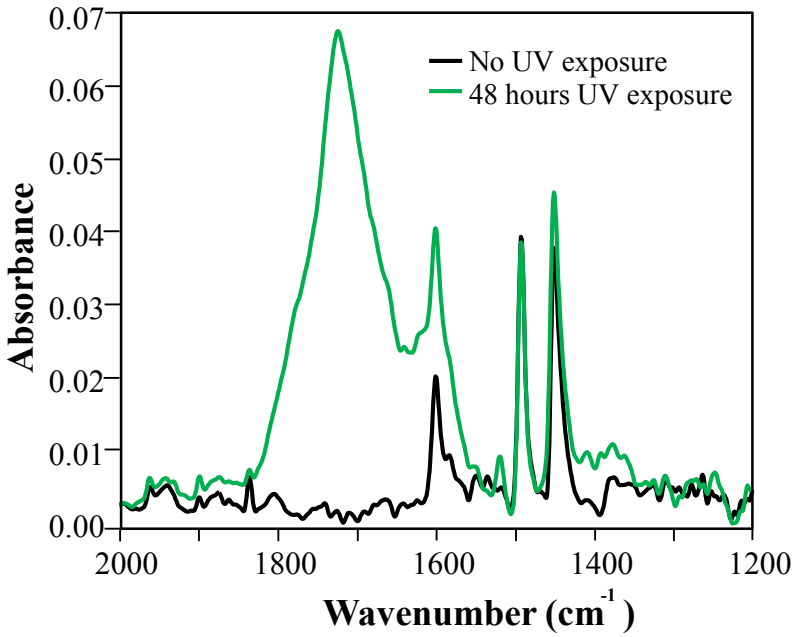

FIGURE 5.5 Polystyrene beads (2 µm diameter) before (black) and after (green) 48 hours of UV irradiation. The increase in the carbonyl peak at 1723 cm^{-1} arises from the photoxidation of polystyrene.

5.1.7 PRELIMINARY LIVE CELL RESULTS

Cells transfected to express mutant SOD1-YFP were imaged at the Hyperion IR microscope at beamline U10B at the NSLS, but without flowing media. The cells were grown on calcium fluoride windows and transfected in the petri dish in a conventional incubator. To prevent cells from growing on the edges of the window, where the spacer would damage the cell, kapton tape was used to cover the outer area the window. Before placing the window in the chamber, the tape was removed ensuring that the cells were only in the center of the window. Ten hours after the transfection was initiated the cells were transferred to the IR chamber and imaged using FTIRI over the course of several hours. A field of cells was selected based on the presence of dimly fluorescent cells. It was anticipated that the fluorescence and protein content would increase with time; but the water in the chamber slowly dried out. As a result the lipid

region, which over laps with the water O-H stretching mode, appears to increase (**Figure 5.6**). This apparent increase is likely due to less water in the spectrum, making the lipid regions of the cell appear more intense.

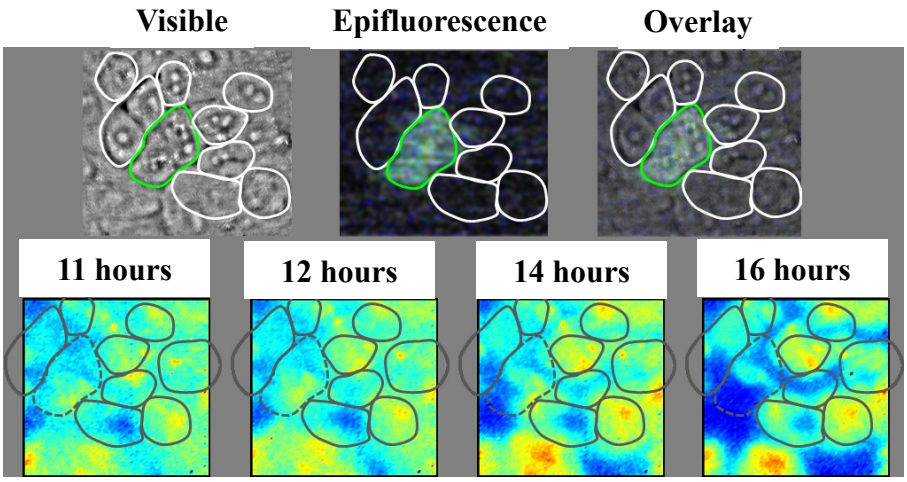

FIGURE 5.6 CHO-K1 cells transfected to express SOD1-YFP. Top row - visible image from the FTIR microscope (left), the epifluorescence image (middle), and the composite image (right). The fluorescent cells are outlined in green, and the untransfected cells are outlined in white. Bottom row - FTIRI images from the CHO-K1 cells of the same area. The transfected cells are outlined with a dashed line, and the untransfected cells are outlined with solid lines. In these images, the cells appear have an increase in the lipid region (2750-3025 cm^{-1}) of the same live cells between 11 and 16 hours post transfection. The changes are likely due to the loss of water from the chamber during the course of the experiment. As the absorbance of lipids also overlaps with the O-H stretching mode of water, the decrease in water content results in an apparent increase in lipids.

Subsequently, transfected cells have been maintained in the lab under a visible microscope for over 12 hours in a traditional FTIR flow cell chamber with a 10 µm spacer. The cells were grown on a calcium fluoride slide and transfected in a petri dish. Twelve hours after the transfection was started the cells were moved to the chamber with a warm stage, and ultra-buffered transfection media was circulated through the flow cell. Images of the YFP fluorescence were taken every hour, resulting in a "movie" from the accumulation of a series of images of aggregate formation and cell death, and representative images are shown in **Figure 5.7**.

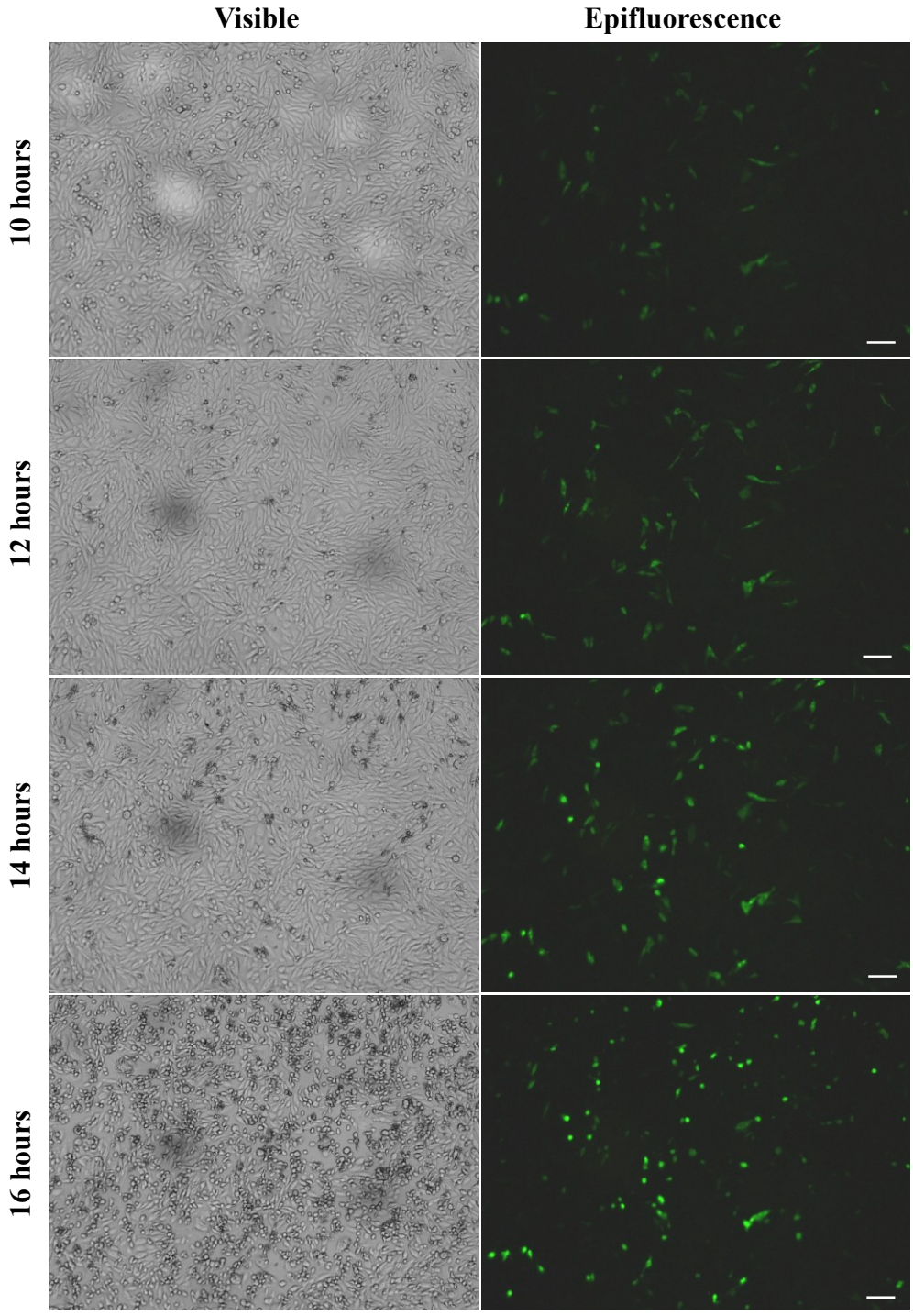

Figure 5.7 Visible (left) and epifluorescence (right) microscope images from the live cell "movie" of G37R SOD1-YFP transfected cells at 10, 12, 14, and 16 hours after initiating transfection. The cells were grown on CaF_2 windows and inserted in to a flow cell. At 10 hours, the cells are dimly fluorescent and fluorescence, and the fluorescence increases through 14 hours. However, by 16 hours the cells appear to be mostly dead (round cells and intensely fluorescent dots). Though CO_2 independent media was flowed through the chamber, the cells may have died due to a lack of nutrients and/or the overexpression of SOD1-YFP. White scale bar = 40 μm.

Based on experiments in normal petri dishes, dim YFP fluorescence was noticeable in the transfected cells after ~10 hours; aggregates form between 18 and 24 hours; and the transfected cells usually die about ~30 hours after being transfected, though the timeline of events is dependent on the specific SOD1 mutation. However, once transfected cells begin producing aggregates, they only live for a few more hours. Unfortunately, the flow chamber used for this experiment was too tall to be accommodated under the 36x or the 74x objective lens at the Hyperion.

5.1.8 NEXT STEPS

In the future, live cell experiments with a modified chamber will be performed at the Hyperion microscope. This will require a lower profile chamber that can fit under the microscope objectives. One major component of this new chamber likely includes a stronger material for the windows than calcium fluoride that will prevent bowing. More rigid materials such as chemical vapor deposited diamond on a silicon wafer have been used successfully [175]. Flowing media through the chamber will also be implemented to provide nutrients for the cells, allowing for much longer experiments. Other groups have added media flow to chambers using microfluidics [176, 190] or with more traditional flow cell ports [175, 179]. Designs for chambers similar to these are currently being tested. Additional improvements in maintaining cell viability in the chambers will also be worked on, which would be beneficial for more long-term experiments. Improving spatial resolution through the use of ATR would also benefit the project significantly as the aggregates are on the order of a few microns in size.

Ultimately, monitoring live cells with FTIRI could provide valuable information about the nature of protein aggregates by observing their formation in real time. Future studies could

also be expanded to understand the effects of novel drugs on cells, such as those that may impact aggregation. Live cell FTIRI is not limited to studying protein secondary structure and could also be used to study cellular events such as apoptosis, mineralization and lipid unsaturation in real time. Experiments such as these could provide invaluable information regarding cellular mechanisms in health and disease.

5.2 Metallation Levels and Metallation States in the Amyloid Plaques from Alzheimer's Disease Mouse Models

5.2.1 Abstract

Alzheimer's disease (AD) is a progressive neurodegenerative disorder that is characterized in part by the formation of plaques composed of the amyloid-β (Aβ) peptide in the brain. AD is also associated with altered metal homeostasis, though the mechanisms associated with this process are not well understood. Previous studies have found large increases of metal in the plaques of human AD patients, but failed to find a similar increase in the plaques from the PSAPP mouse model of AD. Interestingly, this mouse model does not experience any neurodegeneration that is a key component in the human AD brain. To investigate the role of metal ions in neurodegeneration, we employed two additional mouse models of AD that do show neuron loss (5xFAD and APPVn/NOS2 KO) and plaque formation. The metal content within the plaques was determined using X-ray fluorescence microscopy (XFM). An increase in the amount of copper was found in the two models that show neurodegeneration but not in the PSAPP mouse. In addition, iron concentrations are known to increase in the AD brain, but little is known about the type of iron that is present. Thus, the iron oxidation state and coordination were also investigated in the PSAPP, 5xFAD, and APPVn/NOS2 KO mouse models, using X-ray absorption near edge spectroscopy (XANES), to determine if the increase in iron is a different form than the iron contained in a healthy, non-AD brain. Results showed that the iron present was a mostly iron (III) mixed with some iron (II), but no difference in iron coordination was observed between any of the mouse models and the control mice. These results show that the presence of copper in the plaques is correlated with neurodegeneration and that the iron increase

in the AD brain is not related to a change in the type of iron in the brain. The altered metal homeostasis seen in these AD models suggests that the maintenance and control of metal ions is critical to neuronal survival.

5.2.2 INTRODUCTION

Alzheimer's disease (AD) is another neurodegenerative disease that has several properties in common with ALS. Both SOD1-linked ALS and AD involve the aggregation of proteins that are implicated in the disease. Metals are also thought to play an integral role in the progression of AD and ALS. Thus, metal homeostasis is a significant concern. In both diseases the mechanisms of protein aggregation and metal dyshomeostasis are poorly understood.

AD is the most common age-related neurodegenerative disease, affecting about 2% of the population in industrialized countries [191]. Clinically, AD is characterized by memory loss and diminished cognitive functioning. Pathologically, amyloid plaques and neurofibrillary tangles (NFT) are found in the AD brain [192]. The amyloid plaques consist primarily of the amyloid-β (Aβ) peptide, which is produced by the cleavage of the amyloid precursor protein (APP) [133]. The functions of both Aβ and APP are unclear, but there is evidence that APP is an important component in neuronal survival, neurite outgrowth, synaptic plasticity and cell adhesion [193].

Previous studies with human specimens found a large concentration of metal in the plaques compared to the surrounding areas [194]. The difference in metal concentrations inside and outside the plaque was recently reported to be 177%, 466%, and 339% for iron, copper, and zinc, respectively [83, 195]. However, in the PSAPP mouse model there was no increase in the metal content within the plaques. In fact, a net decrease was found for iron (-17%) and copper (-22%), but a relatively small increase in zinc was also observed (29%) [83]. The contrast between

the human plaque data and the PSAPP mouse model has led to questions regarding how and why the two types of plaques are different. One possible explanation is that the human plaques are significantly older than the mouse plaques and have had many years to accumulate metal, while the mouse plaques have had only a few months to undergo the same process. Another potential possibility is that the PSAPP mice do not show neurodegeneration, a hallmark pathology of AD. Given the potentially toxic nature of metals, this has led to the hypothesis that metal accumulation in the human plaques could be related to neurodegeneration.

To study the metal accumulation in the plaques and the relationship to neurodegeneration, we compared the PSAPP mouse plaques to those of two other mouse models of AD that show neurodegeneration and develop plaques at different ages. The PSAPP mouse expresses genetic mutations in the human APP gene, found in AD patients, and overexpresses the presenlin-1 gene, also associated with AD [196, 197]. This produces a mouse model that develops plaques between six and seven months of age. The 5xFAD mouse model (provided by the vanNostrand laboratory at Stony Brook University and Osten laboratory at Cold Spring Harbor) overexpresses mutated human APP with some additional mutations to those found in the PSAPP mice [198]. As a result, these mice produce more Aβ and develop plaques sooner than the PSAPP mice at 1.5 months of age. They also show signs of memory loss and neurodegeneration. The third mouse model, the APPVn/NOS2 knockout (KO) mouse (Colton laboratory, Duke University), overexpresses a similar APP mutation to the other models and does not produce nitric oxide synthase 2 (NOS2) [199]. During acute diseased states, NO, produced in part by NOS2, was shown to be anti-apoptotic and pro-growth. This mouse model exhibits memory loss and neurodegeneration, and it develops Aβ plaques around six months old, and show signs of tau pathology.

In addition to the development of plaques, metal homeostasis is also a known component of AD. Increases of iron in brain iron have been detected in AD patients using magnetic resonance imaging [200-202]. It was recently shown that the PSAPP mice had a 34% increase in iron content in the cortex at early stages of the disease compared to age-matched controls [203]. This increase in iron was not associated with the plaques but suggests that iron dyshomeostasis is a factor in AD at very early stages, making it a promising biomarker for early detection of the disease. The type of iron in the brain has not been well characterized and previous studies have yield some conflicting results [204]. However, a recent study showed that ferritin, a common iron storage protein, was the primary iron component in the brain from an AD mouse model (APP/V717I), and this iron does not interact with iron in the plaques [205].

The goal of this study was to test the hypothesis that the increase of metal in human plaques is associated with the neurodegeneration in AD and to determine if there are any changes in the type of iron present in the AD mouse models compared to control mice. We hypothesized that the models that show neurodegeneration (5xFAD and APPVn/NOS2 KO) would have increased metal in the plaques because the metal in the plaques could be associated with the neurodegeneration, found in AD. We also hypothesized that the type of iron would change between healthy and diseased mice based on changes in iron homeostasis in AD because a change in homeostasis could result in an influx of iron that is different or less well controlled than the iron present in healthy tissues. To test these hypotheses, the metal content and oxidation state of metals in the plaques were examined using X-ray fluorescence microscopy (XFM) and X-ray absorption spectroscopy (XAS), respectively.

5.2.3 MATERIALS AND METHODS

End stage AD mice from two PSAPP mice (56 weeks old), four 5xFAD mice (63 weeks old), and two APPVn/NOS2 KO mice (27 weeks old) were sacrificed and perfused with PBS. The brains were removed and immediately frozen over dry ice and stored at -80°C. The tissues were embedded into OCT and cryosectioned at -12°C to 30 μm thick. The thin sections were carefully mounted on Ultralene film (SPEX Certiprep, Metuchen, NJ), an X-ray transparent and trace metal free. The Ultralene film had been stretched and adhered to a Delrin ring using 3M white/gray epoxy (3M Scotch-Weld, St. Paul, MN), providing structural support for the 4 μm thick Ultralene film.

The tissue sections were then stained with thioflavin-S, a β-sheet specific dye, to determine the location of the plaques [206, 207]. To do this, dried tissue sections were stained within a few hours of being cut by rehydrating with a 50% ethanol solution. The section was covered in a 0.0125% solution of Thioflavin S in 50% ethanol and allowed to stand for two minutes. The section was then rinsed in 50% ethanol, followed by a second rinse in nanopure water to remove any excess Thioflavin S solution. The sections were allowed to dry and were stored in a desiccator until imaging took place. The green fluorescence from the Thioflavin S stain was visualized using a wide-band blue filter cube (excitation: 465 nm, emission: 550 nm). Thioflavin S was previously shown to not alter iron, copper, or zinc content within tissues that were measured before and after staining [83].

Small FTIRM maps were taken, prior to XFM data collection, in regions on and off the plaques in order to determine the protein content to normalize the XFM data to protein density on the plaque. Normalizing to protein density ensures that the increased protein density within

the plaques is accounted for when quantifying the metal content to avoid over estimating the metal content within the plaques. FTIRM data were acquired at the Continμum IR microscope (Thermo-Nicolet, Madison, WI) at beamline U2B at the National Synchrotron Light Source (NSLS) at Brookhaven National Laboratory (BNL, Upton, NY) with 8 cm^{-1} spectral resolution over the mid infrared region (4000-800 cm^{-1}). A 10 μm aperture was used with a 4 μm step size and 64 scans per point. The relative protein content in the plaques compared to the surrounding healthy tissue was determined by integrating the Amide II peak from 1490 – 1580 cm^{-1} with a linear baseline of 1480 – 1800 cm^{-1}. The height of this peak is directly proportional to the amount of protein in the sample.

The metal concentration within the plaques and the surrounding healthy tissue in the cortex were collected using synchrotron XFM at the Biophysics Collaborative Access Team (BioCAT) beamline 18-ID-D at the Advanced Photon Source, Argonne National Laboratory (Argonne, IL). The energy of the incident X-ray beam was 12 keV using a Si(111) double crystal monochromator. The X-ray beam was focused to 5 by 5 μm spot size using Kirkpatrick-Baez (KB) focusing mirrors. The specimens were placed at a 45° angle with respect to the incident X-ray beam, and the X-ray fluorescence was detected by a Ketek (Munich, Germany) single-element Si-drift detector oriented at a 90° angle from the incident beam. Energy dispersive spectra were collected at every pixel while raster scanning across the specimen at 0.5 seconds per point with a 5 μm step size. The metal concentrations were quantified based on NIST thin-film standards 1832 and 1833 by integrating the peak area for each element of interest in the standards and specimens.

Plaque data were analyzed by creating a region of interest (ROI) both of areas on a plaque and areas off the plaque, using the thioflavin-S visible fluorescence images and the zinc

XFM maps to determine the location of the plaques. Median values were obtained from all the pixels in each ROI for each element. The metal concentration in the plaques was normalized to the total protein content to account for the increased density within the plaques. A percentage difference was calculated between the inside and outside of the plaque regions and compared to previous human and PSAPP mouse data.

XAS data were collected at NSLS beamline X27A using a variable incident X-ray energy, from 50 eV below the iron absorption edge (7112 eV) to 220 eV above the edge, with a channel cut Si(111) monochromator. KB mirrors focused the beam to 10 by 15 μm, and the X-ray fluorescence was detected with a Canberra 13-element germanium array X-ray detector (Meridian, CT) in the same geometry as at 18-ID. Iron X-ray absorption near edge spectroscopy (XANES) data were collected on at least four areas per mouse type, both on and off the plaque, to determine the metal speciation in the plaques and the surrounding tissues. To avoid excess exposure to X-rays and beam damage, two spectra were collected at each point; the beam was then moved 10 μm in the vertical, where two more spectra were collected. This was repeated once more for a total of six XANES spectra (two scans per point) for each area analyzed. To ensure that the beam was maintained within a plaque, only large plaques greater than 30 μm in size were analyzed. XANES standards were acquired at NSLS beamline X3B using a double crystal Si(111) monochromator. Four iron-containing proteins were used: myoglobin and cytochrome-C that contain a porphyrin ring; ferredoxin, an iron-sulfur complex; and ferritin, a common iron storage protein in the brain. These proteins contain different iron binding environments that may be encountered in a biological sample. The samples were maintained at cryogenic temperatures to minimize beam damage for the duration of the experiment. After each spectrum the beam was moved to a new spot on the sample just beyond the width of the beam

(3.25 µm) to further avoid beam damage. The X-ray fluorescence was detected using a Canberra 13-element germanium detector. XANES standards were also collected at beamline X27A on the iron mineral magnetite (Fe_3O_4), which is a possible biomineral found in AD brains [208]. Linear combination fitting was done to determine the possible composition of iron using Athena software (version 0.8.056).

5.2.4 Results and Discussion

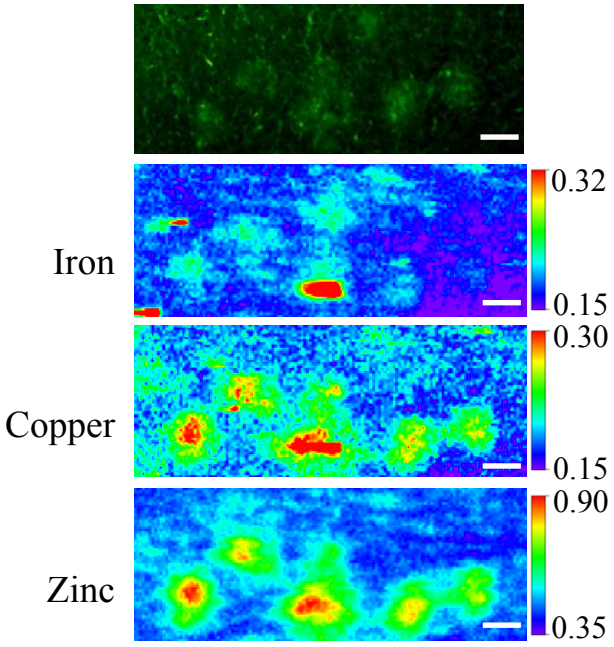

Figure 5.8 Example of plaques from an APPVn/NOS2 KO mouse. Top image shows an epifluorescence image of the thioflavin S stained plaques. The lower three images are maps from XFM data showing the localization of iron, copper and zinc. The relatively small increases in iron are normalized out once the data were normalized to the plaque protein density, but there is increased copper and zinc in these plaques. Concentrations are in mM. Scale bar = 45 µM.

Based on the Amide II band from the FTIRM data, the plaque regions contained on average 1.3 times more protein in the plaques than in the surrounding tissue in the 5xFAD and APPVn/NOS2 mice, and 1.6 times more protein in the PSAPP mice. The plaque regions of the XFM data were

then normalized to these values when calculating the percent difference between the inside and the outside of the plaque.

TABLE 5.1 Protein normalized ratio of iron, copper, and zinc concentrations between inside and outside of a plaque in the cortex of human [83, 195] and AD mouse models PSAPP [83], 5xFAD, and NOS2 KO with the respective percent difference between the metal concentrations in the plaque and the surrounding tissue. In the mouse models the plaque age is listed below the model name.

		Iron	Copper	Zinc
Human	Inside/Outside Plaque (protein Normalized)	2.79 ± 0.24	5.70 ± 0.49	4.42 ± 0.38
	% Difference	+177	+466	+339
PSAPP 32 weeks	Inside/Outside Plaque (protein Normalized)	0.83 ± 0.09	0.79 ± 0.07	1.29 ± 0.12
	% Difference	-17	-22	+29
5xFAD ~48 weeks	Inside/Outside Plaque (protein normalized)	1.04 ± 0.20	1.29 ± 0.23	1.12 ± 0.19
	% Difference	+1.9	+23	+9.6
NOS2 KO 13 weeks	Inside/Outside Plaque (protein normalized)	0.92 ± 0.13	1.34 ± 0.22	1.39 ± 0.23
	% Difference	-9.5	+30	+31

Representative XFM maps are shown in **Figure 5.8** of an area with plaques and healthy tissue in the cortex of an APPVn/NOS2 KO mouse with the thioflavin-S visible fluorescence image and XFM maps of iron, copper, and zinc. **Table 5.1** shows the protein normalized percent difference between inside and outside of the plaque for the two new mouse models 5xFAD and the APPVn/NOS2 KO, in comparison to the PSAPP mouse model and human AD plaques reported previously [83]. The concentration difference between on the plaque and off the plaque for iron, copper and zinc for the 5xFAD mice was 1.9%, 23% and 9.6%, respectively. Whereas

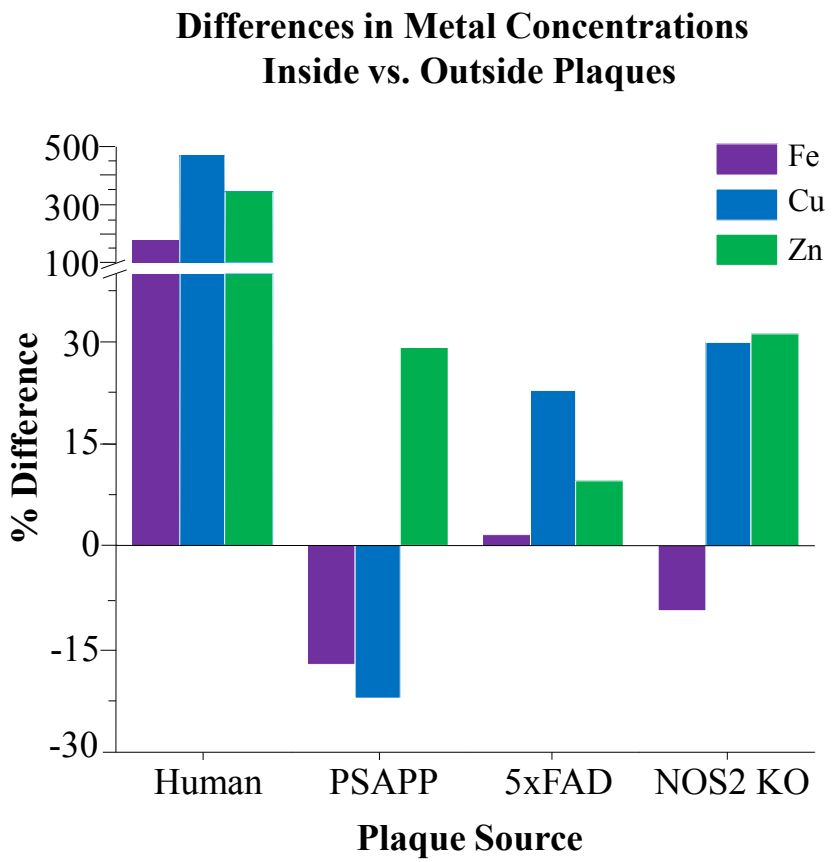

FIGURE 5.9 Bar chart showing the percent difference of iron, copper and zinc inside the plaques compared to the normal surrounding tissue. The human samples showed over 100% increases for all 3 metals [83, 195], but the mouse models did not show the same changes. Percent differences in iron were negative in the PSAPP mice [83] and the APPVn/NOS2 KO mice and only slightly above zero in the 5xFAD mice. Copper was decreased in the PSAPP mice in the plaques but increased in the plaques of 5xFAD and APPVn/NOS2 KO mice. Zinc was consistently elevated in all mouse models but to a much lesser extent than the human plaques.

the APPVn/NOS2 KO mice contained -9.5%, 30% and 31% differences in the iron, copper and zinc, respectively. **Figure 5.9** shows a bar chart of the percent difference values from the human [83, 195], PSAPP [83], 5xFAD, and APPVn/NOS2 KO. XFM data from the plaques of the two mouse models with neurodegeneration, 5xFAD and APPVn/NOS2 KO mice, showed modest increases in metal content upon normalization to protein density. The most significant distinction between the mouse models with neurodegeneration and the PSAPP mice was the increase in copper in the plaques compared to the PSAPP plaques. While the metallation levels in the

plaques of the 5xFAD and APPVn/NOS2 KO mice were not as large as the human plaque data, they are significantly higher than in the PSAPP mice.

The net increase in copper content in the plaques of the 5xFAD and the APPVn/NOS2 KO mice is very intriguing and suggests that the presence of copper could be associated with the neurodegeneration seen in these models, as this is the primary difference between these models and the PSAPP mouse model. Copper and Aβ appear to have a dichotomous relationship. For example, when complexed with copper, Aβ is neurotoxic, but increasing copper levels through diet, drugs or genetic manipulation inhibits Aβ production [209-212]. Thus, it is hypothesized that copper alters the processing of APP and thereby modulating Aβ production [209, 213]. In contrast, copper is known to mediate the degradation of Aβ, which likely occurs through the phosphatedylinositol 3-kinase (PI3K) pathway [214, 215]. Copper is especially hazardous to biological systems because it is redox active, so its improper regulation is detrimental to cells and can lead to the increased oxidative stress found in AD brains [119]. Additionally, *in vitro* studies show that copper is able to bind to Aβ, and it can promote Aβ oligomerization, which is highly cytotoxic [216]. This complex relationship between copper and Aβ suggests that a careful balance of both must be maintained. Production of the amyloidgenic version of Aβ (1-42) is increased in the 5xFAD mouse model [198], but the Aβ production in the APPVn/NOS2 KO should be similar to that of the PSAPP mouse model [217]. However, given the increased copper found in the plaques of the 5xFAD and APPVn/NOS2 KO, it is possible that copper is more affected in these models and could also be associated with neurodegeneration.

We also compared the ages of the 5xFAD mice and the APPVn/NOS2 KO mice and their respective plaque metallation levels. The age of the plaque was determined by the time between

which the mouse model is known to begin developing plaques and when the mouse was sacrificed. Thus, the PSAPP mouse model had plaques that were 32 weeks old, the 5xFAD plaques were ~48 weeks old, and the APPVn/NOS2 KO mouse had 13 week old plaques (**Table 5.1**). The PSAPP mice had plaques that were considerably older than those of the APPVn/NOS2 KO mice, but the PSAPP mice contained less metal, while the younger APPVn/NOS2 KO mice showed more metal. Additionally, in the PSAPP time course study done previously, there was no significant change in metal concentrations in the plaques between mice who were 24, 40, and 56 weeks old, with the exception of zinc, which significantly increased in the last time point [203]. However, the protein density within the plaques did increase between the last two time points. Based on this limited analysis, it does not appear that the age of the plaque leads to an increase in the plaque metal content. Thus, plaques do not appear to accumulate metal over time.

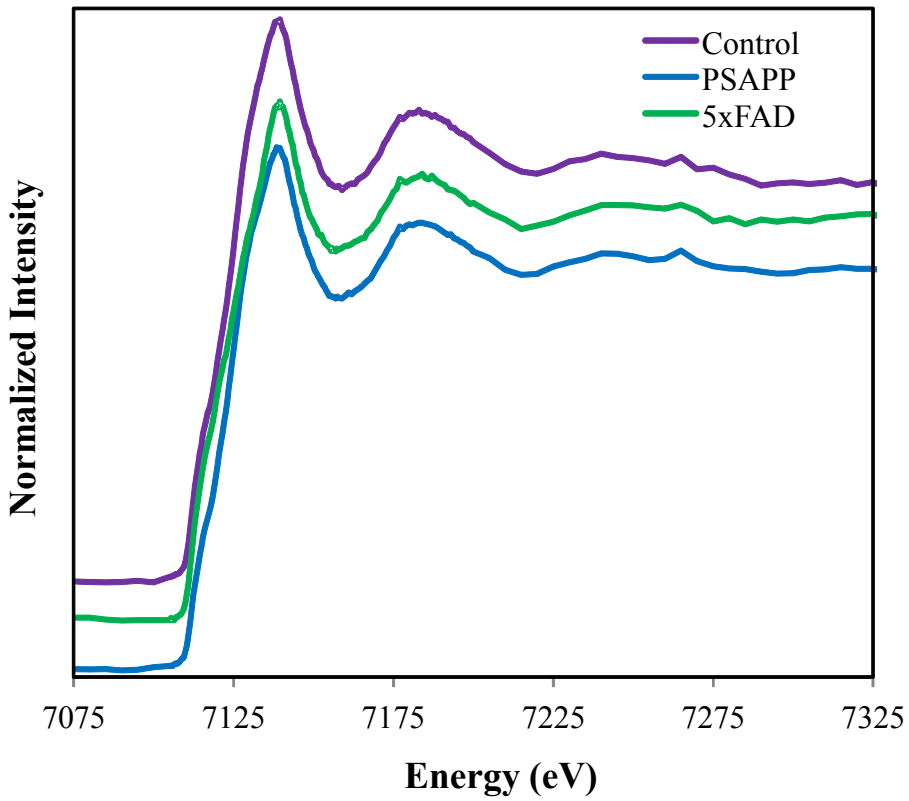

FIGURE 5.10 Iron XANES data from the cortex of control, PSAPP, and 5xFAD mice. No difference was observed between the mouse models or the control mice in the oxidation state of iron or the coordination.

The iron XANES data showed that there is no observable difference between the types of iron found inside versus outside the plaques. In addition, there was no difference in iron speciation between the different mouse models as well as the control mice. This suggests that the type of iron present in the mouse brains is not significantly altered. The iron present in the cortex and the plaques is a combination of iron (II) and iron (III), but is predominantly iron (III). **Figure 5.10** shows representative XANES spectra from on a plaque and surrounding healthy tissue from a 5xFAD mouse and a representative spectrum from a control mouse. Using iron protein and iron mineral standards, there was no clear match that could suggest the form of iron found in the brain specimens (**Figure 5.11)**. These data agree with a previous study, suggesting that iron (III) is the primary species in the mouse models [205] but does not suggest that ferritin is the primary

species. While iron increases in the AD brain, it does not appear to affect the speciation or the form of iron that is present.

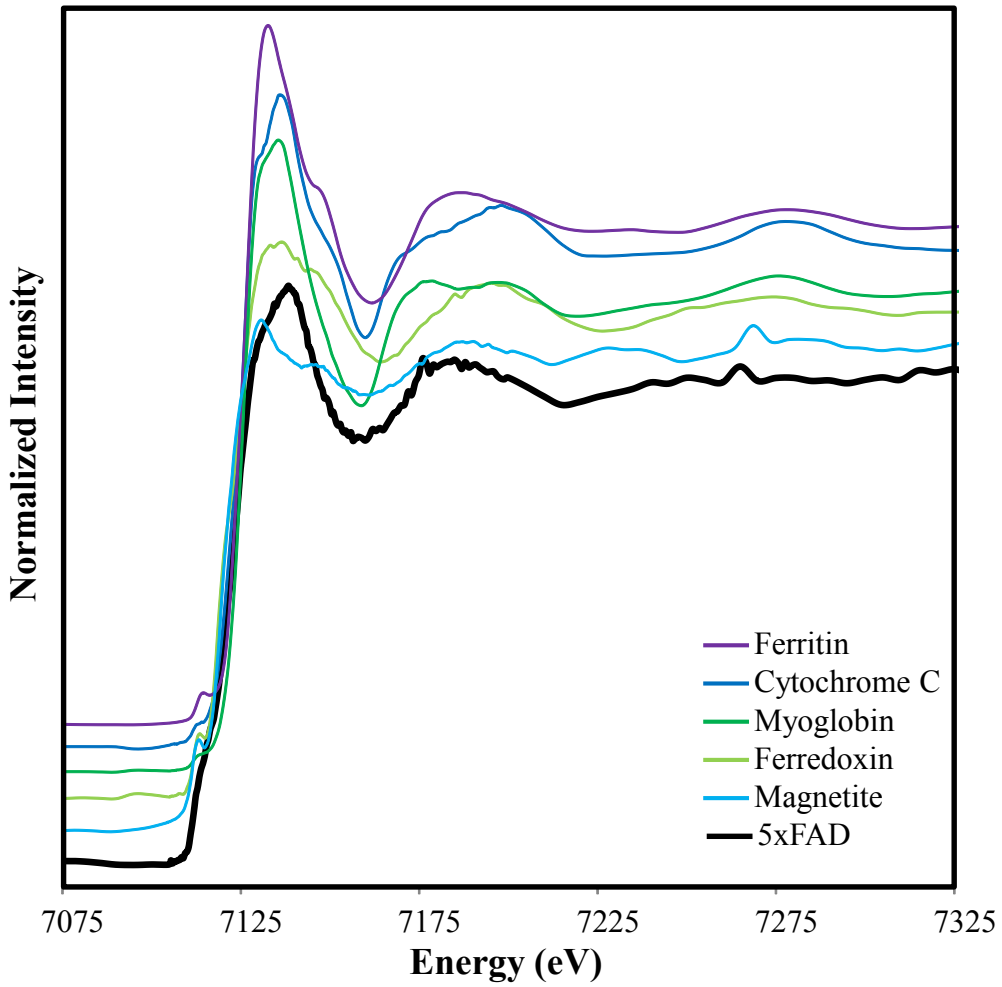

FIGURE 5.11 XANES data from iron standards: ferritin, cytochrome C, myoglobin, ferredoxin, and magenetite with a spectrum from a 5xFAD mouse. Based on linear combination fitting, none of the standard spectra were representative of the specimen spectra.

5.2.5 CONCLUSIONS

These results showed that copper is increased in the plaques in the mouse models that showed neurodegeneration (5xFAD and APPVn/NOS2 KO). The presence of neurodegeneration is the primary difference between these models and the PSAPP mouse model, which did not have

copper enriched plaques. Though the increase in copper is not as significant as in the human models, these data suggest that the presence of copper could contribute to the neurodegeneration that is seen in these models and in AD. In addition, no correlation between the age of the plaques and the metal content was found. While the human plaques are significantly older than mouse plaques, it is unlikely that the plaques accumulate metal after aggregation. Changes in iron homeostasis are well documented in AD, but no difference was seen in the iron oxidation state or coordination of the metal ion between any of the mouse models or control mice. This suggests that the higher levels of iron seen in AD are an increase in the same type of iron found in the healthy brain, which is mostly ferritin [205], rather than a new source of iron. Collectively, these results suggest that a careful balance in metal ions is critical to neuronal survival and restoring metal homeostasis is a potential treatment option for AD in the future.

5.2.6 Future Work

The work presented here was a done on a small scale, with just a few mice per model to test the hypothesis regarding neurodegeneration and the presence of metals in the plaques. In the future, a larger sample size should be used. It would also be useful to test other models with and without neurodegeneration to further confirm these results. Due to the increase in copper inside the plaques of these models, copper XANES would also be a very interesting study in the future. Unfortunately, the low concentration of copper in biological specimens is near the detection limit of this technique, which makes it a very challenging experiment. A beamline with higher flux would be useful, but the increased flux results in additional beam damage to the sample that can alter the electronic environment within the specimen and lead to data that were not representative of the native environment of the specimen. These future experiments could aid in determining

the precise role of metal ions in AD, improve our understanding of the disease, and ultimately lead to better treatment options.

CHAPTER 6

DISCUSSIONS, CONCLUSIONS, AND OUTLOOK

6.1 SUMMARY

Amyotrophic lateral sclerosis (ALS) is a fatal neurodegenerative disease. The precise cause of sporadic ALS cases is unknown. Though the familial cases, such as those linked to copper-zinc superoxide dismutase (SOD1) mutations, provide important insight into the complex mechanisms of the disease. The formation of SOD1 aggregates, alterations in metal homeostasis, and oxidative stress are heavily implicated in the etiology of ALS, but are not well understood [16, 218, 219]. The overwhelming majority of SOD1-ALS research has been performed *in vitro*, but very little has been done *in situ.* To investigate these complex problems we targeted research along three specific aims with *in situ* specimens, using X-ray and infrared imaging techniques. **Specific Aim 1** examined the metallation state of the aggregates in transfected cells with SOD1 mutations, which provided information regarding how the aggregates form. Results showed that aggregates were unmetallated, and support the hypothesis that nascent SOD1 mutations are the predominant form of protein in the aggregates [60, 129]. In addition, cells with SOD1 mutations contained significantly less copper in the cytoplasm than cells with WT SOD1, suggesting a disruption in copper homeostasis in the mutant SOD1 cells. The copper chaperone for SOD1 (CCS) is the primary mechanism to deliver copper to SOD1, and the SOD1 mutations may

preclude the binding of CCS and prevent the delivery of copper [127, 220]. This could contribute to the reduced copper in the cells with mutant SOD1 and the unmetallated aggregates.

To further investigate how metal homeostasis is affected in the spinal cord in ALS, **Specific Aim 2** sought to determine the concentration and localization of metal ions in the spinal cords of transgenic mice with ALS symptoms. As metal ions are critical to the structure and function of SOD1, understanding how they are affected in the disease is necessary to unraveling the mechanisms behind ALS. It was found that soluble SOD1 from wild-type like (WTL) mutations are capable of binding metal, as shown by the soluble SOD1 metallation and by the increase in copper in the gray matter of wild-type (WT) and WTL mouse spinal cords [129]. Additionally, an increase in white matter zinc levels was found in the spinal cords of all the disease-conferring mutations but not in the healthy WT samples, which may be related to glutamate excitotoxicity, found in ALS patients [141].

Metal ions, especially copper and iron, are capable of catalyzing the production of reactive oxygen species (ROS) that can increase oxidative stress [24, 49]. It has also been suggested that mutant SOD1 can react with inappropriate substrates and induce the production of ROS, which can then damage lipids and proteins [52, 221]. Thus, **Specific Aim 3** focused on the degree of oxidative damage found in the spinal cord tissues from ALS mice based on levels of lipid unsaturation and protein carbonyls. The G37R mutation showed the lowest levels of oxidative damage, which could be related to the more protected copper active site associated with this mutation or the reduction in net negative charge, which induces aggregation [158, 163]. Interestingly, this mutation is associated with one of the longest life expectancies among ALS patients [35]. These data suggest that the reduction in oxidative damage could be in part responsible for the increased life span. Collectively, these results show that aggregates were

unmetallated, both copper and zinc metal homeostasis was disrupted, and that the type of SOD1 mutation (WTL or MBR) does not correlate with the degree of oxidative damage.

6.2 DISCUSSION

There are over 160 known SOD1 mutations that can cause ALS [30, 31]. However, they have a large variation in biophysical and chemical properties, making it very difficult to distinguish how these mutations all result in the same disease [16]. Numerous studies have attempted to find a common property that makes SOD1 mutations toxic, but thus far no such property has been elucidated [35]. The differences in metal binding ability and SOD1 activity between WTL and MBR mutations are perhaps the most intriguing discrepancies between SOD1 mutations. One of the goals of this dissertation was to further understand how the different mutation types affect metal homeostasis and oxidative damage in ALS. Thus, we investigated a total of seven SOD1 mutations, including four WTL mutations (A4V, G37R, G93A, and L126Z) and three MBR mutations (H46R/H48Q, H80R, and D125H). All the mutations have been found in ALS patients except the double mutant (H46R/H48Q), which is comprised of two mutations found separately in ALS patients.

All SOD1 mutations form aggregates in the cells, mice, and human patients, but the aggregation propensity varies based on the mutation [35]. Once metallated, WTL SOD1 mutations are often highly stable. However, the unmetalled, apo-SOD1 mutations are significantly less stable than the apo-WT SOD1 for all the mutations, including the WTL mutations [34, 125]. Thus it was hypothesized that the unmetallated form of mutant SOD1 would be more prone to aggregation *in vivo*. The recent findings that detergent insoluble SOD1 extracted from mouse spinal cords was uunmodified and unmetallated strengthens this

hypothesis, and suggests that the nascent SOD1 forms the aggregates before metallation occurs [60, 129]. The results presented here, show the first *in situ* conformation that the SOD1 aggregates within transfected cells are unmetallaed, strongly supporting the hypothesis that the mutant apo-SOD1 accumulates in the aggregates.

Metal ions, such as iron, copper, and zinc, play a role in normal biological processes. However, when metals are improperly regulated metal homeostasis is disrupted, which provides the opportunity for a cascade of detrimental cytotoxic events. In the mouse models copper was elevated in the gray matter of WT and WTL mutations, consistent with the expression of SOD1 and metallation levels of soluble SOD1; but the MBR mutation did not show the same increase in copper. These results are in contrast to the cell culture experiment in which the copper concentration was not dependent on the mutations metal binding ability. The difference between the two models could be related to the amount of soluble SOD1 in cells versus the spinal cord tissue. As the cultured cells quickly form dense aggregates, they likely contain less soluble SOD1 protein than the mouse models. Also, the tissues from the mouse models contain a more complex network of different cell types that have recently been associated with ALS [130, 131]. It is also possible that the copper content was not exclusively in the motor neurons and was present in the other cell types, such as astrocytes. There are currently two known pathways to insert copper into SOD1, a CCS dependent and a CCS independent pathway [128]. Each of the SOD1 mutations studied occurs in the homologous region with CCS that is required for recognition and may be affecting copper binding [127, 220]. The cell culture model is a much simpler system than the mouse model and may be missing an important component to metallate mutant SOD1 without CCS. While CHO-K1 cells and mice should be able to utilize both

pathways [128], the cell network in the spinal cord tissues could be more adept at using the CCS-independent pathway to metallate SOD1 [222, 223].

One of the primary goals of this dissertation was to understand how metallation levels are affected in ALS, by studying them *in situ*. To determine how ALS affects metal homeostasis, spinal cords from transgenic mice expressing mutant human SOD1 were imaged using X-ray fluorescence microscopy (XFM) to evaluate metal localization. Changes were seen in the localization of metal ions in the spinal cord, including increased gray matter copper in the WT and WTL mutations, and increased zinc in the white matter of all SOD1 mutations. Interestingly, ICP-MS studies on the whole spinal cord of mice with the same genotypes did not show a change in copper or zinc concentrations with respect to the type of SOD1 [129]. This highlights the importance of the XFM imaging studies that show copper is significantly increased within the gray matter, though total copper concentrations remained unchanged.

It has been hypothesized that improper metal binding of WTL mutations could result in the catalysis of ROS [61, 224]. Thus it was also expected that mutation type would have an effect on the degree of oxidative stress. However, this was not the result observed in this study. Evidence of increased oxidative damage was found in the WT SOD1 and three of the four SOD1 mutations studied. The oxidative damage found in the WT SOD1 spinal cords suggests that the overexpression of the antioxidant SOD1 does not reduce oxidative damage, but rather increases the amount of oxidative damage relative to non-transgenic (NTG) mice. Indeed, the overexpression of WT SOD1 in mice has shown to produce some ALS-like symptoms in older mice that could be related to the oxidative damage [44, 157, 225]. Both WTL and MBR mutations showed extensive levels of oxidative damage, except for the WTL mutation G37R. Therefore, it does not appear that the type of mutation has a significant effect on the degree of

oxidative damage seen in ALS. Remarkably, the G37R mutation in humans leads to an unusually long life expectancy of about 17 years after the onset of symptoms [35]. It appears to be unlikely that the copper bound to SOD1 is involved in oxidative damage because G37R is a WTL mutation that is capable of binding copper and zinc but shows reduced oxidative damage [129]. One of the most common proposed hypotheses for the toxic gain of function of SOD1 in ALS is its conversion to a pro-oxidant, rather than an anti-oxidant. However, the reduced oxidative damage in the G37R mice argues against SOD1 acting as pro-oxidant and may be linked to the unusually long life expectancy of human patients with this mutation. The results demonstrated here do not correlate with other known properties of the various SOD1 mutations including aggregation propensity, protein half-life, or antioxidant activity levels [35]. Thus, a common property that explains the link between SOD1 mutations and ALS remains elusive.

6.3 Implications for Treatment

ALS remains an untreatable and complex disease. Aside from the deterioration of motor neurons, sporadic variants of ALS (SALS) share many similarities with those of the SOD1-ALS cases. For example, protein aggregation is also found in SALS, though in sporadic cases a variety of proteins other than SOD1 have been found in the aggregates [226, 227]. Increased oxidative stress and metal homeostasis are also associated with SALS [47, 228]. Thus, the results of studies with SOD1-ALS remain relevant to many ALS cases. Currently, the only approved drug treatment of ALS is riluzole, a glutamate inhibitor that reduces the propensity for glutamate excitotoxicity. As riluzole only provides an additional three months to the life expectancy, the efficacy of this drug is very limited for ALS patients [114]. However, the disease-dependent increase in zinc levels seen in the white matter of the spinal cords in transgenic mice

overexpressing SOD1 mutations could be an indication of glutamate excitotoxicity and argues that glutamate inhibitors could be an effective treatment method for ALS patients [141]. Thus, significant improvements to the currently available glutamate inhibitor are necessary.

Numerous other drug treatments have been suggested for ALS, including metal chelation and antioxidant supplementation [5, 50]. Some of these potential treatments have been effective in mouse models, but their transfer to human patients has been less successful [172]. Based on the results presented here, metal ions involved in SOD1 do not directly contribute to the production of oxidative damage or to an accumulation of metal in the aggregates. Therefore, chelation therapy does not appear to be a viable treatment option. Treatment with additional antioxidants, however, may be an acceptable alternative. The G37R mutation that contained the lowest levels of oxidative damage also contains the longest life expectancy of the mutations studied here. Thus, additional antioxidant treatments could be beneficial to compensate for the loss of antioxidant function in SOD1.

6.4 LIMITATIONS

The experiments presented here possess a number of limitations. First, due to the time-consuming data acquisition, the sample size is limited both in the mouse models and in the cell culture experiments. However, the high detection sensitivity and spatial resolution necessary for these experiments required the high brightness of synchrotron source, at which experimental time is limited. Second, the mouse and cell models used here are not fully representative of ALS. For example, the mice still contain their own mouse SOD1 in addition to overexpressing mutant human SOD1. Additionally, cell culture models do no not represent a complete biological system where numerous cell types work in parallel. Given that it has recently been suggested that the

neighboring glial cells contribute to the disease, this could be a significant limitation [130, 131]. The cell culture model of ALS also forced extreme aggregation within the cells that is not completely representative of ALS. It is believed the cells in this model die as a result of cellular pathways being blocked by the numerous intracellular aggregates, but this is not thought to occur in ALS. In addition, these results were not compared to human samples, so it is unclear if the results are directly relatable to human subjects or a result of the genetic manipulation to develop the ALS models.

6.5 Conclusions and Future Work

This dissertation provides an experimental study of a very complex and fatal disease that specifically affects the motor neurons of the spinal cord in humans. Our approach has been to provide a fundamental understanding of the key components in ALS with a systematic approach using cell culture and mouse models of the disease. We have investigated the protein aggregation (**Specific Aim 1**), the role of metals (**Specific Aim 2**), and oxidative stress (**Specific Aim 3**) *in situ* using advanced microspectroscopic imaging techniques, including synchrotron based XFM and FTIR. Our results have identified a critical interplay between metal homeostasis (copper and zinc) but the aggregates were not enriched in metal. In addition oxidative stress was present in all transgenic mice except G37R and thus was not correlated to the type of mutation in SOD1. These results through the use of imaging techniques provided novel insights towards new drug targets and improved treatment options will hopefully lead to a cure for ALS.

The present work inspires a number of potential future experiments to further understand ALS, such as when do the changes in metal homeostasis occur? In the future, a time course study could be done on mice before and after symptoms appear to understand when in the course of the

disease the changes in metal ion localization and concentration begin. Understanding the progression of the disease, especially which pathology occurs first, could help in determining precisely how SOD1 mutations cause ALS. If changes in metal homeostasis occur before the onset of symptoms, it could be used as an early biomarker for the disease. This in turn could lead to treatments beginning sooner and having a greater likelihood of success, as is often found in the mouse models when treatments that begin before the onset of symptoms have been most beneficial [172].

These studies also suggest that some mutations might be less prone to oxidative damage. To study this in more detail, mutations that are similar to G37R could be studied. For example, the H46R (single mutation) and E100K mutations are both associated with longer life expectancies in human patients and have a reduced net charge, similar to G37R [163]. It is hypothesized that these mutations will also have reduced markers for oxidative stress and would further correlate the reduction in oxidative stress with increased life expectancies.

With the recent advancements in live cell IR imaging, the mechanism of SOD1 aggregation can also be probed using IR imaging with live cells to understand the effect of SOD1 mutations on aggregation. Different mutations with various aggregation propensities can be studied to understand which mutations affect the rate of aggregation. This has been done using YFP-SOD1 transfected cells [35], but this was done based on the presence of punctate aggregates. It is possible that IR images, which are highly sensitive to protein secondary structure could see noticeable changes before the development of the very dense aggregates found in the cells.

Additionally, human studies can be done to determine how well the mouse and cell culture models mimic the disease. This would also provide a more direct means of studying

SALS, which affects the majority of patients with this disease. It would be especially interesting to compare SOD1-ALS to SALS to determine if these variants of ALS possess different changes in metal homeostasis. The aggregates (SOD1 or other ALS-associated proteins) in any remaining motor neurons could also be studied in human cases to determine if they are also unmetallated or if the observations seen in the mouse and cell culture models are a result of the SOD1 overexpression.

REFERENCES

1. Ferraiuolo, L., et al., *Molecular pathways of motor neuron injury in amyotrophic lateral sclerosis.* Nature Reviews Neurology, 2011. **7**(11): p. 616-630.

2. Bruijn, L., T. Miller, and D. Cleveland, *Unraveling the mechanisms involved in motor neuron degeneration in ALS.* Annual Review of Neuroscience, 2004. **27**: p. 723-749.

3. McCombe, P.A. and R.D. Henderson, *Effects of gender in amyotrophic lateral sclerosis.* Gender Medicine, 2010. **7**(6): p. 557-570.

4. Ahmed, A. and M.P. Wicklund, *Amyotrophic Lateral Sclerosis: What Role Does Environment Play?* Neurologic clinics, 2011. **29**(3): p. 689-711.

5. de Carvalho, M. and M. Swash, *Amyotrophic lateral sclerosis: an update.* Current Opinion in Neurology, 2011. **24**(5): p. 497-503.

6. Neumann, M., et al., *Ubiquitinated TDP-43 in frontotemporal lobar degeneration and amyotrophic lateral sclerosis.* Science, 2006. **314**(5796): p. 130-133.

7. Sreedharan, J., et al., *TDP-43 mutations in familial and sporadic amyotrophic lateral sclerosis.* Science, 2008. **319**(5870): p. 1668-1672.

8. Mackenzie, I.R.A., et al., *Pathological TDP-43 distinguishes sporadic amyotrophic lateral sclerosis from amyotrophic lateral sclerosis with SOD1 mutations.* Annals of Neurology, 2007. **61**(5): p. 427-434.

9. Vance, C., et al., *Mutations in FUS, an RNA processing protein, cause familial amyotrophic lateral sclerosis type 6.* Science, 2009. **323**(5918): p. 1208-1211.

10. Bäumer, D., et al., *Juvenile ALS with basophilic inclusions is a FUS proteinopathy with FUS mutations.* Neurology, 2010. **75**(7): p. 611-618.

11. Bäumer, D., et al., *The role of RNA processing in the pathogenesis of motor neuron degeneration.* Expert Rev Mol Med, 2010. **12**: p. e21.

12. Lagier-Tourenne, C., M. Polymenidou, and D.W. Cleveland, *TDP-43 and FUS/TLS: emerging roles in RNA processing and neurodegeneration.* Human Molecular Genetics, 2010. **19**(R1): p. R46-R64.

13. Caceci, T. *Nervous Tissue*. [cited 2012 April]; Available from: http://www.vetmed.vt.edu/education/Curriculum/VM8054/Labs/Lab9/lab9.htm.

14. Freinbichler, W., et al., *Highly reactive oxygen species: detection, formation, and possible functions.* Cellular and Molecular Life Sciences, 2011. **68**(12): p. 2067.

15. Rosen, D.R., et al., *Mutations in Cu/Zn superoxide dismutase gene are associated with familial amyotrophic lateral sclerosis.* Nature, 1993. **362**(6415): p. 59-62.

16. Valentine, J., P. Doucette, and S. Potter, *Copper-zinc superoxide dismutase and amyotrophic lateral sclerosis.* Annu. Rev. Biochem., 2005. **72**: p. 563-593.

17. Tainer, J.A., et al., *Determination and analysis of the 2 A-structure of copper, zinc superoxide dismutase.* Journal of Molecular Biology, 1982. **160**(2): p. 181-217.

18. Fridovich, I., *Superoxide dismutases.* Annual review of biochemistry, 1975. **44**(1): p. 147-159.

19. Hoffman, E.K., et al., *Proteasome inhibition enhances the stability of mouse Cu/Zn superoxide dismutase with mutations linked to familial amyotrophic lateral sclerosis.* Journal of the neurological sciences, 1996. **139**(1): p. 15-20.

20. Kurobe, N., et al., *Sensitive enzyme immunoassay for human Cu/Zn superoxide dismutase.* Clinica chimica acta, 1990. **187**(1): p. 11-20.

21. Pryor, W.A. and G.L. Squadrito, *The chemistry of peroxynitrite: a product from the reaction of nitric oxide with superoxide.* American Journal of Physiology-Lung Cellular and Molecular Physiology, 1995. **268**(5): p. L699-L722.

22. Beckman, J.S. and W.H. Koppenol, *Nitric oxide, superoxide, and peroxynitrite: the good, the bad, and ugly.* American Journal of Physiology-cell physiology, 1996. **271**(5): p. C1424-C1437.

23. Flint, D.H., J.F. Tuminello, and M.H. Emptage, *The inactivation of Fe-S cluster containing hydro-lyases by superoxide.* Journal of Biological Chemistry, 1993. **268**(30): p. 22369-22376.

24. Imlay, J.A., *Pathways of oxidative damage.* Annual Reviews in Microbiology, 2003. **57**(1): p. 395-418.

25. D'Autréaux, B. and M.B. Toledano, *ROS as signalling molecules: mechanisms that generate specificity in ROS homeostasis.* Nature Reviews Molecular Cell Biology, 2007. **8**(10): p. 813-824.

26. Gardner, P.R. and I. Fridovich, *Superoxide sensitivity of the Escherichia coli aconitase.* Journal of Biological Chemistry, 1991. **266**(29): p. 19328-19333.

27. Winterbourn, C.C. and D. Metodiewa, *Reactivity of biologically important thiol compounds with superoxide and hydrogen peroxide.* Free Radical Biology and Medicine, 1999. **27**(3-4): p. 322-328.

28. Walling, C., *Fenton's reagent revisited.* Accounts of Chemical Research, 1975. **8**(4): p. 125-131.

29. Rush, J.D., Z. Maskos, and W.H. Koppenol, *Reactions of iron (II) nucleotide complexes with hydrogen peroxide.* FEBS letters, 1990. **261**(1): p. 121-123.

30. Lill, C.M., et al., *Keeping up with genetic discoveries in amyotrophic lateral sclerosis: The ALSoD and ALSGene databases.* Amyotrophic Lateral Sclerosis, 2011. **12**(4): p. 238-249.

31. Abel, O., *ALS Online Genetic Database*, in *ALSOD (3.0)*2012.

32. Shibata, N., et al., *Intense superoxide dismutase-1 immunoreactivity in intracytoplasmic hyaline inclusions of familial amyotrophic lateral sclerosis with posterior column involvement.* Journal of neuropathology and experimental neurology, 1996. **55**(4): p. 481-490.

33. Hayward, L., et al., *Decreased metallation and activity in subsets of mutant superoxide dismutases associated with familial amyotrophic lateral sclerosis.* Journal of Biological Chemistry, 2002. **277**(18): p. 15923-15931.

34. Rodriguez, J.A., et al., *Familial amyotrophic lateral sclerosis-associated mutations decrease the thermal stability of distinctly metallated species of human copper/zinc superoxide dismutase.* Journal of Biological Chemistry, 2002. **277**(18): p. 15932-15937.

35. Prudencio, M., et al., *Variation in aggregation propensities among ALS-associated variants of SOD1: Correlation to human disease.* Human Molecular Genetics, 2009. **18**(17): p. 3217-3226.

36. Lynch, S.M., S.A. Boswell, and W. Colón, *Kinetic Stability of Cu/Zn Superoxide Dismutase Is Dependent on Its Metal Ligands:Implications for ALS†.* Biochemistry, 2004. **43**(51): p. 16525-16531.

37. Radunovic, A. and P.N. Leigh, *Cu/Zn superoxide dismutase gene mutations in amyotrophic lateral sclerosis: correlation between genotype and clinical features.* Journal of Neurology, Neurosurgery & Psychiatry, 1996. **61**(6): p. 565-572.

38. Zu, J.S., et al., *Exon 5 encoded domain is not required for the toxic function of mutant SOD1 but essential for the dismutase activity: identification and characterization of two new SOD1 mutations associated with familial amyotrophic lateral sclerosis.* Neurogenetics, 1997. **1**(1): p. 65-71.

39. Robberecht, W., et al., *Rapid Communication: Cu/Zn Superoxide Dismutase Activity in Familial and Sporadic Amyotrophic Lateral Sclerosis.* Journal of neurochemistry, 1994. **62**(1): p. 384-387.

40. Tsuda, T., et al., *Analysis of the functional effects of a mutation in SOD1 associated with familial amyotrophic lateral sclerosis.* Neuron, 1994. **13**(3): p. 727-736.

41. Wong, P.C., et al., *An adverse property of a familial ALS-linked SOD1 mutation causes motor neuron disease characterized by vacuolar degeneration of mitochondria.* Neuron, 1995. **14**(6): p. 1105-1116.

42. Bowling, A.C., et al., *Superoxide dismutase concentration and activity in familial amyotrophic lateral sclerosis.* Journal of neurochemistry, 1995. **64**(5): p. 2366-2369.

43. Bruijn, L.I., et al., *Aggregation and motor neuron toxicity of an ALS-linked SOD1 mutant independent from wild-type SOD1.* Science, 1998. **281**(5384): p. 1851-1854.

44. Jaarsma, D., et al., *Human Cu/Zn superoxide dismutase (SOD1) overexpression in mice causes mitochondrial vacuolization, axonal degeneration, and premature motoneuron death and accelerates motoneuron disease in mice expressing a familial amyotrophic lateral sclerosis mutant SOD1.* Neurobiology of Disease, 2000. **7**(6): p. 623-643.

45. Furukawa, Y. and T.V. O'Halloran, *Posttranslational modifications in Cu, Zn-superoxide dismutase and mutations associated with amyotrophic lateral sclerosis.* Antioxidants & Redox Signaling, 2006. **8**(5-6): p. 847-867.

46. Fitzmaurice, P.S., et al., *Evidence for DNA damage in amyotrophic lateral sclerosis.* Muscle & nerve, 1996. **19**(6): p. 797-798.

47. Ferrante, R.J., et al., *Evidence of increased oxidative damage in both sporadic and familial amyotrophic lateral sclerosis.* Journal of neurochemistry, 1997. **69**(5): p. 2064-2074.

48. Shibata, N., et al., *Morphological evidence for lipid peroxidation and protein glycoxidation in spinal cords from sporadic amyotrophic lateral sclerosis patients.* Brain research, 2001. **917**(1): p. 97-104.

49. Barber, S.C. and P.J. Shaw, *Oxidative stress in ALS: key role in motor neuron injury and therapeutic target.* Free Radical Biology and Medicine, 2010. **48**(5): p. 629-641.

50. Barnham, K.J., C.L. Masters, and A.I. Bush, *Neurodegenerative diseases and oxidative stress.* Nature Reviews Drug Discovery, 2004. **3**(3): p. 205-214.

51. Yim, M.B., P.B. Chock, and E.R. Stadtman, *Copper, zinc superoxide dismutase catalyzes hydroxyl radical production from hydrogen peroxide.* Proceedings of the National Academy of Sciences, 1990. **87**(13): p. 5006-5010.

52. Yim, M.B., P.B. Chock, and E.R. Stadtman, *Enzyme function of copper, zinc superoxide dismutase as a free radical generator.* Journal of Biological Chemistry, 1993. **268**(6): p. 4099-4105.

53. Estévez, A.G., et al., *Induction of Nitric Oxide--Dependent Apoptosis in Motor Neurons by Zinc-Deficient Superoxide Dismutase.* Science, 1999. **286**(5449): p. 2498-2500.

54. Genova, M.L., et al., *The mitochondrial production of reactive oxygen species in relation to aging and pathology.* Annals of the New York Academy of Sciences, 2004. **1011**(1): p. 86-100.

55. Kikuchi, H., et al. *Spinal cord endoplasmic reticulum stress associated with a microsomal accumulation of mutant superoxide dismutase-1 in an ALS model*. 2006. National Acad Sciences.

56. Saxena, S., E. Cabuy, and P. Caroni, *A role for motoneuron subtype–selective ER stress in disease manifestations of FALS mice.* Nature neuroscience, 2009. **12**(5): p. 627-636.

57. Wang, J., et al., *Progressive aggregation despite chaperone associations of a mutant SOD1-YFP in transgenic mice that develop ALS.* Proceedings of the National Academy of Sciences, 2009. **106**(5): p. 1392-1397.

58. Lee, J.P., et al., *No correlation between aggregates of Cu/Zn superoxide dismutase and cell death in familial amyotrophic lateral sclerosis.* Journal of neurochemistry, 2002. **82**(5): p. 1229-1238.

59. Lino, M.M., C. Schneider, and P. Caroni, *Accumulation of SOD1 mutants in postnatal motoneurons does not cause motoneuron pathology or motoneuron disease.* The Journal of Neuroscience, 2002. **22**(12): p. 4825-4832.

60. Shaw, B.F., et al., *Detergent-insoluble aggregates associated with amyotrophic lateral sclerosis in transgenic mice contain primarily full-length, unmodified superoxide dismutase-1.* Journal of Biological Chemistry, 2008. **283**(13): p. 8340-8350.

61. Wiedau-Pazos, M., et al., *Altered reactivity of superoxide dismutase in familial amyotrophic lateral sclerosis.* Science, 1996. **271**(5248): p. 515-518.

62. Crow, J.P., et al., *Decreased zinc affinity of amyotrophic lateral sclerosis-associated superoxide dismutase mutants leads to enhanced catalysis of tyrosine nitration by peroxynitrite.* Journal of neurochemistry, 1997. **69**(5): p. 1936-1944.

63. Trumbull, K.A. and J.S. Beckman, *A role for copper in the toxicity of zinc-deficient superoxide dismutase to motor neurons in amyotrophic lateral sclerosis.* Antioxidants & Redox Signaling, 2009. **11**(7): p. 1627-1639.

64. Cao, X., et al., *Structures of the G85R variant of SOD1 in familial amyotrophic lateral sclerosis.* Journal of Biological Chemistry, 2008. **283**(23): p. 16169-16177.

65. Liu, H., et al., *Copper (2+) binding to the surface residue cysteine 111 of His46Arg human copper-zinc superoxide dismutase, a familial amyotrophic lateral sclerosis mutant.* Biochemistry, 2000. **39**(28): p. 8125-8132.

66. Watanabe, S., et al., *Increased affinity for copper mediated by cysteine 111 in forms of mutant superoxide dismutase 1 linked to amyotrophic lateral sclerosis.* Free Radical Biology and Medicine, 2007. **42**(10): p. 1534-1542.

67. Son, M., et al., *Overexpression of CCS in G93A-SOD1 mice leads to accelerated neurological deficits with severe mitochondrial pathology.* Proceedings of the National Academy of Sciences, 2007. **104**(14): p. 6072-6077.

68. Elliott, J.L., *Zinc and copper in the pathogenesis of amyotrophic lateral sclerosis.* Progress in Neuro-Psychopharmacology and Biological Psychiatry, 2001. **25**(6): p. 1169-1185.

69. Smith, A.P. and N.M. Lee, *Role of zinc in ALS.* Amyotrophic Lateral Sclerosis, 2007. **8**(3): p. 131-143.

70. Dineley, K.E., T.V. Votyakova, and I.J. Reynolds, *Zinc inhibition of cellular energy production: implications for mitochondria and neurodegeneration.* Journal of neurochemistry, 2003. **85**(3): p. 563-570.

71. Magrané, J. and G. Manfredi, *Mitochondrial function, morphology, and axonal transport in amyotrophic lateral sclerosis.* Antioxidants & Redox Signaling, 2009. **11**(7): p. 1615-1626.

72. Persechini, A., K. McMillan, and B.S.S. Masters, *Inhibition of nitric oxide synthase activity by Zn2+ ion.* Biochemistry, 1995. **34**(46): p. 15091-15095.

73. Maragakis, N.J., M. Dykes-Hoberg, and J.D. Rothstein, *Altered expression of the glutamate transporter EAAT2b in neurological disease.* Annals of Neurology, 2004. **55**(4): p. 469-477.

74. Rakhit, R., et al., *Oxidation-induced misfolding and aggregation of superoxide dismutase and its implications for amyotrophic lateral sclerosis.* Journal of Biological Chemistry, 2002. **277**(49): p. 47551-47556.

75. Curtain, C.C., et al., *Alzheimer's disease amyloid-β binds copper and zinc to generate an allosterically ordered membrane-penetrating structure containing superoxide dismutase-like subunits.* Journal of Biological Chemistry, 2001. **276**(23): p. 20466-20473.

76. Ide-Ektessabi, A., *Applications of Synchrotron Radiation: Micro Beams in Cell Micro Biology and Medicine*2007: Springer Verlag.

77. Vogt, S. *X-Ray Microscopy and Imaging: X-ray Fluorescence Mapping*. 2007 [cited 2012 April]; Available from:

http://www.aps.anl.gov/Xray_Science_Division/Xray_Microscopy_and_Imaging/Science_and_Research/Techniques/Xray_Fluorescence_Mapping/index.html.

78. Janssens, J., *X-ray based methods of analysis*, in *Non-destructive microanalysis of cultural heritage materials*, C. Barceló, Editor 2005, Elsevier: Amsterdam, The Netherlands.

79. Skoog, D.A., F.J. Holler, and S.R. Crouch, *An Introduction to Infrared Spectrometry*, in *Principles of Instrumental Analysis*2007, Thomson Brooks/Cole: Belmont, CA.

80. Matthäus, C., et al., *Infrared and Raman microscopy in cell biology.* Methods in cell biology, 2008. **89**: p. 275-308.

81. Miller, L.M. and P. Dumas, *From structure to cellular mechanism with infrared microspectroscopy.* Current Opinion in Structural Biology, 2010. **20**(5): p. 649-656.

82. Miller, L.M. and P. Dumas, *Chemical imaging of biological tissue with synchrotron infrared light.* Biochimica et Biophysica Acta (BBA) - Biomembranes, 2006. **1758**(7): p. 846-857.

83. Leskovjan, A.C., A. Lanzirotti, and L.M. Miller, *Amyloid plaques in PSAPP mice bind less metal than plaques in human Alzheimer's disease.* NeuroImage, 2009. **47**(4): p. 1215-1220.

84. Byler, D.M. and H. Susi, *Examination of the secondary structure of proteins by deconvolved FTIR spectra.* Biopolymers, 1986. **25**(3): p. 469-487.

85. Goormaghtigh, E., J.M. Ruysschaert, and V. Raussens, *Evaluation of the information content in infrared spectra for protein secondary structure determination.* Biophysical journal, 2006. **90**(8): p. 2946-2957.

86. Sills, R.H., D.J. Moore, and R. Mendelsohn, *Erythrocyte Peroxidation: Quantitation by Fourier Transform Infrared Spectroscopy.* Analytical Biochemistry, 1994. **218**(1): p. 118-123.

87. Leskovjan, A.C., A. Kretlow, and L.M. Miller, *Fourier Transform Infrared Imaging Showing Reduced Unsaturated Lipid Content in the Hippocampus of a Mouse Model of Alzheimer's Disease.* Analytical Chemistry, 2010. **82**(7): p. 2711-2716.

88. Bruijn, L.I., et al., *Elevated free nitrotyrosine levels, but not protein-bound nitrotyrosine or hydroxyl radicals, throughout amyotrophic lateral sclerosis (ALS)-like disease implicate tyrosine nitration as an aberrant in vivo property of one familial ALS-linked superoxide dismutase 1 mutant.* Proceedings of the National Academy of Sciences, 1997. **94**(14): p. 7606-7611.

89. Reaume, A.G., et al., *Motor neurons in Cu/Zn superoxide dismutase-deficient mice develop normally but exhibit enhanced cell death after axonal injury.* Nature Genetics, 1996. **13**(1): p. 43-47.

90. Ripps, M.E., et al., *Transgenic mice expressing an altered murine superoxide dismutase gene provide an animal model of amyotrophic lateral sclerosis.* Proceedings of the National Academy of Sciences, 1995. **92**(3): p. 689-693.

91. Wils, H., et al., *TDP-43 transgenic mice develop spastic paralysis and neuronal inclusions characteristic of ALS and frontotemporal lobar degeneration.* Proceedings of the National Academy of Sciences, 2010. **107**(8): p. 3858-3863.

92. Wegorzewska, I., et al., *TDP-43 mutant transgenic mice develop features of ALS and frontotemporal lobar degeneration.* Proceedings of the National Academy of Sciences, 2009. **106**(44): p. 18809-18814.

93. Stallings, N.R., et al., *Generation and characterization of wild-type and mutant TDP-43 transgenic mice*. Abstract Book Society for Neuroscience2009: Society for Neuroscience.

94. Swarup, V. and J.P. Julien, *ALS pathogenesis: Recent insights from genetics and mouse models.* Progress in Neuro-Psychopharmacology and Biological Psychiatry, 2011. **35**(2): p. 363-369.

95. Cote, F., J.F. Collard, and J.P. Julien, *Progressive neuronopathy in transgenic mice expressing the human neurofilament heavy gene: a mouse model of amyotrophic lateral sclerosis.* Cell, 1993. **73**(1): p. 35-35.

96. Lee, M.K., J.R. Marszalek, and D.W. Cleveland, *A mutant neurofilament subunit causes massive, selective motor neuron death: implications for the pathogenesis of human motor neuron disease.* Neuron, 1994. **13**(4): p. 975-988.

97. Millecamps, S., et al., *Defective axonal transport of neurofilament proteins in neurons overexpressing peripherin.* Journal of neurochemistry, 2006. **98**(3): p. 926-938.

98. LaMonte, B.H., et al., *Disruption of dynein/dynactin inhibits axonal transport in motor neurons causing late-onset progressive degeneration.* Neuron, 2002. **34**(5): p. 715-727.

99. Hafezparast, M., et al., *Mutations in dynein link motor neuron degeneration to defects in retrograde transport.* Science, 2003. **300**(5620): p. 808-812.

100. Laird, F.M., et al., *Motor neuron disease occurring in a mutant dynactin mouse model is characterized by defects in vesicular trafficking.* The Journal of Neuroscience, 2008. **28**(9): p. 1997-2005.

101. Eymard-Pierre, E., et al., *Infantile-onset ascending hereditary spastic paralysis is associated with mutations in the alsin gene.* The American Journal of Human Genetics, 2002. **71**(3): p. 518-527.

102. Yang, Y., et al., *The gene encoding alsin, a protein with three guanine-nucleotide exchange factor domains, is mutated in a form of recessive amyotrophic lateral sclerosis.* Nature Genetics, 2001. **29**(2): p. 160-165.

103. Hadano, S., et al., *Mice deficient in the Rab5 guanine nucleotide exchange factor ALS2/alsin exhibit age-dependent neurological deficits and altered endosome trafficking.* Human Molecular Genetics, 2006. **15**(2): p. 233-250.

104. Gurney, M.E., et al., *Motor neuron degeneration in mice that express a human Cu,Zn superoxide dismutase mutation.* Science, 1994. **264**(5166): p. 1772-1775.

105. Wang, J., et al., *Fibrillar inclusions and motor neuron degeneration in transgenic mice expressing superoxide dismutase 1 with a disrupted copper-binding site.* Neurobiology of Disease, 2002. **10**(2): p. 128-138.

106. Silani, V., et al., *Motor neurones in culture as a model to study ALS.* Journal of Neurology, 2000. **247**: p. 28-36.

107. Menzies, F.M., et al., *Mitochondrial dysfunction in a cell culture model of familial amyotrophic lateral sclerosis.* Brain, 2002. **125**(7): p. 1522-1533.

108. Dimos, J.T., et al., *Induced pluripotent stem cells generated from patients with ALS can be differentiated into motor neurons.* Science, 2008. **321**(5893): p. 1218-1221.

109. Prudencio, M. and D.R. Borchelt, *Superoxide dismutase 1 encoding mutations linked to ALS adopts a spectrum of misfolded states.* Molecular Neurodegeneration, 2011. **6**(1): p. 1-19.

110. Barnham, K., C. Masters, and A. Bush, *Neurodegenerative diseases and oxidative stress.* Nature Reviews Drug Discovery, 2004. **3**: p. 205-214.

111. Ogawa, Y., et al., *Stability of mutant superoxide dismutase-1 associated with familial amyotrophic lateral sclerosis determines the manner of copper release and induction of thioredoxin in erythrocytes.* Biochemical and biophysical research communications, 1997. **241**(2): p. 251-257.

112. Bergomi, M., et al., *Environmental exposure to trace elements and risk of amyotrophic lateral sclerosis: a population-based case-control study.* Environmental research, 2002. **89**(2): p. 116-123.

113. Andrus, P., et al., *Protein oxidative damage in a transgenic mouse model of familial amyotrophic lateral sclerosis.* Journal of neurochemistry, 1998. **71**(5): p. 2041-2048.

114. Miller, R.G., et al., *Riluzole for amyotrophic lateral sclerosis (ALS)/motor neuron disease (MND).* Cochrane Database Syst Rev, 2007. **1**(1).

115. Ellerby, L.M., et al., *Copper-zinc superoxide dismutase: Why not pH-dependent?* Journal of the American Chemical Society, 1996. **118**(28): p. 6556-6561.

116. Deng, H.X., et al., *Amyotrophic lateral sclerosis and structural defects in Cu, Zn superoxide dismutase.* Science, 1993. **261**(5124): p. 1047-1051.

117. Borchelt, D.R., et al., *Superoxide dismutase 1 with mutations linked to familial amyotrophic lateral sclerosis possesses significant activity.* Proceedings of the National Academy of Sciences, 1994. **91**(17): p. 8292-8296.

118. Seetharaman, S.V., et al., *Disrupted zinc-binding sites in structures of pathogenic SOD1 variants D124V and H80R.* Biochemistry, 2010. **49**(27): p. 5714-5725.

119. Maynard, C.J., et al., *Metals and amyloid in Alzheimer's disease.* International journal of experimental pathology, 2005. **86**(3): p. 147-159.

120. Bush, A., *The metallobiology of Alzheimer's disease.* TRENDS in Neurosciences, 2003. **26**(4): p. 207-214.

121. Vonk, W. and L. Klomp, *Role of transition metals in the pathogenesis of amyotrophic lateral sclerosis.* Biochemical Society Transactions, 2008. **36**: p. 1322-1328.

122. Lutsenko, S., A. Bhattacharjee, and A.L. Hubbard, *Copper handling machinery of the brain.* Metallomics, 2010. **2**(9): p. 596-608.

123. Huang, X., et al., *Zinc-induced Alzheimer's Aβ1–40 aggregation is mediated by conformational factors.* Journal of Biological Chemistry, 1997. **272**(42): p. 26464-26470.

124. Bertoncini, C.W., et al., *Release of long-range tertiary interactions potentiates aggregation of natively unstructured α-synuclein.* Proceedings of the National Academy of Sciences of the United States of America, 2005. **102**(5): p. 1430-1435.

125. Rodriguez, J.A., et al., *Destabilization of apoprotein is insufficient to explain Cu, Zn-superoxide dismutase-linked ALS pathogenesis.* Proceedings of the National Academy of Sciences of the United States of America, 2005. **102**(30): p. 10516-10521.

126. Karch, C.M. and D.R. Borchelt, *A limited role for disulfide cross-linking in the aggregation of mutant SOD1 linked to familial amyotrophic lateral sclerosis.* Journal of Biological Chemistry, 2008. **283**(20): p. 13528-13537.

127. Schmidt, P.J., et al., *Multiple protein domains contribute to the action of the copper chaperone for superoxide dismutase.* Journal of Biological Chemistry, 1999. **274**(34): p. 23719-23725.

128. Leitch, J.M., P.J. Yick, and V.C. Culotta, *The right to choose: multiple pathways for activating copper, zinc superoxide dismutase.* Journal of Biological Chemistry, 2009. **284**(37): p. 24679-24683.

129. Lelie, H.L., et al., *Copper and Zinc Metallation Status of Copper-Zinc Superoxide Dismutase from Amyotrophic Lateral Sclerosis Transgenic Mice.* Journal of Biological Chemistry, 2011. **286**(4): p. 2795-2806.

130. Julien, J.P., *ALS: astrocytes move in as deadly neighbors.* Nature neuroscience, 2007. **10**(5): p. 535-537.

131. Ilieva, H., M. Polymenidou, and D.W. Cleveland, *Non–cell autonomous toxicity in neurodegenerative disorders: ALS and beyond.* The Journal of cell biology, 2009. **187**(6): p. 761-772.

132. Gaggelli, E., et al., *Copper homeostasis and neurodegenerative disorders (Alzheimer's, prion, and Parkinson's diseases and amyotrophic lateral sclerosis).* Chemical reviews, 2006. **106**(6): p. 1995-2044.

133. Selkoe, D.J., *Alzheimer's disease: genes, proteins, and therapy.* Physiological reviews, 2001. **81**(2): p. 741-766.

134. Lotharius, J. and P. Brundin, *Pathogenesis of Parkinson's disease: dopamine, vesicles and alpha-synuclein.* Nature Reviews Neuroscience, 2002. **3**(12): p. 932-942.

135. Popescu, B.F.G., et al., *Iron, copper, and zinc distribution of the cerebellum.* The Cerebellum, 2009. **8**(2): p. 74-79.

136. Pardo, C.A., et al., *Superoxide dismutase is an abundant component in cell bodies, dendrites, and axons of motor neurons and in a subset of other neurons.* Proceedings of the National Academy of Sciences, 1995. **92**(4): p. 954-954.

137. Jeong, S.Y., et al., *Dysregulation of iron homeostasis in the CNS contributes to disease progression in a mouse model of amyotrophic lateral sclerosis.* The Journal of Neuroscience, 2009. **29**(3): p. 610-619.

138. Winkler, D.D., et al., *Structural and Biophysical Properties of the Pathogenic SOD1 Variant H46R/H48Q†.* Biochemistry, 2009. **48**(15): p. 3436-3447.

139. Rodriguez, J.A., *Thermal stability, catalytic activity and spectroscopic properties of amyotrophic lateral sclerosis-associated copper-zinc superoxide dismutases*, in *Chemistry and Biochemistry*2004, University of California Los Angeles. p. 244.

140. Doucette, P.A., *Biophysical studies of human copper-zinc superoxide dismutase muants associated with the neurodegenerative disease amyotrophic lateral sclerosis*, in *Chemistry and Biochemistry*2004, University of California Los Angeles. p. 249.

141. Rothstein, J.D., *Excitotoxicity and neurodegeneration in amyotrophic lateral sclerosis.* Clinical neuroscience (New York, NY), 1996. **3**(6): p. 348-359.

142. Tomik, B., et al., *Implementation of X-ray Fluorescence Microscopy for Investigation of Elemental Abnormalities in Amyotrophic Lateral Sclerosis.* Neurochemical Research, 2006. **31**(3): p. 321-331.

143. Sillevis Smitt, P.A.E., et al., *Metallothionein immunoreactivity is increased in the spinal cord of patients with amyotrophic lateral sclerosis.* Neuroscience letters, 1992. **144**(1-2): p. 107-110.

144. Sillevis Smitt, P.A.E., et al., *Metallothionein in amyotrophic lateral sclerosis.* Neurosignals, 1994. **3**(4): p. 193-197.

145. Kim, J., et al., *Accumulation of labile zinc in neurons and astrocytes in the spinal cords of G93A SOD-1 transgenic mice.* Neurobiology of Disease, 2009. **34**(2): p. 221-229.

146. Gong, Y.H. and J.L. Elliott, *Metallothionein expression is altered in a transgenic murine model of familial amyotrophic lateral sclerosis.* Experimental neurology, 2000. **162**(1): p. 27-36.

147. Nagano, S., et al., *Reduction of metallothioneins promotes the disease expression of familial amyotrophic lateral sclerosis mice in a dose-dependent manner.* European Journal of Neuroscience, 2001. **13**(7): p. 1363-1370.

148. Puttaparthi, K., et al., *Disease progression in a transgenic model of familial amyotrophic lateral sclerosis is dependent on both neuronal and non-neuronal zinc binding proteins.* The Journal of neuroscience, 2002. **22**(20): p. 8790-8796.

149. Goto, J.J., et al., *Loss of in vitro metal ion binding specificity in mutant copper-zinc superoxide dismutases associated with familial amyotrophic lateral sclerosis.* Journal of Biological Chemistry, 2000. **275**(2): p. 1007-1014.

150. Beal, M.F., et al., *Increased 3 nitrotyrosine in both sporadic and familial amyotrophic lateral sclerosis.* Annals of Neurology, 1997. **42**(4): p. 644-654.

151. Smith, R.G., et al., *Presence of 4-hydroxynonenal in cerebrospinal fluid of patients with sporadic amyotrophic lateral sclerosis.* Annals of Neurology, 1998. **44**(4): p. 696-699.

152. Simpson, E.P., et al., *Increased lipid peroxidation in sera of ALS patients.* Neurology, 2004. **62**(10): p. 1758-1765.

153. Dalle-Donne, I., et al., *Protein carbonyl groups as biomarkers of oxidative stress.* Clinica Chimica Acta, 2003. **329**(1-2): p. 23-38.

154. Lelie, H.L., *Elucidating the role of mutant human copper-zinc superoxide dismutase aggregates and metal ions in a mouse model of amyotrophic lateral sclerosis*, in *Chemistry and Biochemistry*2010, University of Calfiornia Los Angeles. p. 220.

155. Lee, M.H., et al., *Effect of overexpression of wild-type and mutant Cu/Zn-superoxide dismutases on oxidative stress and cell death induced by hydrogen peroxide, 4-hydroxynonenal or serum deprivation: potentiation of injury by ALS-related mutant superoxide dismutases and protection by Bcl-2.* Journal of neurochemistry, 2001. **78**(2): p. 209-220.

156. Joyce, P.I., et al., *SOD1 and TDP-43 animal models of amyotrophic lateral sclerosis: recent advances in understanding disease toward the development of clinical treatments.* Mammalian Genome, 2011: p. 1-29.

157. Dal Canto, M.C. and M.E. Gurney, *Neuropathological changes in two lines of mice carrying a transgene for mutant human Cu, Zn SOD, and in mice overexpressing wild type human SOD: a model of familial amyotrophic lateral sclerosis (FALS).* Brain research, 1995. **676**(1): p. 25-40.

158. Eisenberg, D., et al., *Subunit asymmetry in the three-dimensional structure of a human CuZnSOD mutant found in familial amyotrophic lateral sclerosis.* Protein Science, 1998. **7**(3): p. 545-555.

159. Carrì, M.T., et al., *Impaired copper binding by the H46R mutant of human Cu, Zn superoxide dismutase, involved in amyotrophic lateral sclerosis.* FEBS letters, 1994. **356**(2-3): p. 314-316.

160. Beckman, J.S., et al., *ALS, SOD and peroxynitrite.* Nature, 1993. **364**(6438): p. 584-584.

161. Museth, A.K., et al., *The ALS-Associated Mutation G93A in Human Copper-Zinc Superoxide Dismutase Selectively Destabilizes the Remote Metal Binding Region.* Biochemistry, 2009. **48**(37): p. 8817-8829.

162. Seetharaman, S., et al., *Immature Copper-Zinc Superoxide Dismutase and Familial Amyotrophic Lateral Sclerosis.* Experimental Biology and Medicine, 2009. **234**(10): p. 1140-1154.

163. Shaw, B.F., et al., *Taking Charge of Proteins:: From Neurodegeneration to Industrial Biotechnology.* Advances in Protein Chemistry and Structural Biology, 2010. **79**: p. 127-164.

164. Shaw, B. and J. Valentine, *How do ALS-associated mutations in superoxide dismutase 1 promote aggregation of the protein?* Trends in Biochemical Sciences, 2007. **32**(2): p. 78-85.

165. Wang, Q., et al., *Protein aggregation and protein instability govern familial amyotrophic lateral sclerosis patient survival.* PLoS biology, 2008. **6**(7): p. e170.

166. Bensimon, G., L. Lacomblez, and V. Meininger, *A controlled trial of riluzole in amyotrophic lateral sclerosis.* New England Journal of Medicine, 1994. **330**(9): p. 585-591.

167. Koh, J.Y., et al., *Antioxidative and proapoptotic effects of riluzole on cultured cortical neurons.* Journal of neurochemistry, 1999. **72**(2): p. 716-723.

168. Gurney, M.E., et al., *Benefit of vitamin E, riluzole, and gababapentin in a transgenic model of familial amyotrophic lateral sclerosis.* Annals of Neurology, 1996. **39**(2): p. 147-157.

169. Desnuelle, C., et al., *A double-blind, placebo-controlled randomized clinical trial of α-tocopherol (vitamin E) in the treatment of amyotrophic lateral sclerosis.* Amyotrophic Lateral Sclerosis, 2001. **2**(1): p. 9-18.

170. Graf, M., et al., *High dose vitamin E therapy in amyotrophic lateral sclerosis as add-on therapy to riluzole: results of a placebo-controlled double-blind study.* Journal of Neural Transmission, 2005. **112**(5): p. 649-660.

171. Rothstein, J.D., *Of mice and men: reconciling preclinical ALS mouse studies and human clinical trials.* Annals of Neurology, 2003. **53**(4): p. 423-426.

172. Benatar, M., *Lost in translation: treatment trials in the SOD1 mouse and in human ALS.* Neurobiology of Disease, 2007. **26**(1): p. 1-13.

173. Zobov, N.F., et al., *Vibration-rotation levels of water beyond the Born-Oppenheimer approximation.* Chemical physics letters, 1996. **260**(3): p. 381-387.

174. Millo, A., Y. Raichlin, and A. Katzir, *Mid-infrared Fiber-Optic Attenuated Total Reflection Spectroscopy of the Solid–Liquid Phase Transition of Water.* Applied spectroscopy, 2005. **59**(4): p. 460-466.

175. Nasse, M.J., et al., *Demountable Liquid/Flow Cell for in Vivo Infrared Microspectroscopy of Biological Specimens.* Applied spectroscopy, 2009. **63**(10): p. 1181-1186.

176. Birarda, G., et al., *Fabrication of a microfluidic platform for investigating dynamic biochemical processes in living samples by FTIR microspectroscopy.* Microelectronic engineering, 2010. **87**(5-8): p. 806-809.

177. Birarda, G., et al., *Infrared microspectroscopy of biochemical response of living cells in microfabricated devices.* Vibrational Spectroscopy, 2010. **53**(1): p. 6-11.

178. Holman, H.Y.N., et al., *Real-time chemical imaging of bacterial activity in biofilms using open-channel microfluidics and synchrotron FTIR spectromicroscopy.* Analytical Chemistry, 2009. **81**(20): p. 8564-8570.

179. Tobin, M.J., et al., *FTIR spectroscopy of single live cells in aqueous media by synchrotron IR microscopy using microfabricated sample holders.* Vibrational Spectroscopy, 2010. **53**(1): p. 34-38.

180. Kuimova, M.K., K.L. Chan, and S.G. Kazarian, *Chemical imaging of live cancer cells in the natural aqueous environment.* Applied spectroscopy, 2009. **63**(2): p. 164-171.

181. Yang, W., et al., *In situ evaluation of breast cancer cell growth with 3D ATR-FTIR spectroscopy.* Vibrational Spectroscopy, 2009. **49**(1): p. 64-67.

182. Mariangela, C.-G., et al., *Experimental ATR device for real-time FTIR imaging of living cells using brilliant synchrotron radiation sources.* Biotechnology Advances, 2012. **In press**(0).

183. Holman, H.Y.N., M.C. Martin, and W.R. McKinney, *Tracking chemical changes in a live cell: Biomedical applications of SR-FTIR spectromicroscopy.* Spectroscopy-An International Journal, 2003. **17**(2-3): p. 139-160.

184. Marcsisin, E.J.S., et al., *Infrared microspectroscopy of live cells in aqueous media.* Analyst, 2010. **135**(12): p. 3227-3232.

185. Marcsisin, E.J., *Infrared Spectroscopy to Monitor Drug Response of Individual Live Cells*, in *Chemistry*2011, Northeastern University. p. 182.

186. Sommer, A., et al., *Attenuated total internal reflection infrared mapping microspectroscopy using an imaging microscope.* Applied spectroscopy, 2001. **55**(3): p. 252-256.

187. Venyaminov, S.Y. and F.G. Prendergast, *Water (H2O and D2O) Molar Absorptivity in the 1000-4000 cm^{-1} Range and Quantitative Infrared Spectroscopy of Aqueous Solutions.* Analytical Biochemistry, 1997. **248**(2): p. 234-245.

188. Griffiths, P.R. and J.A. De Haseth, *Fourier transform infrared spectrometry*. Vol. 171. 2007: Wiley-Interscience.

189. Gardette, J., B. Mailhot, and J. Lemaire, *Photooxidation mechanisms of styrenic polymers.* Polymer degradation and stability, 1995. **48**(3): p. 457-470.

190. Holman, H.Y.N., et al., *Synchrotron IR spectromicroscopy: chemistry of living cells.* Analytical Chemistry, 2010. **82**(21): p. 8757-8765.

191. Mattson, M.P., *Pathways towards and away from Alzheimer's disease.* Nature, 2004. **430**(7000): p. 631-639.

192. Alzheimer, A., *A new disease of the cortex (Ger).* Allg Z Psychiatr, 1907. **64**: p. 146-148.

193. Mattson, M.P., *Cellular actions of beta-amyloid precursor protein and its soluble and fibrillogenic derivatives.* Physiological reviews, 1997. **77**(4): p. 1081-1132.

194. Lovell, M.A., et al., *Copper, iron and zinc in Alzheimer's disease senile plaques.* Journal of the neurological sciences, 1998. **158**(1): p. 47-52.

195. Miller, L., et al., *Synchrotron-based infrared and X-ray imaging shows focalized accumulation of Cu and Zn co-localized with β-amyloid deposits in Alzheimer's disease.* Journal of Structural Biology, 2006. **155**(1): p. 30-37.

196. Jankowsky, J.L., et al., *Co-expression of multiple transgenes in mouse CNS: a comparison of strategies.* Biomolecular engineering, 2001. **17**(6): p. 157-165.

197. Garcia-Alloza, M., et al., *Characterization of amyloid deposition in the APPswe/PS1dE9 mouse model of Alzheimer disease.* Neurobiology of Disease, 2006. **24**(3): p. 516-524.

198. Oakley, H., et al., *Intraneuronal β-amyloid aggregates, neurodegeneration, and neuron loss in transgenic mice with five familial Alzheimer's disease mutations: potential factors in amyloid plaque formation.* The Journal of Neuroscience, 2006. **26**(40): p. 10129-10140.

199. Colton, C.A., et al., *The effects of NOS2 gene deletion on mice expressing mutated human AßPP.* Journal of Alzheimer's Disease, 2008. **15**(4): p. 571-587.

200. Haacke, E.M., et al., *Imaging iron stores in the brain using magnetic resonance imaging.* Magnetic resonance imaging, 2005. **23**(1): p. 1-25.

201. Brass, S.D., et al., *Magnetic resonance imaging of iron deposition in neurological disorders.* Topics in Magnetic Resonance Imaging, 2006. **17**(1): p. 31-31.

202. Stankiewicz, J., et al., *Iron in chronic brain disorders: imaging and neurotherapeutic implications.* Neurotherapeutics, 2007. **4**(3): p. 371-386.

203. Leskovjan, A.C., et al., *Increased brain iron coincides with early plaque formation in a mouse model of Alzheimer's disease.* NeuroImage, 2011. **55**(1): p. 32-38.

204. Collingwood, J. and J. Dobson, *Mapping and characterization of iron compounds in Alzheimer's tissue.* Journal of Alzheimer's Disease, 2006. **10**(2/3): p. 215-222.

205. Wang, H., et al., *The distribution profile and oxidation states of biometals in APP transgenic mouse brain: dyshomeostasis with age and as a function of the development of Alzheimer's disease.* Metallomics, 2012. **4**(3): p. 289-296.

206. Saeed, S.M. and G. Fine, *Thioflavin-T for amyloid detection.* American journal of clinical pathology, 1967. **47**(5): p. 588-588.

207. Westermark, G.T., K.H. Johnson, and P. Westermark, *Staining methods for identification of amyloid in tissue.* Methods in enzymology, 1999. **309**: p. 3-25.

208. Collingwood, J.F., et al., *High-resolution x-ray absorption spectroscopy studies of metal compounds in neurodegenerative brain tissue.* Journal of Physics: Conference Series, 2005. **17**(1): p. 54-60.

209. Borchardt, T., et al., *Copper inhibits beta-amyloid production and stimulates the non-amyloidogenic pathway of amyloid-precursor-protein secretion.* Biochemical Journal, 1999. **344**(Pt 2): p. 461-461.

210. Crouch, P.J., et al., *Increasing Cu bioavailability inhibits Aβ oligomers and tau phosphorylation.* Proceedings of the National Academy of Sciences, 2009. **106**(2): p. 381-386.

211. Huang, M., et al., *Elucidation of the mechanism of mitochondrial iron loading in Friedreich's ataxia by analysis of a mouse mutant.* Proceedings of the National Academy of Sciences, 2009. **106**(38): p. 16381-16386.

212. Donnelly, P.S., et al., *Selective intracellular release of copper and zinc ions from bis (thiosemicarbazonato) complexes reduces levels of Alzheimer disease amyloid-β peptide.* Journal of Biological Chemistry, 2008. **283**(8): p. 4568-4577.

213. Cater, M., et al., *Intracellular copper deficiency increases amyloid-beta secretion by diverse mechanisms.* Biochem. J, 2008. **412**: p. 141-152.

214. White, A.R., et al., *Degradation of the Alzheimer disease amyloid β-peptide by metal-dependent up-regulation of metalloprotease activity.* Journal of Biological Chemistry, 2006. **281**(26): p. 17670-17680.

215. Hung, Y.H., A.I. Bush, and R.A. Cherny, *Copper in the brain and Alzheimer's disease.* Journal of Biological Inorganic Chemistry, 2010. **15**(1): p. 61-76.

216. Atwood, C.S., et al., *Copper mediates dityrosine cross-linking of Alzheimer's amyloid.* Biochemistry, 2004. **43**(2): p. 560-568.

217. Wilcock, D.M., et al., *Progression of amyloid pathology to Alzheimer's disease pathology in an amyloid precursor protein transgenic mouse model by removal of nitric oxide synthase 2.* J Neurosci, 2008. **28**(7): p. 1537-1545.

218. Banci, L., et al., *Metal-free superoxide dismutase forms soluble oligomers under physiological conditions: a possible general mechanism for familial ALS.* Proceedings of the National Academy of Sciences, 2007. **104**(27): p. 11263-11263.

219. Shaw, B.F. and J.S. Valentine, *How do ALS-associated mutations in superoxide dismutase 1 promote aggregation of the protein?* Trends in Biochemical Sciences, 2007. **32**(2): p. 78-85.

220. Lamb, A.L., et al., *Crystal structure of the copper chaperone for superoxide dismutase.* Nature Structural & Molecular Biology, 1999. **6**(8): p. 724-729.
221. Potter, S. and J. Valentine, *The perplexing role of copper-zinc superoxide dismutase in amyotrophic lateral sclerosis (Lou Gehrig's disease).* Journal of Biological Inorganic Chemistry, 2003. **8**(4): p. 373-380.

222. Wong, P.C., et al., *Copper chaperone for superoxide dismutase is essential to activate mammalian Cu/Zn superoxide dismutase.* Proceedings of the National Academy of Sciences, 2000. **97**(6): p. 2886-2891.

223. Carroll, M.C., et al., *Mechanisms for activating Cu-and Zn-containing superoxide dismutase in the absence of the CCS Cu chaperone.* Proceedings of the National Academy of Sciences of the United States of America, 2004. **101**(16): p. 5964-5969.

224. Roe, J.A., et al., *In vivo peroxidative activity of FALS-mutant human CuZnSODs expressed in yeast.* Free Radical Biology and Medicine, 2002. **32**(2): p. 169-174.
225. Turner, B.J. and K. Talbot, *Transgenics, toxicity and therapeutics in rodent models of mutant SOD1-mediated familial ALS.* Progress in neurobiology, 2008. **85**(1): p. 94-134.

226. Niwa, J., et al., *Dorfin ubiquitylates mutant SOD1 and prevents mutant SOD1-mediated neurotoxicity.* Journal of Biological Chemistry, 2002. **277**(39): p. 36793-36798.

227. Kabashi, E., et al., *TARDBP mutations in individuals with sporadic and familial amyotrophic lateral sclerosis.* Nature Genetics, 2008. **40**(5): p. 572-574.

228. Bogdanov, M., et al., *Increased oxidative damage to DNA in ALS patients.* Free Radical Biology and Medicine, 2000. **29**(7): p. 652-658.